NUREG/CR-2905

Raman Scattering Temperature Measurements for Water Vapor in Nonequilibrium Dispersed Two-Phase Flow

Prepared by C. M. Anastasia, S. Neti, W. R. Smith, J. C. Chen

Institute of Thermo-Fluid Engineering and Science
Lehigh University

Prepared for
U.S. Nuclear Regulatory Commission

GPO Printed copy price: $7.00

NUREG/CR-2905
R2

Raman Scattering Temperature Measurements for Water Vapor in Nonequilibrium Dispersed Two-Phase Flow

Manuscript Completed: June 1982
Date Published: September 1982

Prepared by
C. M. Anastasia, S. Neti, W. R. Smith, J. C. Chen

Institute of Thermo-Fluid Engineering and Science
Lehigh University
Bethlehem, PA 18015

Prepared for
Division of Accident Evaluation
Office of Nuclear Regulatory Research
U.S. Nuclear Regulatory Commission
Washington, D.C. 20555
NRC FIN B6794

ACKNOWLEDGEMENTS

This research was sponsored by the National Science Foundation through Grant ENG78-11222, and by the U.S. Nuclear Regulatory Commission through Contract NRC-04-81-183.

The authors acknowledge the interest and encouragement given by Dr. Y. Y. Hsu and Mr. M. Young of U.S. NRC. The authors are also particularly grateful to Dr. Philip Kosky, previously a faculty member at Lehigh University, for the initial suggestion of using laser Raman spectroscopy for this application.

TABLE OF CONTENTS

TABLE OF CONTENTS (Continued)

LIST OF TABLES

LIST OF FIGURES

LIST OF FIGURES (Continued)

LIST OF FIGURES (Continued)

LIST OF FIGURES (Continued)

LIST OF FIGURES (Continued)

LIST OF FIGURES (Continued)

ABSTRACT

In several important applications of dispersed, two-phase flow, the possible occurrence of thermodynamic nonequilibrium between the vapor and liquid phases is of fundamental interest and practical concern. The measurement of the potential superheated temperatures of the vapor, in the presence of cold liquid droplets remains a difficult experimental task. To date, only partial success has been obtained by use of intrusive, aspirating thermocouple probes. The objective of this present investigation was to determine the feasibility of using Raman scattering to measure vapor temperatures in dispersed two-phase flow as an alternative nonintrusive technique.

The Raman system developed for this investigation is described, including alignment of optics and optimization of the photodetector for photon pulse counting. Experimentally obtained Raman spectra are presented for the following single- and two-phase samples: liquid water, atmospheric nitrogen, superheated steam, nitrogen and water droplets in a high void fraction air/water mist, and superheated water vapor in nonequilibrium dispersed flow.

The Stokes vibrational Raman band was measured for single-phase steam at atmospheric pressure, with 20 to 200 K vapor superheat ($T-T_{SAT}$, $T_{SAT} = 373$ K). Integrated intensity ratios, calculated from these spectra, can be used for temperature measurements with an estimated uncertainty of ±15 K.

Water droplets, in two-phase samples, cause Mie and Raman scattering which interfere with the desired measurement. Mie scattering is many orders of magnitude more intense than Raman scattering, but is spectrally removed from the Raman vibrational bands, and was rejected using a triple monochromator. Raman spectra, measured for atmospheric nitrogen in an air/water mist, show that although the uncertainty is approximately double that of single-phase samples, Stokes vibrational spectra can be measured in dispersed two-phase samples. For water, in non-equilibrium dispersed flow, the 3400 cm^{-1} Raman band for the droplets creates a potential spectral interference with the 3650 cm^{-1} Raman band for the vapor. Raman scattering from the droplets contributed a small but measurable intensity in the spectral region of interest for water vapor. This contribution was considered negligible in Raman measurements for water vapor in nonequilibrium dispersed flow.

The Stokes vibrational Raman band for water vapor was observed in dispersed flow, at atmospheric pressure, and 20 to 80 K nonequilibrium vapor superheat ($T-T_{SAT}$, $T_{SAT} = 373$ K). The vapor to liquid mass flow ratio was about two, and equilibrium qualities were 62 to 71 percent. Integrated intensity ratios, calculated from these spectra, can be used for temperature measurements with an estimated uncertainty of ±22 K.

1. INTRODUCTION

Continued refinement of nuclear reactor safety codes has created the need for improved heat transfer models and correlations in post-critical-heat-flux (CHF) boiling. Heat transfer in the dispersed flow regime which may develop after the critical heat flux occurs at moderate to high qualities (greater than 40 percent) is of particular interest. Dispersed two-phase flow may be described as a vapor continuum in which liquid droplets are entrained. In dispersed post-CHF flows, heat transfer is governed mainly by the temperature difference between the vapor and the wall. A recent paper by Nijhawan, et al. [1.1], emphasized the importance of non-equilibrium vapor superheat in developing analytical models and heat transfer correlations for post-CHF, dispersed flow.

Nijhawan, et al., developed an aspirated thermocouple probe for measurement of vapor superheat in nonequilibrium dispersed flow. Experimental difficulties and uncertainties associated with this probe led to the need for an alternate technique for vapor temperature measurements in dispersed two-phase flow.

Laser Raman spectroscopy is a nonintrusive optical technique which has been developed as a diagnostic probe for gas dynamic studies [1.2]. Previous research [1.3, 1.4, 1.5] has demonstrated the temperature sensitivity of Raman spectra for common gases such as nitrogen and water vapor. These studies were restricted to single phase samples with minimal particulate contamination.

The general objective of this program is to use laser Raman spectroscopy to measure nonequilibrium vapor temperatures in

dispersed flow. Raman techniques have not been previously used for analysis of multiphase samples, thus the program was divided into two phases.

1. Proof of principle experiment
2. Verification of aspirated thermocouple data and application to practical heat transfer problems

A proof of principle experiment was necessary to demonstrate the applicability of Raman diagnostic techniques to multiphase flow. The new technique may be used later to verify aspirated thermocouple data in nonequilibrium, dispersed flow. Subsequent use of Raman techniques in dispersed flow may lead to a better understanding of multiphase heat transfer.

This report describes the proof of principle experiment.

2. LITERATURE SURVEY

2.1 History and Theory of Raman Scattering

C. V. Raman first observed frequency shifted light in Calcutta, 1928 [2.1]. Raman scattering was quickly recognized as a powerful tool for investigation of molecular structure. Early applications concentrated on analysis of liquids and crystalline solids [2.2]. The development of coherent lasers and efficient photoelectric detectors in the early 1960's led to widespread application of Raman techniques to fluid dynamic studies. Current state-of-the-art Raman techniques use pulsed lasers and photon counting detectors to obtain time, and spatially resolved, temperature and species concentration measurements over a wide range of practical liquid and gas flow conditions [2.3].

Inelastically scattered light (Raman spectra) from hot gas molecules provides a temperature dependent signature for a nonintrusive probe. Absorbtion of incident light into a virtual molecular state and emission of scattered light are modulated by molecular vibrational and rotational frequencies. The scattered light has characteristic molecular frequency shifts. Quantum restrictions on rotational and vibrational energy transitions impart known temperature dependence on the spectral intensity distribution of Raman scattered light.

The Raman frequency shift is a characteristic of the scattering molecule. Raman spectra of simple molecules are spectrally separated (with the exception of occasional overlaps) allowing simultaneous independent observation of a variety of species.

Spontaneous Raman scattering is a linear optical process (as compared to resonance Raman [2.4] and coherent anti-Stokes Raman [2.5]). The scattering intensity is proportional to the number density of the scattering molecules.

A simplified classical model, described below, may be used to explain the frequency shift characteristic of Raman scattering [2.6]. Consider a molecule irradiated by monochromatic light. The electric field, E(t), associated with the incident light oscillates at the incident frequency, ω_o.

$$E(t) = E_o \cos\omega_o t \tag{2.1}$$

An oscillating dipole is created by the effect of the electric field on the molecule's electron cloud. The molecular polarizability, α, relates the induced dipole, $\mu(t)$, to the incident field.

$$\mu(t) = \alpha E(t) \tag{2.2}$$

Rotational and vibrational molecular frequencies modulate the polarizability which may be expressed as a constant plus a component modulated by the molecular frequency, ω.

$$\alpha = \alpha_o + \alpha_1 \cos\omega t \tag{2.3}$$

Manipulation of equations (2.1) through (2.3) reveals the origins of frequency shifted (Raman) and unshifted (Rayleigh) components of scattered light.

$$\mu(t) = [\alpha_o + \alpha_1 \cos\omega t][E_o \cos\omega_o t] \tag{2.4}$$

Using the trigonometric identity (2.5)

$$[\cos\omega t][\cos\omega_o t] = \frac{1}{2}[\cos(\omega_o+\omega)t + \cos(\omega_o-\omega)t] \qquad (2.5)$$

equation (2.4) may be rewritten as (2.6).

$$\mu(t) = \alpha_o E_o \cos\omega_o t + E_o\alpha_1/2[\cos(\omega_o+\omega)t + \cos(\omega_o-\omega)t] \quad (2.6)$$

The modulated oscillating dipole scatters light at three frequencies. The first term of equation (2.6) represents the unshifted frequency or Rayleigh scattering at ω_o. The second and third terms of equation (2.6) are symmetrically shifted about the incident frequency. These terms represent anti-Stokes ($\omega_o+\omega$) and Stokes ($\omega_o-\omega$) Raman scattering.

The classical model described above does not explain the temperature dependence of Raman spectra; for this, quantum mechanical restrictions must be considered. Figure 2.1 illustrates the quantum nature of light scattering processes. The horizontal lines represent potential rotational and vibrational energy levels of the scattering molecule. Rayleigh scattering is illustrated in part a. An incident photon of frequency ω_o excites the molecule to a higher virtual energy level. A scattered photon of the same frequency is simultaneously emitted leaving the molecule at its original level. The process is instantaneous and no net energy transfer takes place. Parts b and c illustrate Stokes and anti-Stokes Raman scattering. The scattered photon may have a higher (anti-Stokes, $\omega_o+\omega$) or a lower (Stokes, $\omega_o-\omega$) frequency than the incident photon. The

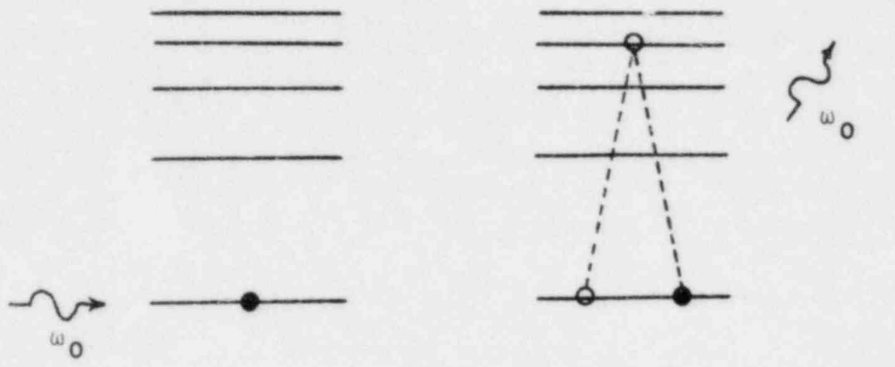

a) Rayleigh scattering

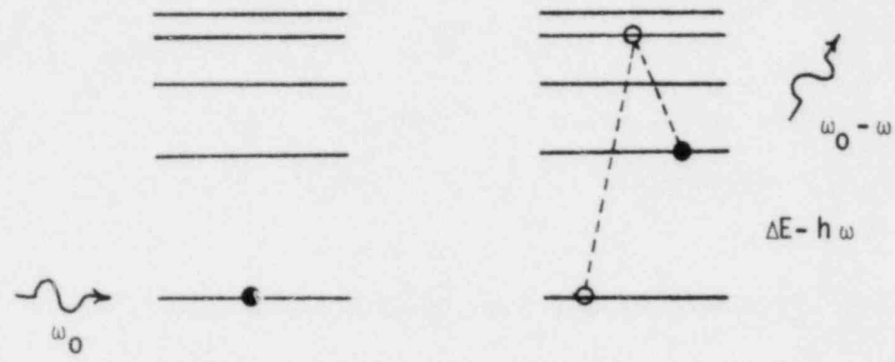

b) Stokes Raman scattering

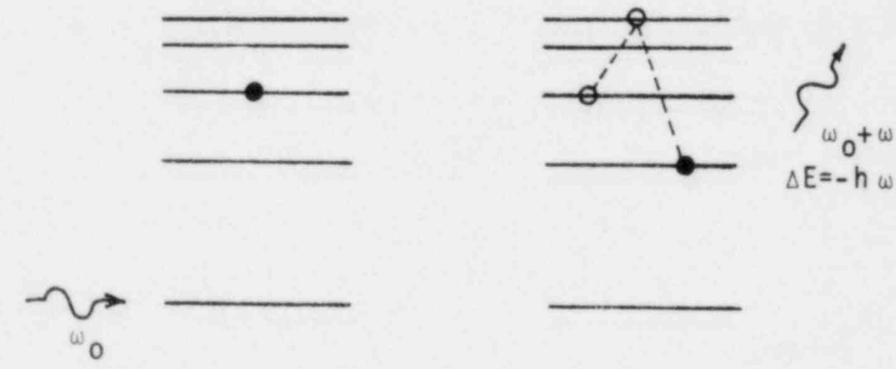

c) Anti-Stokes Raman scattering

Figure 2.1 Quantum nature of molecular light scattering processes [2.7]

frequency shift corresponds to the net change of rotational or vibrational energy of the scattering molecule.

For each possible rotational and vibrational transition there is an associated Raman frequency shift. The Raman spectrum of a molecule is made up of a series of discrete frequency shifted lines. The relative intensity of these lines is determined by the probability of the associated transitions which depends on the energy population distribution of the scattering medium. The spectral intensity distribution of Raman scattered light is a measure of the energy population distribution of the probed medium and is directly related to temperature [2.8].

Application of quantum restrictions to an ideal harmonic oscillator and a rigid rotator leads to the approximate expressions, given below, for the temperature dependence of Stokes, I_s, and anti-Stokes, I_{as}, Raman scattering intensities for simple molecules.

$$I_s \propto (\omega_o-\omega)^4/[1-\exp(-hc\omega/KT)] \tag{2.7}$$

$$I_{as} \propto (\omega_o-\omega)^4\exp(-hc\omega/KT)/[1-\exp(-hc\omega/KT)] \tag{2.8}$$

where h is Plank's constant, K is the Boltzman constant, c is the speed of light and T is the absolute temperature [2.9]. This approximate analysis is valid only for pure rotational and vibrational transitions and applies only as a limiting case for diatomic molecules.

2.2 Raman Techniques

A typical laser Raman experiment is illustrated in Figure 2.2.

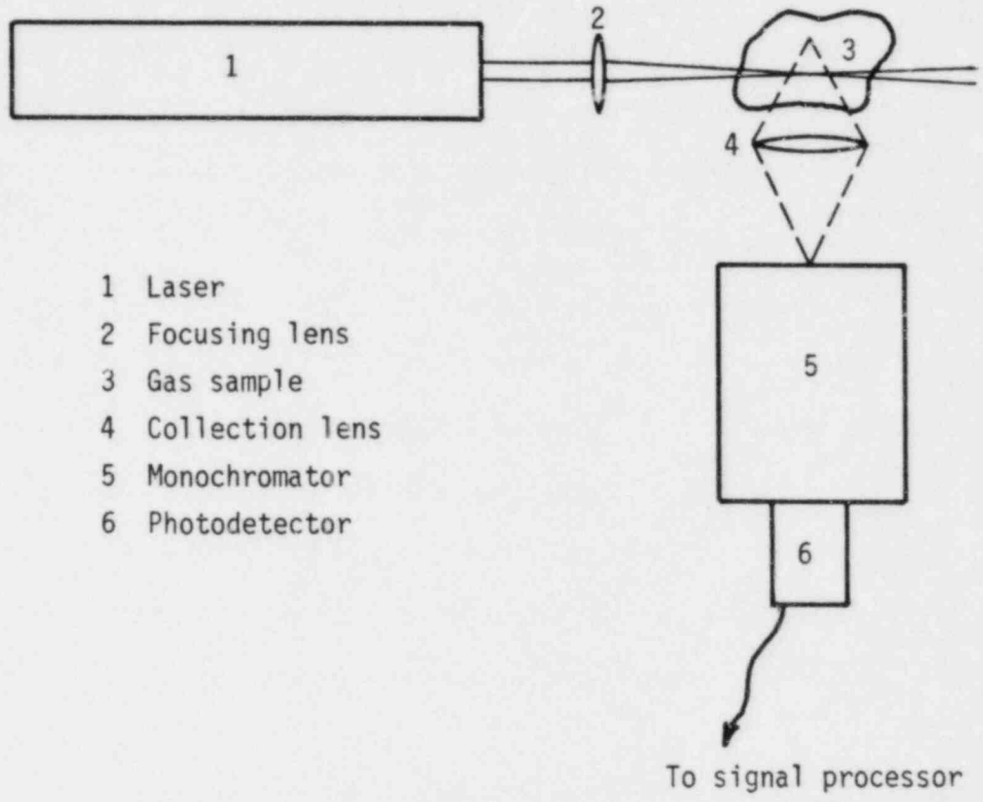

1 Laser
2 Focusing lens
3 Gas sample
4 Collection lens
5 Monochromator
6 Photodetector

Figure 2.2 Typical laser Raman experiment

The sample is irradiated with focused laser light. Scattered light is collected and focused on a monochromator. The spectral intensity distribution is observed using a photoelectric detector. Electronic signals from the detector are amplified and recorded by a signal processor. Rotational or vibrational Raman spectra may be observed with this type of system. The data which may be obtained and the techniques used to characterize temperature dependence of the spectra are described below. Several variations on the basic Raman system are also discussed.

Figure 2.3 is a sketch of the spectral intensity distribution of scattered light from atmospheric nitrogen at room temperature irradiated by a 488 nm incident laser. Rotational transitions cause symmetrically shifted Raman bands about the incident wavelength and about the Stokes and anti-Stokes Raman vibrational branches. At room temperature, rotational broadening of the anti-Stokes vibrational branch is negligible but increases at higher temperatures.

On the scale shown in Figure 2.3, the rotational and vibrational bands are unresolved. Theoretically, the spectra are made up of discrete lines, each shifted by a rotational or vibrational frequency as shown in Figure 2.4. Experimentally observed spectra are convoluted by the monochromator slit function. Observed spectra may or may not be resolved depending on the band width of the slit function. A comparison of slit functions is illustrated qualitatively in Figure 2.5. The effect of a narrow band, triangular slit function is shown in part b. Individual lines are resolved

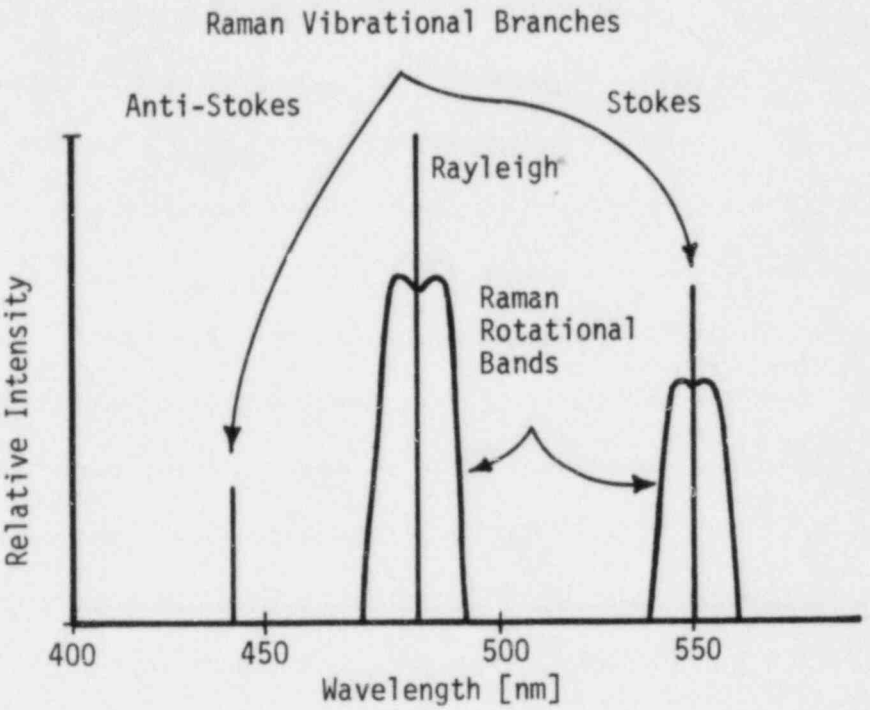

Figure 2.3 Spectral intensity distribution of scattered light from atmospheric nitrogen at room temperature irradiated by a 488 nm incident laser [2.10]

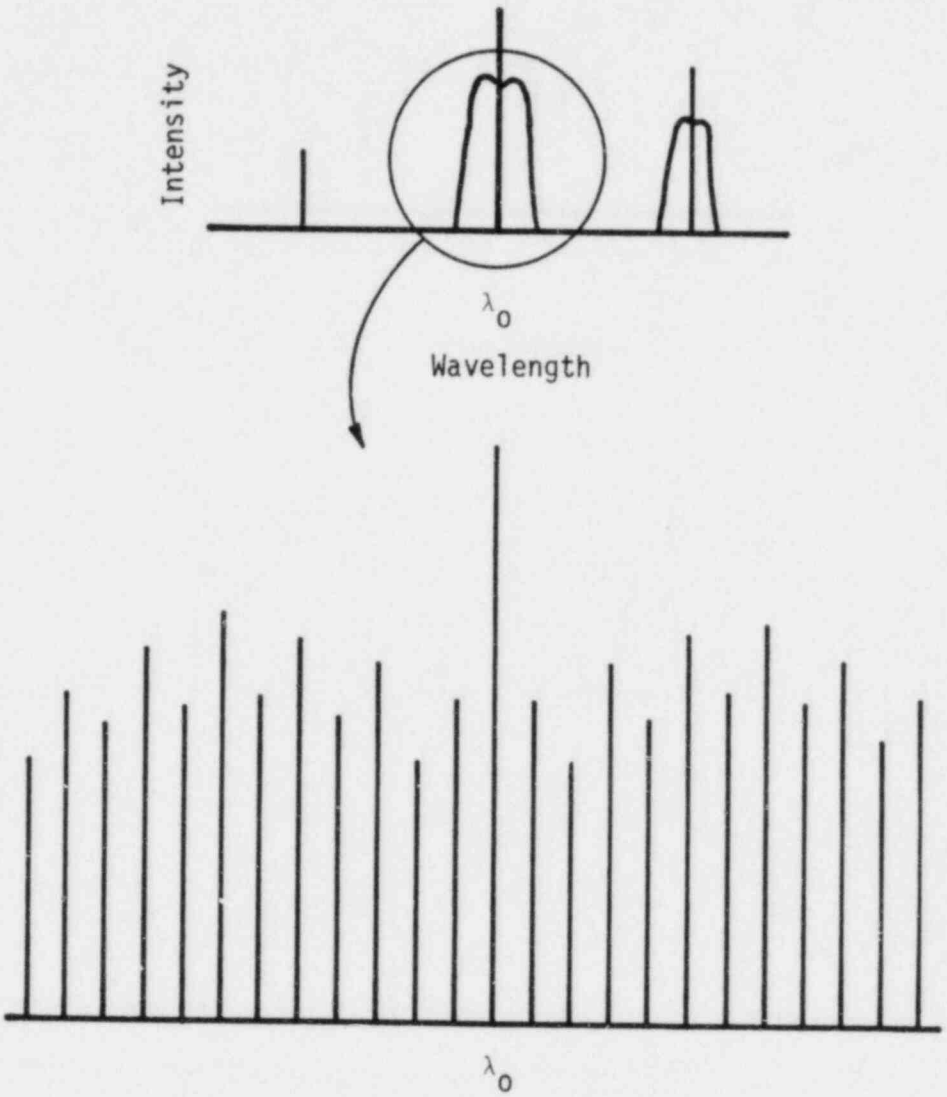

Figure 2.4 Schematic of theoretical rotational Raman bands for a diatomic molecule [2.11]

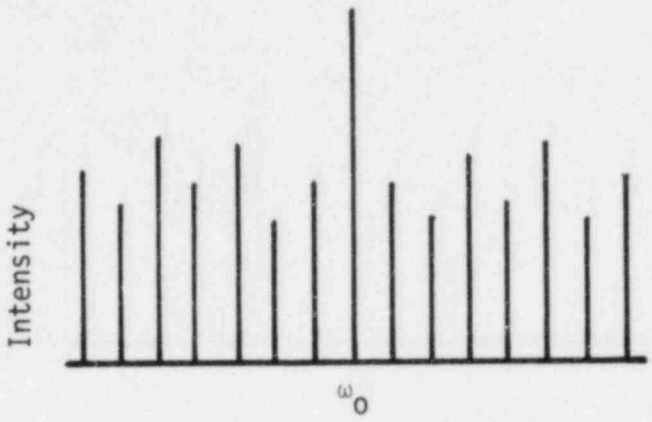

a) Theoretical rotational Raman spectrum

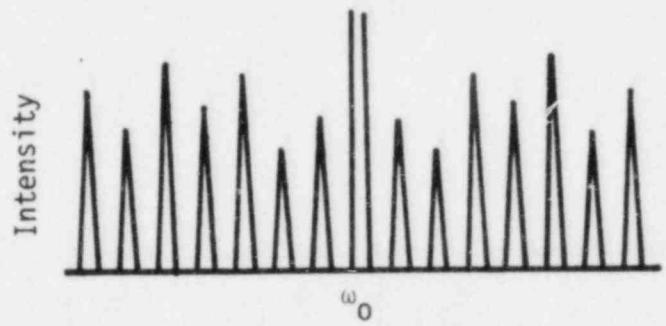

b) Resolved rotational spectrum observed with a narrow band slit function

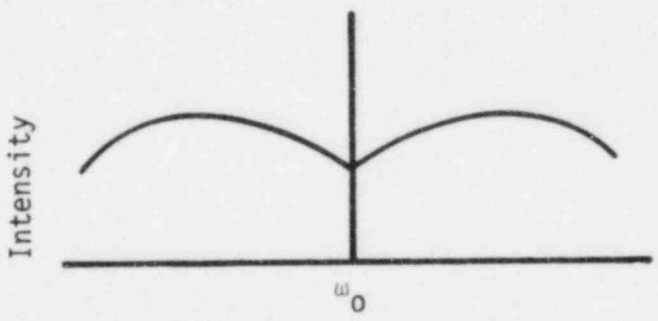

c) Unresolved rotational envelope observed with a broad band slit function

Figure 2.5 Comparison of monochromator slit functions [2.12]

resulting in a contour that looks similar to the actual intensity distribution. The effect of a broad band slit function is shown in part c. The broad band slit function integrates intensity over a larger bandwidth resulting in a smoothed spectral envelope.

The effect of temperature on an unresolved rotational contour is shown in Figure 2.6. There are two types of techniques which may be used to characterize the temperature dependence of Raman spectra.

1. Curve fitting techniques
2. Intensity ratio techniques

Either type of technique may be applied to both rotational and vibrational Raman spectra.

Curve fitting techniques are based on comparing the spectral band shape observed at an unknown temperature to a set of reference spectra at known temperatures [2.14, 2.15]. The reference spectra may be theoretically calculated or obtained empirically through controlled experiments. A least square fit or similar criterion is used to determine which of the reference spectra the observed data matches. Curve fitting may be applied to resolved Raman contours or unresolved spectral envelopes.

Curve fitting is an obvious but time consuming technique; intensity ratio techniques are a simpler alternative. Consider Figure 2.7, the intensity of a given frequency shifted line is represented by $I(\omega)$. Careful selection of spectral lines yields a dimensionless, temperature sensitive parameter, R.

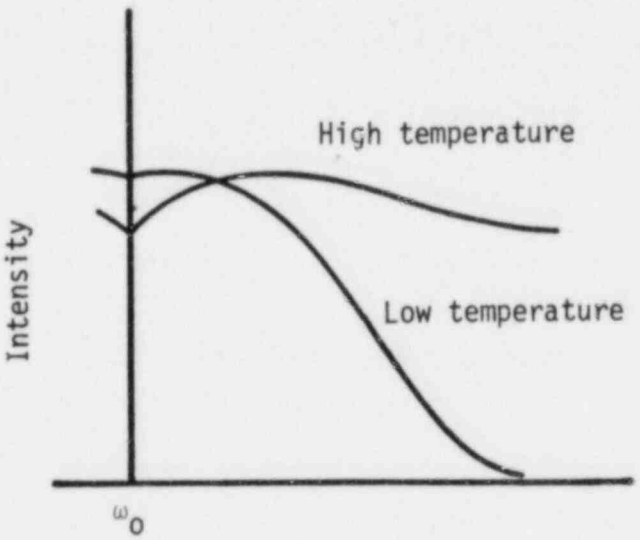

Figure 2.6 Effect of temperature on an unresolved rotational Raman spectrum [2.13]

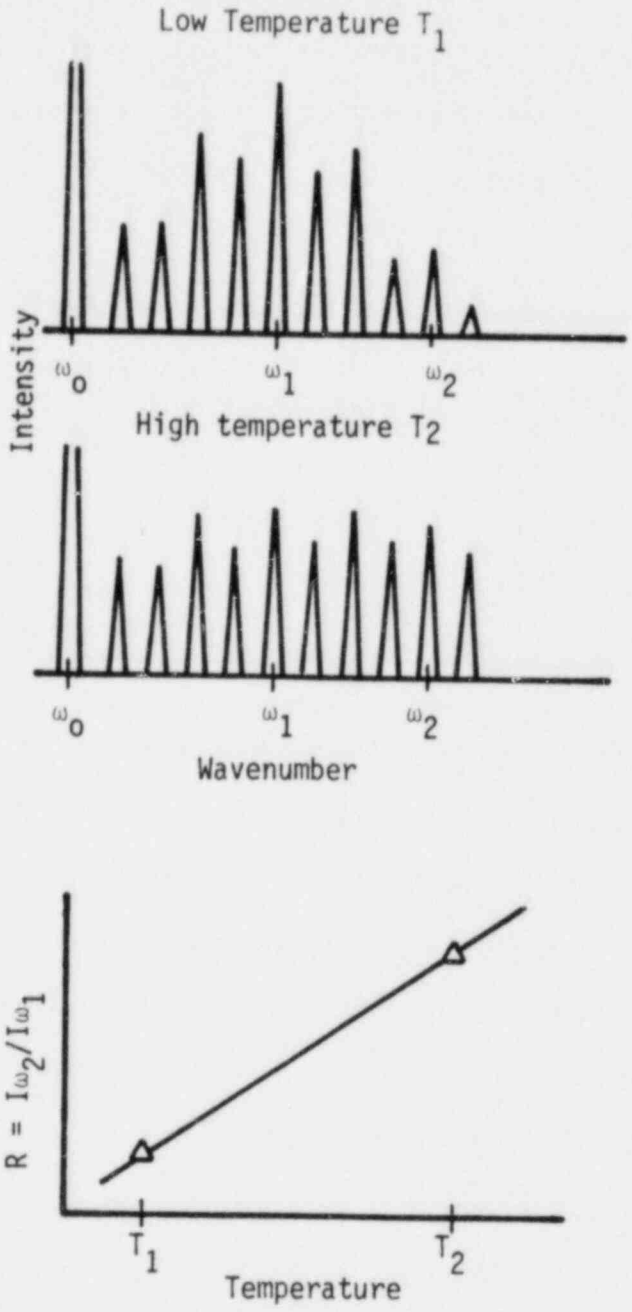

Figure 2.7 Use of intensity ratios, of Raman spectral lines, for temperature measurements

$$R = I(\omega_2)/I(\omega_1) \tag{2.9}$$

The intensity of selected spectral bands rather than lines may also be used to form a temperature sensitive ratio as illustrated in Figure 2.8. The integrated intensity in a selected spectral band is given by equation (2.10).

$$I_\Delta = \int_{\omega_1}^{\omega_2} I(\omega)d\omega \tag{2.10}$$

Careful selection of spectral bands produces a temperature sensitive parameter, R.

$$R = I\Delta_1/I\Delta_2 = \int_{\omega_3}^{\omega_4} I(\omega)d\omega \Big/ \int_{\omega_1}^{\omega_2} I(\omega)d\omega \tag{2.11}$$

Stokes to anti-Stokes intensity ratios may also be used for temperature measurements as suggested by equations (2.7) and (2.8). For Stokes/anti-Stokes measurements, the intensity of individual lines or entire bands may be used. Detailed information on optimal selection of intensity ratios for temperature measurements using rotational and vibrational Raman spectra of nitrogen may be found elsewhere [2.16, 2.17, 2.18].

The advantage of measurements using rotational rather than vibrational Raman scattering is in the larger scattered light intensity. Cross sections for rotational scattering are typically 10 to 100 times larger than vibrational scattering cross sections [2.19]. Rotational scattering is considered useful for single component gases in "clean" environments. Rotational techniques

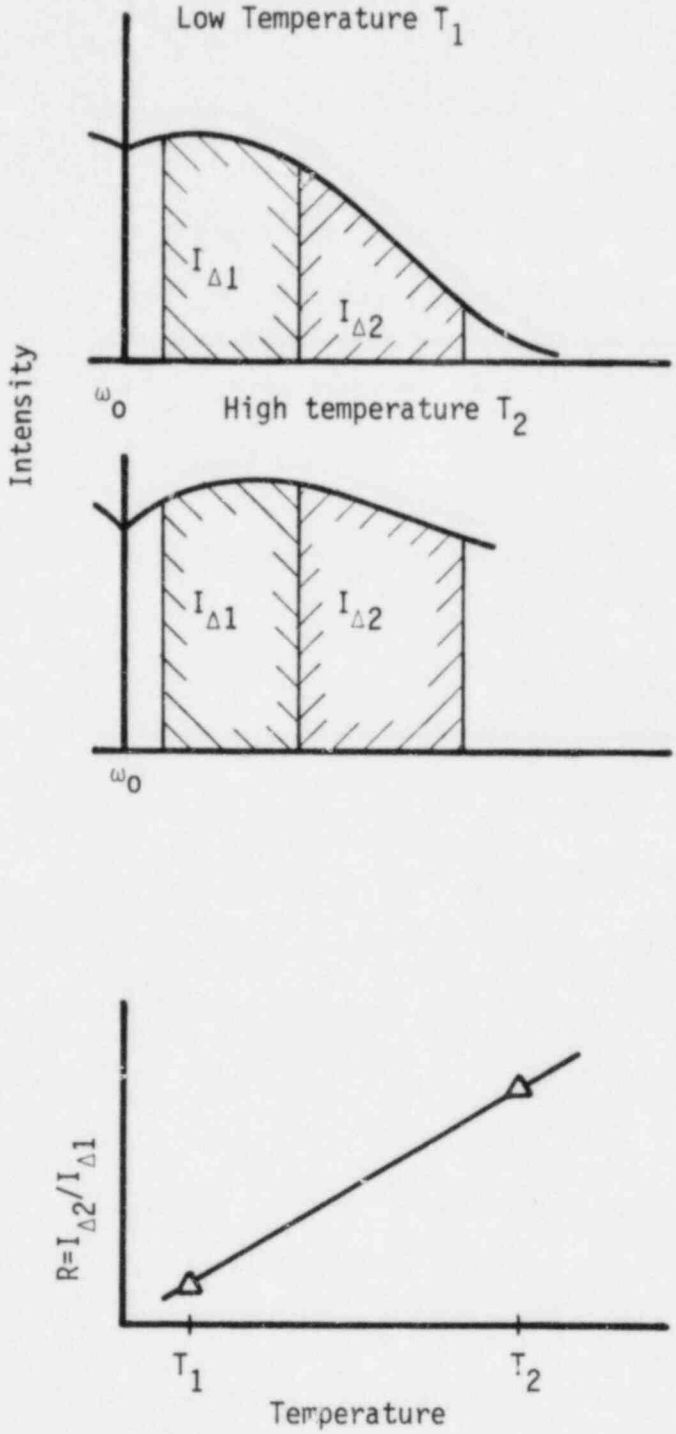

Figure 2.8 Use of integrated intensity ratios of Raman spectral bands for temperature measurements

are generally not used for analysis of multicomponent gases because rotational spectra of many common species overlap [2.20]. Interferences between species complicate rotational spectra making data analysis difficult.

Rotational shifts are small, on the order of 100 cm^{-1}, as compared to vibrational shifts, which are on the order of 1,000 cm^{-1}, thus the spectral region of interest for rotational scattering is near the incident wavelength. The larger spectral shifts, characteristic of vibrational Raman scattering, offer a distinct advantage in "dirty" environments where particulates or droplets cause intense Mie (elastic) scattering of the incident light. Most spectral instruments are incapable of rejecting intense Mie scattering at the incident wavelength which is very near the spectral region of interest for rotational scattering. Although vibrational bands are weaker, they are spectrally removed from elastic scattering at the incident wavelength. Commercially available spectral instruments are capable of rejecting intense Mie scattering which is far from the spectral region of interest for vibrational Raman bands.

Lapp [2.21] used vibrational Raman scattering from nitrogen to measure the temperature of a flame at approximately 1600 K to within about 35 K. Salzman, et al. [2.22], used rotational Raman scattering to measure the temperature of nitrogen in a controlled sample cell over the range 253 to 313 K to within about 7 K.

A variety of lasers, monochromators, photodetectors, and signal processors are available for building Raman systems at

different levels of sophistication. Raman instruments may take several forms, some of these are described below.

The most commonly used spectral instrument is a scanning grating spectrograph. Specialized systems may use interference filters in combination with a diffraction grating to isolate spectral bands. Figures 2.9 through 2.11 illustrate potential configurations for Raman systems. Figure 2.9 shows a scanning grating spectrograph with a photomultiplier tube (PMT) mounted at the exit slit. Incoming light is dispersed by a diffraction grating. A small spectral segment passes the slit and is detected by the PMT. This configuration requires a single photodetector and a serial input signal processor. To acquire a spectrum, the grating is rotated presenting successive wavelengths to the detector. The PMT signal is recorded and plotted as a function of the grating position to produce a spectral intensity distribution. The advantages of scanning systems are simplicity, versatility, and relatively low cost. The spectral region to be scanned may be changed routinely. The disadvantage of scanning systems are low speed and mechanical nonreproducibility. The spectral region of interest is observed in small segments. While one segment is being observed, data at all other wavelengths is lost. The size of the wavelength segment which a scanning system observes is usually small compared to the spectral region of interest; thus, each scan takes a long time. Mechanical linkages required to rotate the grating impart nonreproducibility to spectral data, and wavelength accuracy is limited by mechanical backlash.

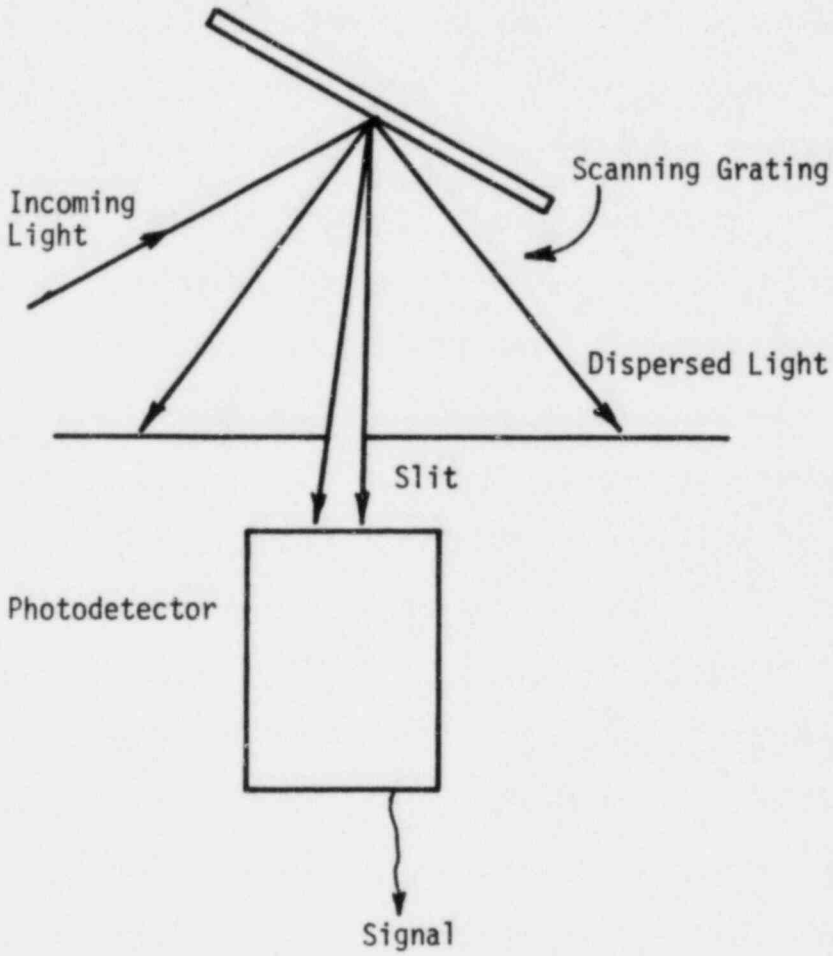

Figure 2.9 Scanning spectrograph with PMT mounted at exit slit

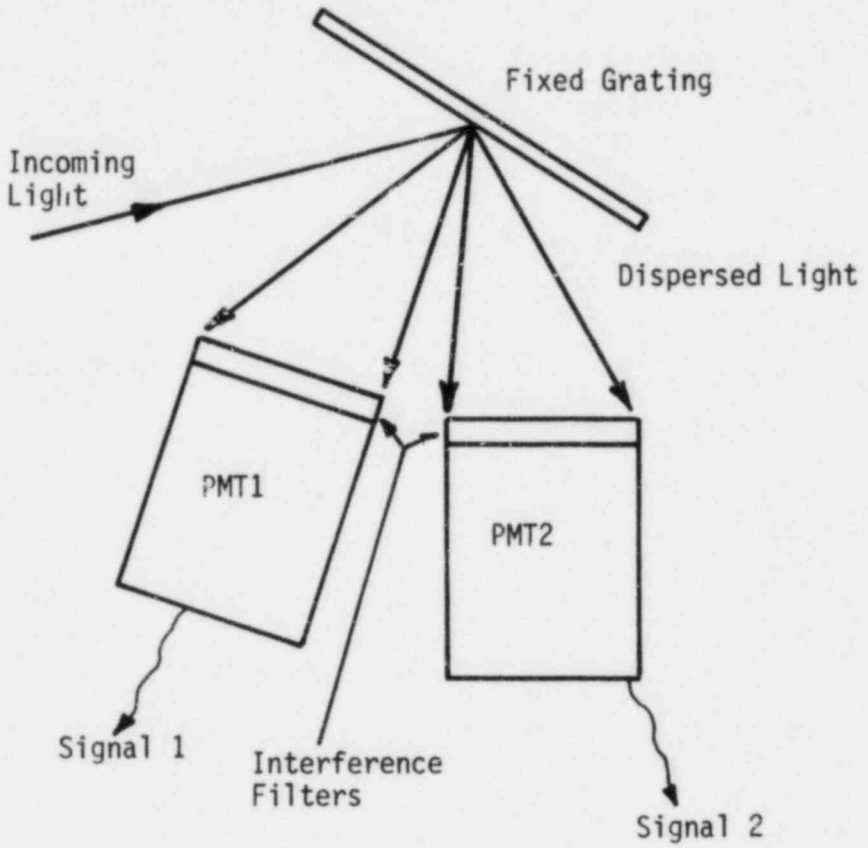

Figure 2.10 Fixed grating system with two photodetectors for monitoring two spectral bands

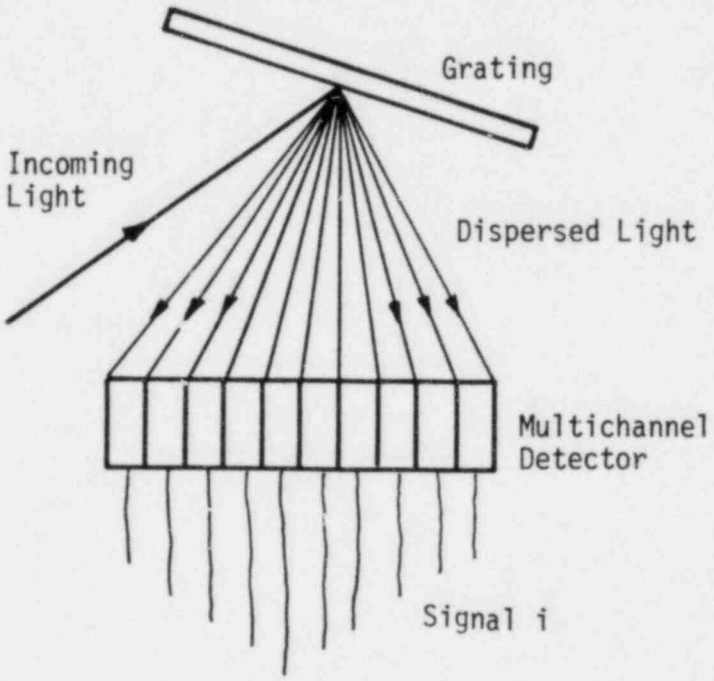

Figure 2.11 Spectrograph with optical multichannel detector for monitoring entire spectral bands simultaneously

Figure 2.10 illustrates a specialized system designed to monitor the intensity of two spectral lines or bands simultaneously. The light to be analyzed is dispersed by a diffraction grating. Two photodetectors are precisely positioned so each monitors a selected spectral region. Interference filters may be added in front of each detector to improve spectral discrimination. Two parallel data processing channels are required for effective use of this configuration. This scheme is more difficult to set up than a scanning system and is less versatile. Once in place, this configuration is not affected by mechanical reproducibility problems as are scanning systems but has limited spectral coverage. Such a scheme may be used to monitor the relative intensity of the Stokes and anti-Stokes bands.

The configuration shown in Figure 2.11 illustrates the use of a multichannel optical detector. Scattered light is dispersed across the array which may have 700 or more separate detectors. Each detector monitors an interval of wavelength allowing simultaneous observation of complete spectral bands. A multichannel detector used in conjunction with a scanning grating monochromator can obtain the same data as either of the previously described systems. The grating may be rotated when selecting the spectral band of interest, but is not rotated during data acquisition. Data is acquired much faster than with a simple scanning system

because the entire spectral band is monitored at once. Signal processing requirements for this type of system are more complex than either of the previous systems. The processor must accept parallel input from 700 or more detectors. Multichannel detectors and signal processors are commercially available.

The systems illustrated in Figures 2.9 and 2.11 may be used for both curve fitting and intensity ratio temperature measurement techniques. The system illustrated by Figure 2.10 is limited to intensity ratio techniques. The scanning spectrograph system is useful only for steady state measurements. The other two systems may be used for steady state measurements with continuous wave lasers or may be adapted for transient measurements using pulsed lasers.

2.3 Raman Spectral Studies of Water

Previous researchers investigated the application of Raman techniques for remote temperature sensing in both liquid water and water vapor.

Pan, et al. [2.23] used laser Raman spectroscopy for remote temperature sensing in liquids. Carbon tetrachloride, benzene, ethylene glycol, and water were among the liquids studied. Variations in the 3400 cm^{-1} Raman band for water were measured from 290 to 330 K. Correlations were developed to relate spectral parameters, based on the Raman band shape, to the sample temperature. The uncertainty of these measurements was found to be 1.5 K.

Lapp [2.24, 2.25], Penney and Lapp [2.26], and Bribes, et al.

[2.27,2.28] investigated the feasibility of temperature and density measurements for water vapor in flames. Lapp and Penney measured Raman vibrational contours for water vapor from 290 to 1500 K. Bribes, et al., conducted a theoretical investigation to determine the temperature sensitivity of vibrational band contours over the same temperature range. Theoretically calculated band contours were found to agree well with experimental data. These studies showed that Raman scattering from water vapor can be used for temperature and density measurements and that good temperature sensitivity can be obtained from the vibrational contours.

These studies were restricted to single phase-samples. In a two-phase water sample there is potential for spectral interference between Raman bands for the liquid and vapor phases. The 3400 cm^{-1} band for liquid water is broader than the 3650 cm^{-1} band for water vapor due to molecular interactions such as hydrogen bonding. Figure 2.12 shows the Raman vibrational bands for both the liquid and vapor phases. The liquid band overlaps the spectral region of interest for the vapor. For the relatively high void fractions (70 to 90 percent) of interest for this investigation, Raman scattering from the liquid phase was expected to cause minimal interference.

2.4 Description of Research

The proof of principle experiment was intended to demonstrate the applicability of Raman techniques for vapor temperature measurements in nonequilibrium two-phase samples. The overall

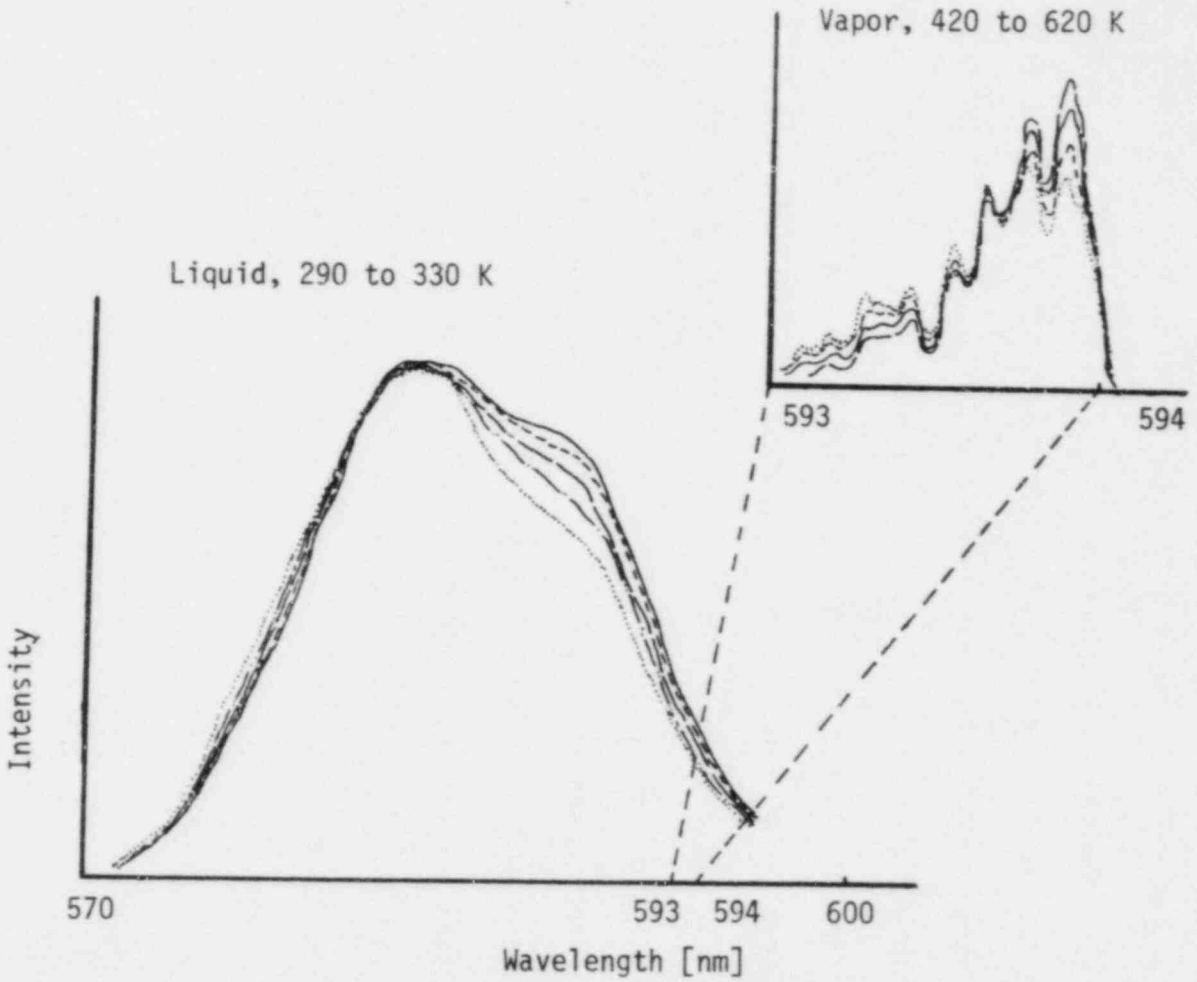

Figure 2.12 Raman scattering from water in liquid and vapor phases [2.29, 2.30]

objectives were to demonstrate feasibility and to estimate the sensitivity of proposed temperature measurements. This experiment could form the basis of future Raman spectral studies of two-phase flows. Problem areas have been identified and recommendations made. The proof of principle experiment was divided into the smaller tasks listed below.

1. Development of a Raman spectroscopy system.
2. Preliminary Raman studies of liquid water and atmospheric nitrogen for development of experimental procedures and data analysis techniques.
3. Observation of temperature effects on Raman spectra of single-phase superheated steam.
4. Observation of Raman scattering from the gas and liquid phases of a high void fraction air/water mist to determine the effect of Mie and Raman scattering from the liquid droplets.
5. Observation of temperature effects on Raman spectra of superheated steam in nonequilibrium dispersed two-phase samples.

A major difficulty with Raman experiments is the weakness of the Raman scattering. Air at standard conditions scatters approximately 10^{-10} of an incident beam per mm along the beam into all Raman bands, in all directions [2.31]. Scattering intensities from water vapor under the conditions of interest here are of the same order of magnitude. An intense laser source is required

for incident radiation along with a sensitive photodetector for measurement of low intensity scattered light.

The intensity of Raman scattered light is proportional to the fourth power of the incident frequency [2.32]. For maximum scattered intensities, a high frequency laser is required. An Argon ion laser of maximum practical power (1.5 watts), operating in the deep blue (488 nm) was used. A photon counting detection system was used to measure the Raman scattering intensities.

The presence of liquid droplets in the flow field causes intense Mie (elastic) scattering at the wavelength of the incident laser in amounts estimated at 5×10^7 to 5×10^9 that of the Raman scattered light [2.33]. Intense Mie scattering from liquid droplets imposes additional stray light rejection requirements. The spectral discrimination system uses a scanning grating spectrograph with a double monochromator as a prefilter. The double monochromator, which is capable of spectral purity of $2/10^9$ at 8 nm from the excitation, rejects the Mie scattering from liquid droplets. This investigation was restricted to the analysis of vibrational scattering as it is unlikely that rotational spectra can be measured in the presence of intense Mie scattering.

In the preliminary experiments, vibrational spectra for liquid water and atmospheric nitrogen at room temperature were observed. These experiments were used to refine system operating procedures for development of data analysis techniques and to demonstrate the reproducibility of the instrumentation.

Temperature dependence of Raman spectra for single-phase steam at atmospheric pressure and 20 to 200 K vapor superheat ($T-T_{SAT}$, T_{SAT} = 373 K) were observed. Results of these experiments were used to estimate the sensitivity of temperature measurements for single-phase steam.

Two-phase experiments were conducted by injecting an atomized spray of water droplets into room temperature air and superheated steam. For a short distance downstream of the spray nozzle, a controlled liquid/gas mixture was established; it is in this region that Raman spectra were observed. Raman scattering from atmospheric nitrogen was observed in a high void fraction (70 to 90 percent) air/water mist to investigate the effect of the droplets. Raman scattering from liquid droplets in the mist was also observed to investigate potential spectral interference between the liquid and vapor phases for nonequilibrium two-phase steam. Raman spectra were measured for steam in nonequilibrium dispersed two-phase samples for a vapor to liquid mass flow ratio of about 2.0 and vapor superheats ($T-T_{SAT}$, T_{SAT} = 373 K) ranging from 20 to 80 K. The results were used to estimate the sensitivity of proposed vapor temperature measurements in nonequilibrium, dispersed flow.

Raman experiments may be carried out at various levels of sophistication. For example, it is possible to use reference sources to calibrate the spectral response of optical components out of measured spectra. Similarly, emission lines of a spectral

calibration lamp may be used to determine the precise wavelength of spectral features. These steps are necessary when using Raman spectra to investigate molecular structure but were unnecessary for this proof of principle experiment. In this study, variations of Raman band shapes were measured as a function of temperature. As long as the measured band shapes were reproducible, the instrument response was considered to be of secondary importance.

3. EXPERIMENTAL APPARATUS

3.1 Introduction

The optical and electronic components of the Raman spectroscopy system are described here. An overview of the integrated system is followed by a detailed description of each component. Most of the components are commercially available; however, some have been modified slightly. Specifications and any special operating procedures for each component are also included.

3.2 System Overview

The Raman system developed for this research is shown schematically in Figure 3.1. The steam generator produces superheated steam which was mixed with an atomized water spray to produce non-equilibrium dispersed flow samples. The laser irradiates the sample with an intense beam of high frequency monochromatic light. The incident beam is concentrated on the measurement point by the focusing optics. The path of the incident beam through the sample defines the scattering volume. The collection optics focus scattered light onto the entrance slit of the premonochromator. The premonochromator filters the scattered light, transmitting a selected spectral band to the spectrograph. The spectrograph, driven by a microprocessor controlled stepping motor, sweeps the selected spectral band. The photomultiplier tube, optimized for photon counting, detects the spectral intensity distribution. The photomultiplier output is amplified and recorded by a multichannel analyzer. Each time the spectrograph steps through a wavelength

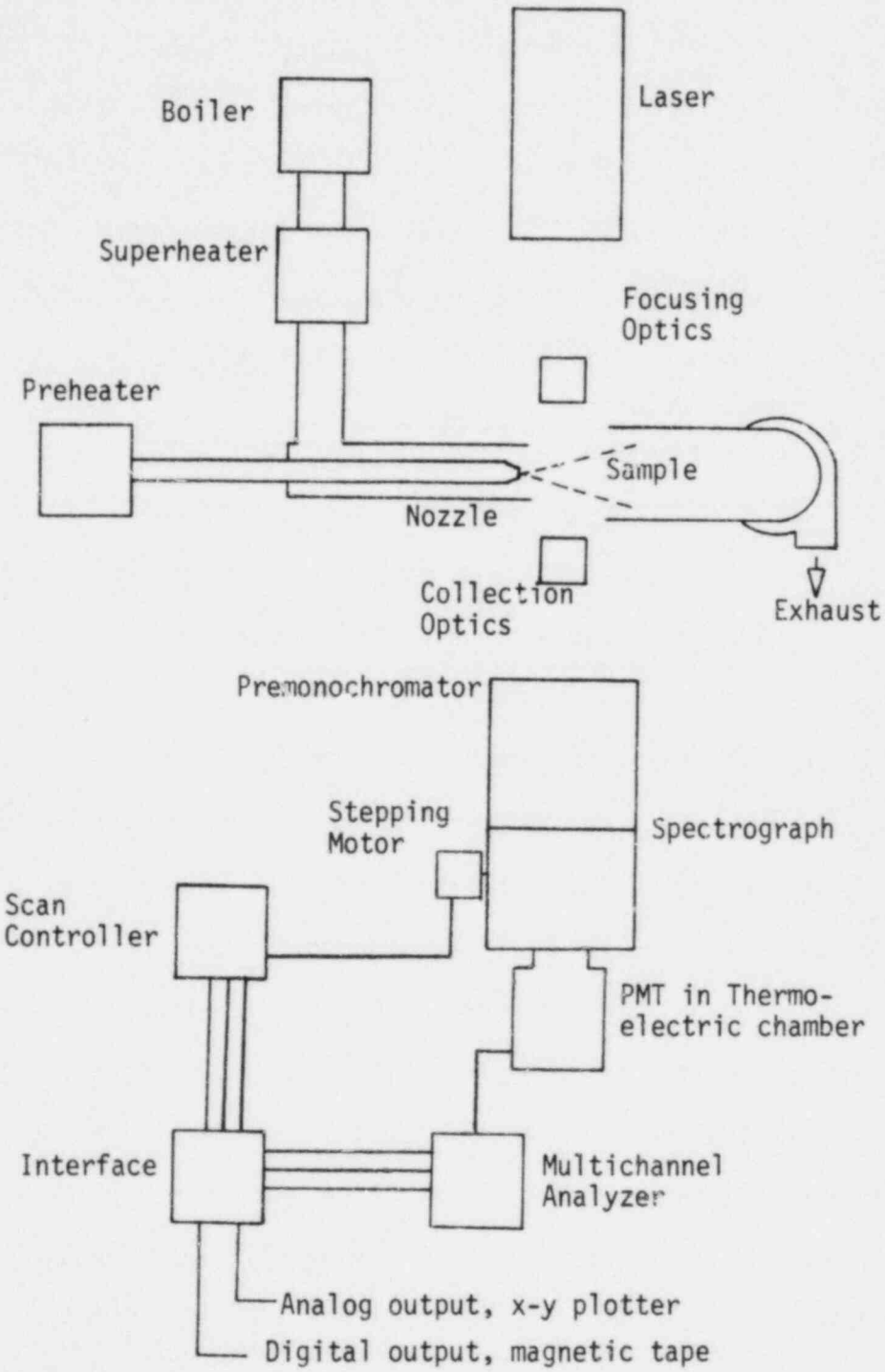

Figure 3.1 Raman system schematic

increment, the scan control interface delivers a synchronized channel advance pulse to the analyzer. Each channel on the analyzer corresponds to an increment of wavelength. Data is available for output in analog form to an x-y plotter or in digital form on magnetic tape for computer analysis.

3.3 Laser

A Spectra Physics model 164-09/265 Argon Ion Laser was used to irradiate the sample. Raman experiments were performed using the 488 nm laser line. A description of the laser specifications, power, and cooling requirements is given below. More detailed information is available from the Spectra Physics Instruction Manual [3.1].

The laser may be tuned for single or multiline operation. The maximum multiline output power is 5 watts; however, Raman applications require a monochromatic source. The two strongest emission lines are 488 and 514.5 nm. The maximum power for these lines is specified to be 1.5 and 2.0 watts respectively. Since the scattering intensity varies as the fourth power of the incident frequency, the 488 nm line is favored. In addition, selection of the 514.5 nm line would shift the Stokes vibrational band for steam further into the red region of the spectrum, where the optical response of most photodetectors is diminished.

Two laser control modes are available, current and light control. In the current control mode, the plasma current is regulated to maintain a constant value independent of line voltage fluctuations. In the current control mode, variation of the output power is less than

3 percent. In the light control mode, a silicon photodetector samples the output beam providing a feedback signal for current regulation. In the light control mode, the output power is regulated to within ±0.5 percent over the range 0.1 to 2.0 watts. All optic adjustments and alignment were performed in the current control mode, all spectra were acquired using the light control mode.

The laser requires a 208 volt, 3 phase electrical supply and draws up to 38 amps of current. The power supply and plasma tube are water cooled requiring a minimum flow of .14 Kg/s at a minimum pressure of 0.27 MPa.

After an estimated 1800 hours of operation, the laser power has dropped to approximately 77 percent of the manufacturers' specification. The operating power, measured using a Scientech model 3600 disc calorimeter, was .9 to 1.0 watts.

3.4 Irradiation and Collection Optics

Incident laser light is guided to the measurement volume by a pair of precision quality, plane laser mirrors. The laser beam is focussed on the sample by a single plano convex lens. Scattered light is collected and focussed on the premonochromater entrance slit by a pair of plano convex lenses.

The laser mirrors are 25.4 mm in diameter and have a broad band coating that produces reflectivity in excess of 99.9 percent. The laser focussing lens is 22.4 mm in diameter and has a 100 mm focal length. The lens material is optical crown glass which

transmits over 90 percent at 488 nm. A single layer anti-reflection coating reduces the reflectivity to less than 2 percent for normal incidence. The collection lenses are 38.1 mm in diameter and have a 76.1 mm focal length. The collection lenses are of UV silica, which transmits over 90 percent down to 200 nm. The UV silica was selected in anticipation of anti-Stokes observations in the deep-blue to near ultra-violet region of the spectrum.

The laser mirrors and collection lenses were obtained from Optics for Research. The laser focussing lens was supplied by Melles Griot.

3.5 Monochromator

The spectral intensity distribution of scattered light from the irradiated sample was observed using ar Instruments for Spectral Analysis (ISA) Model DL-203, f/4.2, triple monochromator. The system utilizes a 200 mm double monochromator as a prefilter for a plane grating spectrograph. The DL-203 is designed for applications requiring high stray light rejection. The premonochromator, operating in subtractive dispersion,transmits a selected spectral band to the spectrograph.

The optical path is shown in Figure 3.2. Light entering slit 1 (S_1) is dispersed across the plane of slit 2 (S_2) by the first grating (G_1). Light passing S_2 is recombined by the second grating (G_2) and focused on slit 3 (S_3). The exit slit of the premonochromator (S_3) serves as the entrance slit for the spectrograph. Light leaving the premonochromator is filtered but not dispersed. The

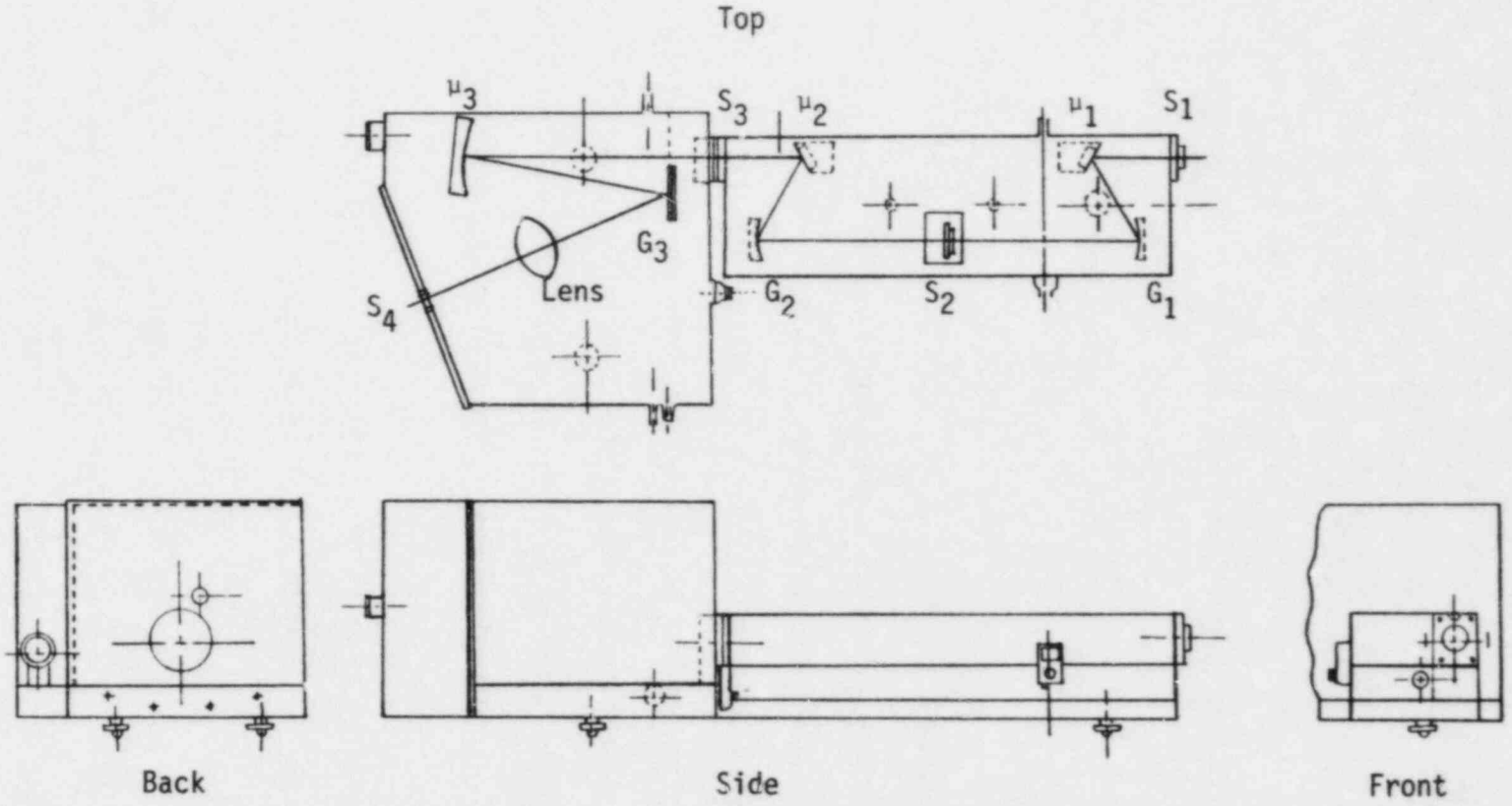

Figure 3.2 ISA-DL203 monochromator [3.2]

filtered light is collimated by a parabolic reflector (M_3) then dispersed by a plane grating (G_3) in the spectrograph. The dispersed image is focussed on the exit slit (S_4) by an output lens. Grating, G_3, is driven by the stepping motor, scanning the dispersed image past S_4 to produce the spectral intensity distribution.

For spectral analysis, the premonochromator bandpass is centered on the spectral region of interest. The spectrograph scans the desired spectral region. The microprocessor controlled scanning system (model #I98-0009) is a standard accessory supplied by ISA. The user sets upper and lower wavelength limits, scan speed and the number of repetitive cycles. The scanning system steps the spectrograph through the desired spectral range in 0.05 nm increments and performs backlash corrections.

The standard output lenses supplied with the monochromator have been replaced with Optics for Research UV silica lenses of the same focal lengths, 50, 105 and 200 mm, in anticipation of anti-Stokes measurements in the deep-blue to near ultra-violet region of the spectrum. The 200 mm output lens gives the maximum dispersion in the exit plane and was used for all work described in this report.

An assortment of various size slits is supplied with the monochromator. The slits are all 10 mm high and have assorted widths. Slit width determines the bandpass, spectral resolution, and light throughput. Spectral performance of the monochromator is described

in terms of bandpass and spectral resolution. The width of the spectral band transmitted to the spectrograph by the premonochromator defines the bandpass. The smallest observable spectral feature defines spectral resolution.

The width of the intermediate slit, S_2, determines the bandpass of the premonochromator but does not affect spectral resolution. The dispersion is 4 nm/mm in the plane of S_2. The bandpass may be varied from 2 to 80 nm by inserting the appropriate slit. The narrowest possible bandpass should be used for spectral analysis since stray light rejection capability diminishes as the bandpass is increased.

Spectral resolution of the monochromator is characterized by the slit function. The spectrograph integrates intensity over a finite wavelength interval as it scans. A spectral line of infinitesimal bandwidth appears as a band having a definite shape and finite bandwidth. The shape and width of the band define the slit function. Best spectral resolution is obtained when the width of the focussed image from the output lens matches the width of the exit slit, S_4. Scanning a rectangular image of uniform intensity past a rectangular slit of the same width produces a triangular intensity distribution. Spectral resolution is described by the full width at half maximum (FWHM) intensity of the slit function. Neighboring spectral lines are resolvable if they are separated by at least the FWHM.

Selection of slits S_1, S_3 and S_4 requires a trade-off of spectral resolution vs. signal strength. Observation of temperature effects on Raman vibrational contours requires spectral resolution on the order of 0.1 to 1.0 nm. The smallest slits supplied with the

monochromator give spectral resolution approaching the low end of this range. Slit size not only affects spectral resolution but also light throughput. Smaller slits limit the amount of light passing through the system, reducing the detected intensity.

An empirical approach was used for slit selection. A mercury vapor spectral calibration lamp (Ealing #26-4812) was observed with various size slits. Results of these observations indicate that light throughput and the FWHM of the slit function are roughly proportional to the size of slits S_1 and S_3 (see Figure 3.3). (Note: ISA recommends always using the same size slits in S_1 and S_3.) Final slit selection was based on preliminary Raman observations. The combination $S_1 = S_3 = 1$ mm, $S_4 = .167$ mm gave the best results. Attempts to gain better spectral resolution by using smaller slits reduced detected Raman intensities to marginal levels. Use of larger slits to increase signal strength caused a significant loss of spectral resolution. Figure 3.4 shows the 577, 579 nm yellow doublet of the mercury vapor lamp observed with the above slit combination. The slit function is approximately triangular with a FWHM of 0.6 nm.

Both the premonochromator and spectrograph utilize sinebar drive mechanisms so spectral analysis is conducted in terms of wavelength rather than frequency or wavenumber. The wavelength counters are accurate to within 2 nm over the visible spectrum. Figure 3.5 shows the distribution of wavelength counter error. This data was obtained using a mercury vapor spectral calibration lamp. Spectral data presented in this report is based on the

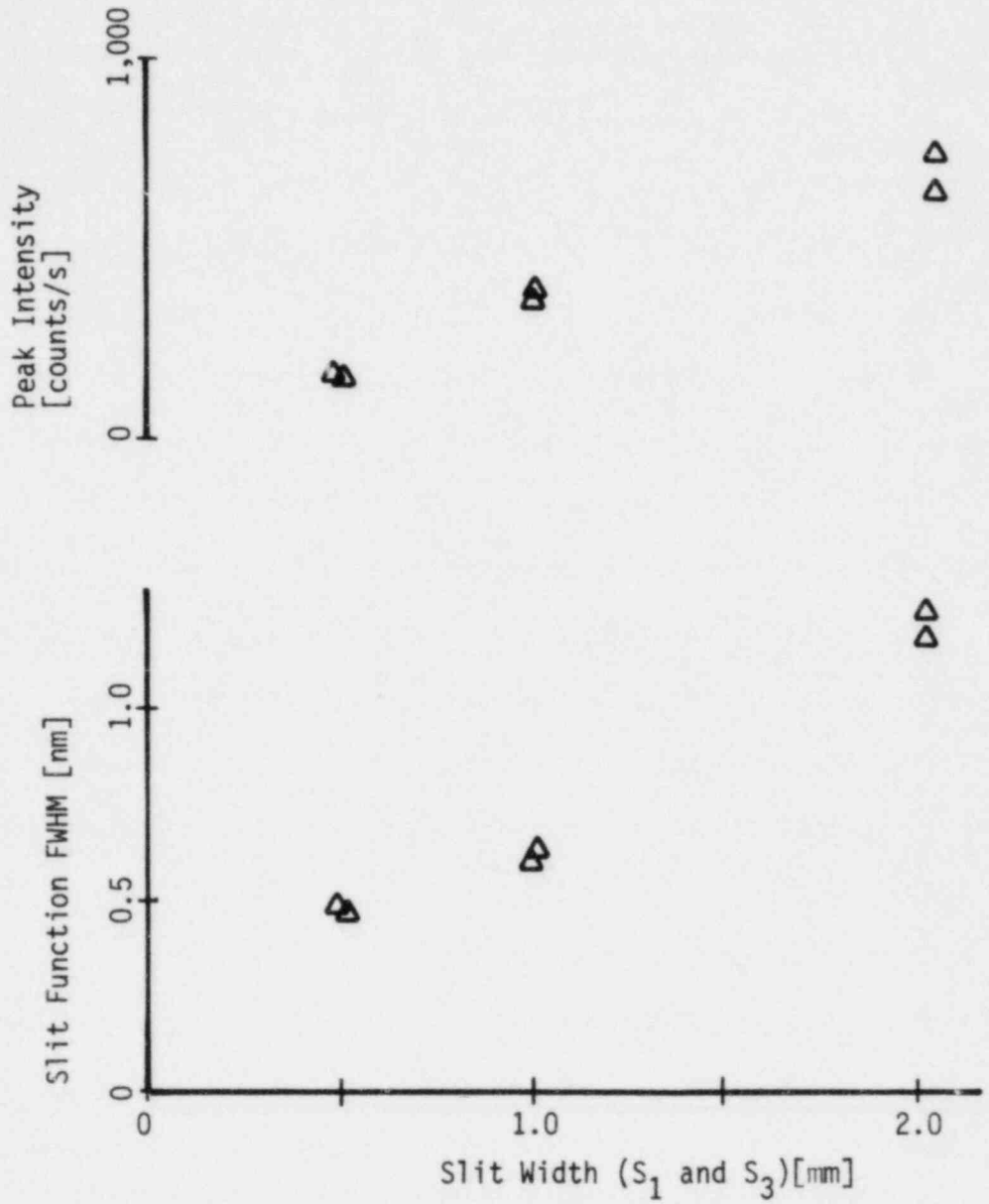

Figure 3.3 Slit selection data from observations of mercury vapor calibration lamp

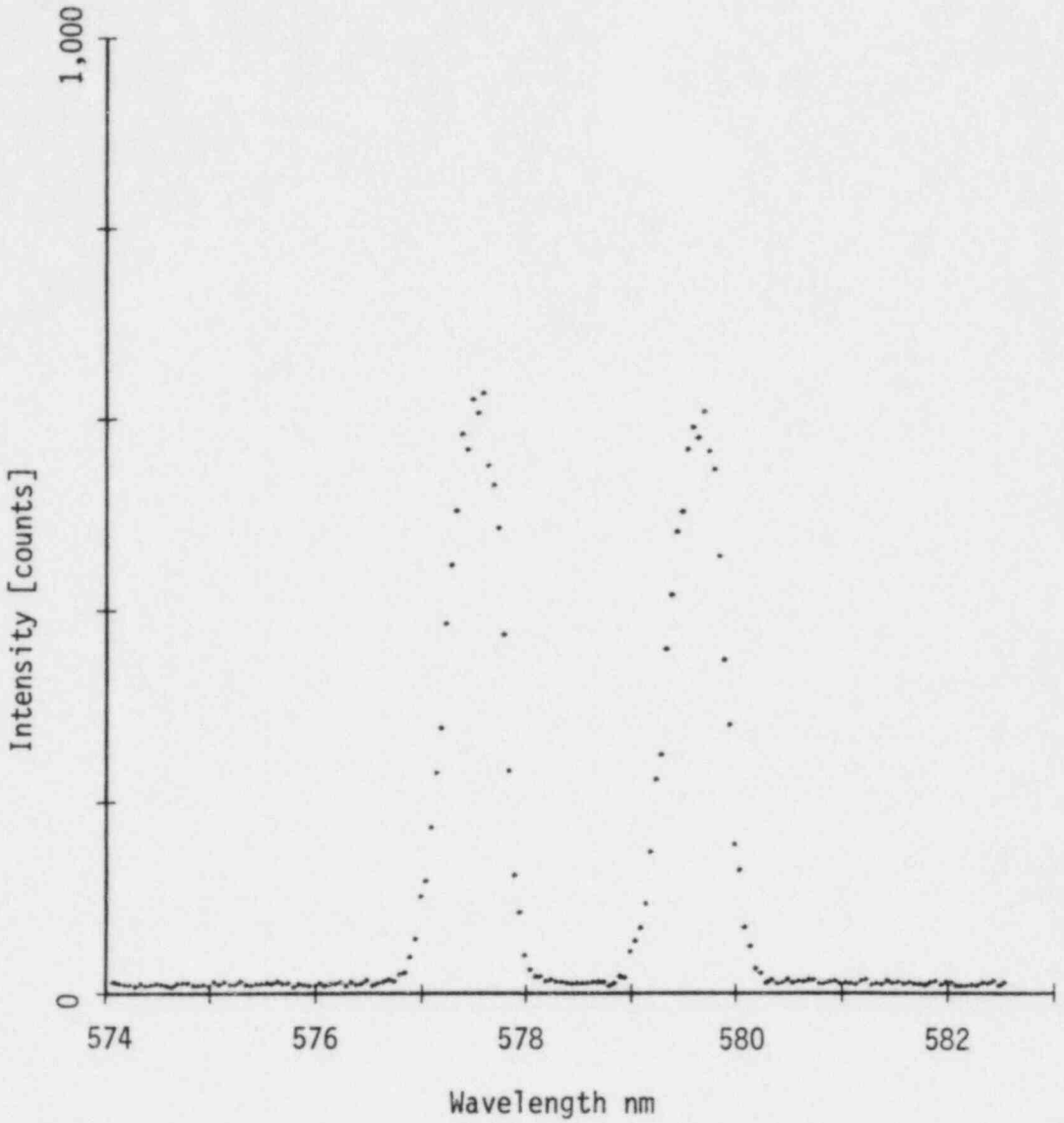

Figure 3.4 Spectrum of 577, 579 nm doublet for mercury vapor calibration lamp

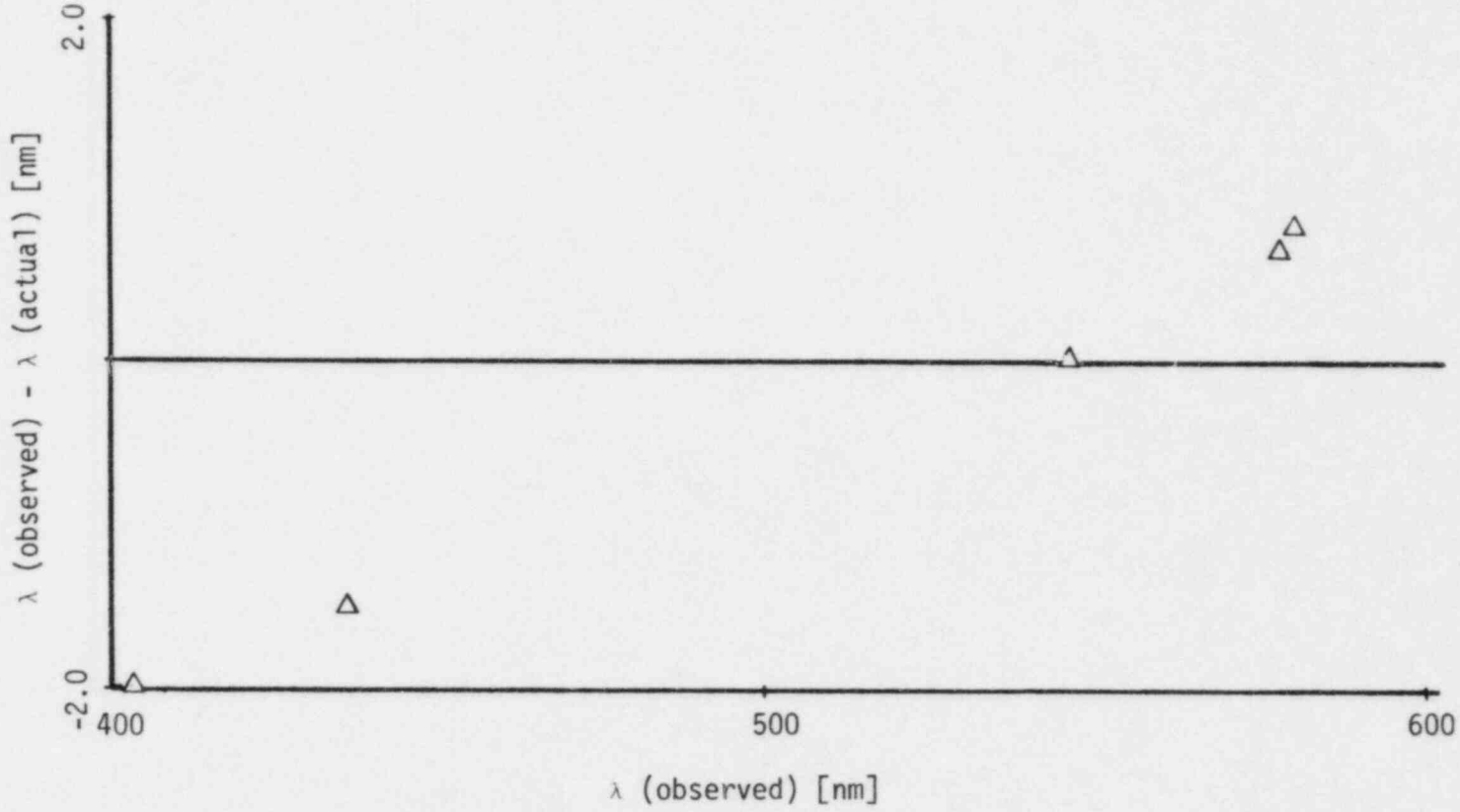

Figure 3.5 Distribution of monochromator wavelength counter error

counters with no correction applied. The premonochromator wavelength is reproducible to with ±0.4 nm. The spectrograph counter is accurate to within one increment of the stepping motor or ±0.05 nm.

3.6 Multichannel Analyzer

A Tracor Northern model 1705 multichannel pulse height analyzer (MCA) was used to process the photomultiplier output. The analyzer has two modes of operation, pulse height analysis (PHA) and multichannel scaling (MCS). The PHA mode was used to optimize the photodetection system for photon pulse counting. The multichannel scaling mode was used during system alignment for signal optimization and for spectral data acquisition.

The MCA has a charge sensitive preamplifier designed to accept negative current pulses from a photomultiplier anode. Input signals are processed and results stored in a 1024 channel solid state memory. Data is displayed on a cathode ray tube and is available as output in analog or digital form for plotting and computer analysis.

In the pulse height analysis mode, the analyzer receives a string of pulses from the photomultiplier tube. The pulses have amplitudes (heights) corresponding to the energy absorbed by the detector. The energy spectrum seen by the phototube is measured by sorting the pulses according to amplitude and forming a histogram [3.3]. Figure 3.6 illustrates pulse height analysis. Part a shows a simplified pulse train as it might appear at the MCA

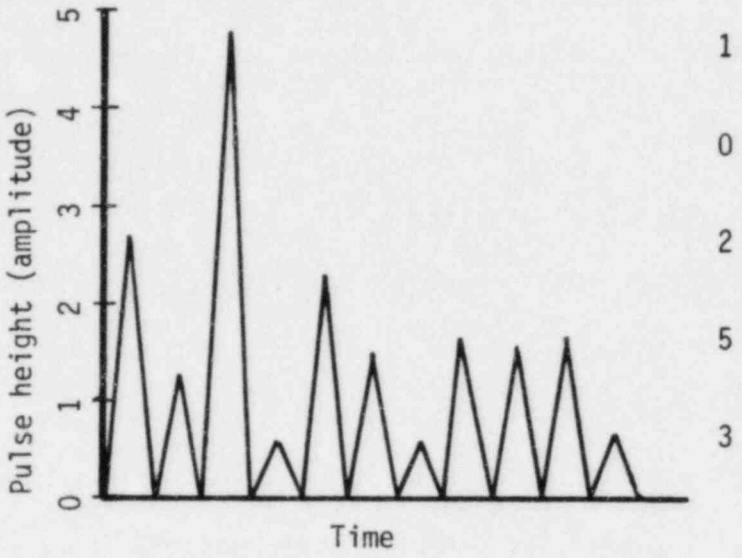

a) Sample pulse train

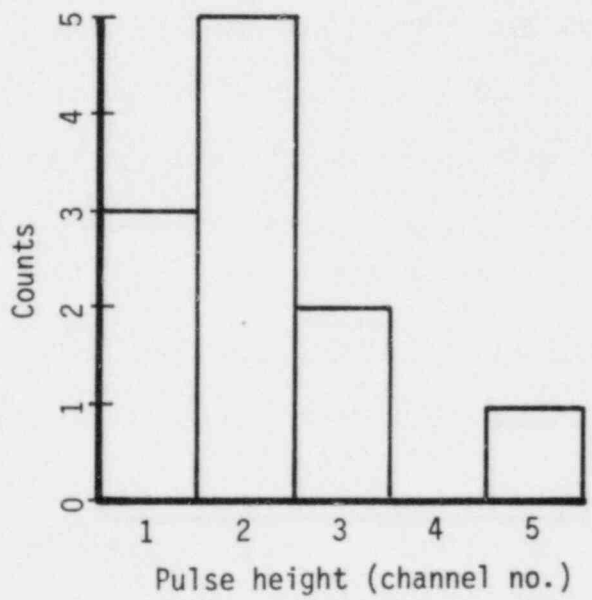

b) Pulse height distribution

Figure 3.6 Pulse height analysis

input. Pulse amplitude is divided into five equal increments. The number of occurrences of each amplitude is tabulated to the right. The pulse height distribution is shown in part b of Figure 3.6. The abscissa is divided into five channels corresponding to the five amplitude intervals. The number of occurrences of each amplitude is plotted, forming a histogram. The number of counts in each channel represents the number of occurrences of each amplitude. The pulse height distribution shows that six pulses occurred having amplitudes between one and two. In practice, the input pulse amplitudes are sorted into 1024 intervals as compared to five in this example.

The pulse height or amplitude is proportional to the energy seen by the detector. The MCA amplifier gain and discriminator threshold define an energy window. Optimization of the energy window for photon counting is described in Chapter 4.

Multichannel scaling produces a histogram showing the number of pulses vs. elapsed time. MCS differs from pulse height analysis in that all pulses are treated the same, no information regarding pulse amplitude is obtained. The pulses are considered to be logic pulses indicating occurrence of an event (detection of a photon). Pulses are counted in each channel for a selected dwell time. The dwell time may be based on an internal clock or on an external signal.

Figure 3.7 illustrates MCS data acquisition [3.4]. A train of pulses, as shown in Figure 3.7, part a, is presented to the

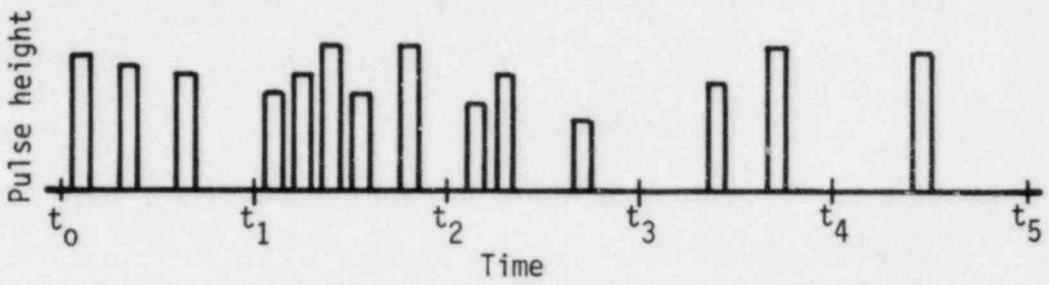

a) Sample pulse train

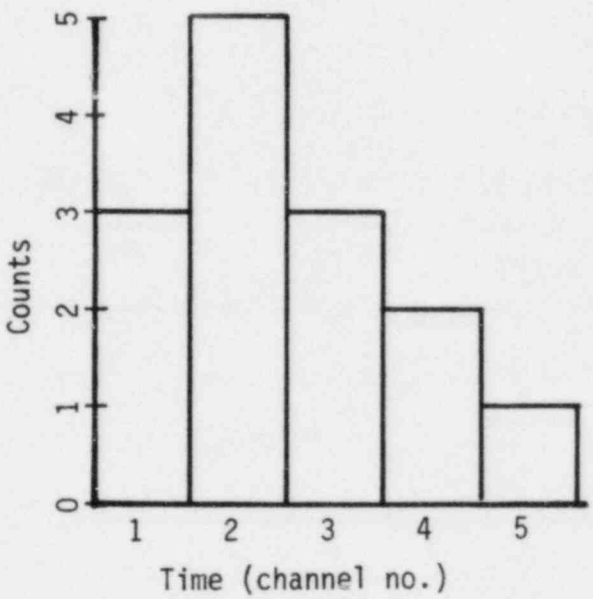

b) MCS histogram

Figure 3.7 Multichannel scaling

input. The input signal is divided into equal time increments with analysis beginning at t_0. The number of pulses in each time interval is counted and stored in successive channels. The resulting histogram, shown in part b of Figure 3.7, displays the number of pulses occurring in each time interval. The pulses may vary in height but will be treated the same and counted,provided that they remain within the selected energy window.

Normally, consecutive channels correspond to sequential time intervals, with channel advance triggered by an internal clock. Alternatively, the MCS sweep may be synchronized to an external device. For spectral analysis, the channel advance is synchronized to the stepping of the spectrograph grating. Then each channel corresponds to a wavelength interval and the pulses counted correspond to photons detected. The resulting MCS data is a spectral intensity distribution. More details on synchronized operation are presented with discussion of the scan control interface.

The analyzer is operated according to the manufacturer's instructions except for two slight modifications described below. The start analysis push button was connected to an unused pin (#9) on the MCA front panel connector,allowing remote analysis control. The 20 mA current loop, Teletype interface has been converted to a 1200 baud EIA-RS232 I/O port.

3.7 Photomultiplier Tube (PMT)

The RCA 8850 PMT is designed for low level light measurements such as photon counting. The PMT bias is provided by a Bertan

Associates model 215 regulated DC power supply. The PMT is cooled in a Products for Research, model TE-104-RF, thermoelectric chamber to reduce dark current.

The photomultiplier features a high gain gallium phosphide first dynode which provides pulse height resolution capable of resolving up to five photo-electron events. The pulse height distribution for a low intensity source breaks up into peaks corresponding to the detection of one photon, two photons, etc. rather than a single broad peak at the average pulse height [3.5]. The excellent pulse height resolution makes it possible to separate low energy thermal noise from pulses corresponding to detected photons.

The PMT is a 45.7 mm diameter, head on, 12 stage photomultiplier. The spectral response is shown in Figure 3.8. The wavelength of maximum response is 385 ±50 nm. The voltage divider network is shown in Figure 3.9. The PMT is operated with a 2000 volt bias because performance is well documanted for this potential [3.7].

The Bertan Associates model 215 power supply is a stable, accurate, high voltage DC supply. The output potential is variable from 0 to 3000 volts with positive or negative polarity. The maximum output current is 5 mA. The output voltage is regulated to within 0.001 percent with a ripple of less than 15 mV peak to peak. The voltage selector dial is calibrated to within ±1 percent plus 2 volts.

The thermoelectric chamber cools the PMT to 253 K, reducing dark noise approximately 60 percent below its room temperature

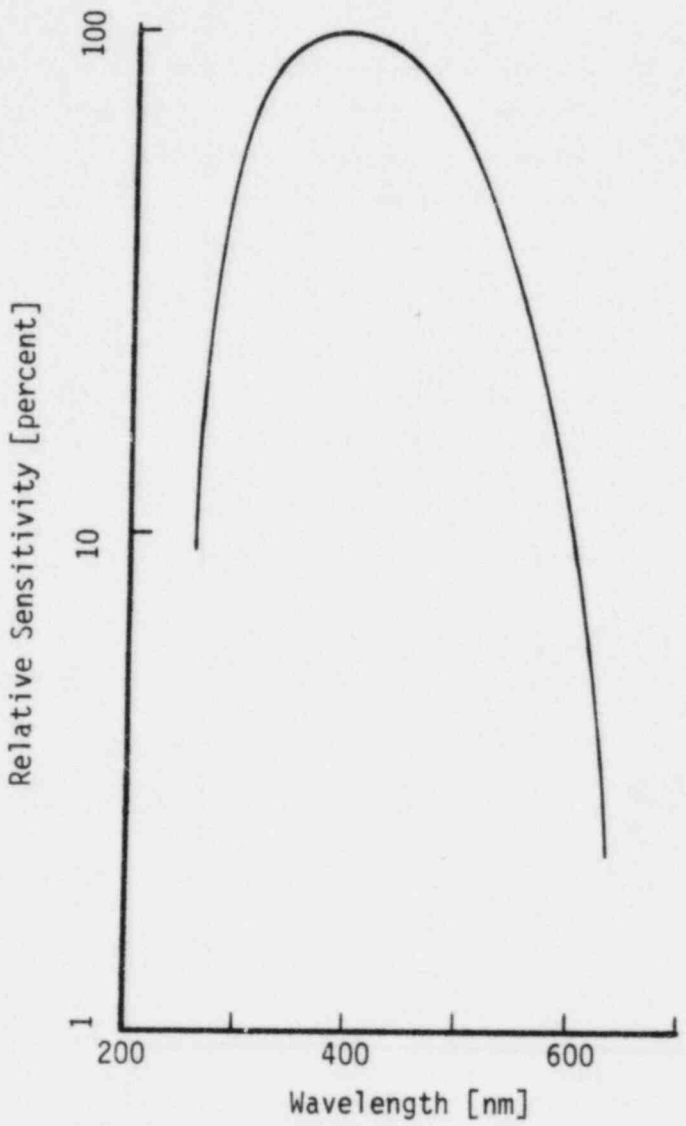

Figure 3.8 PMT spectral response [3.6]

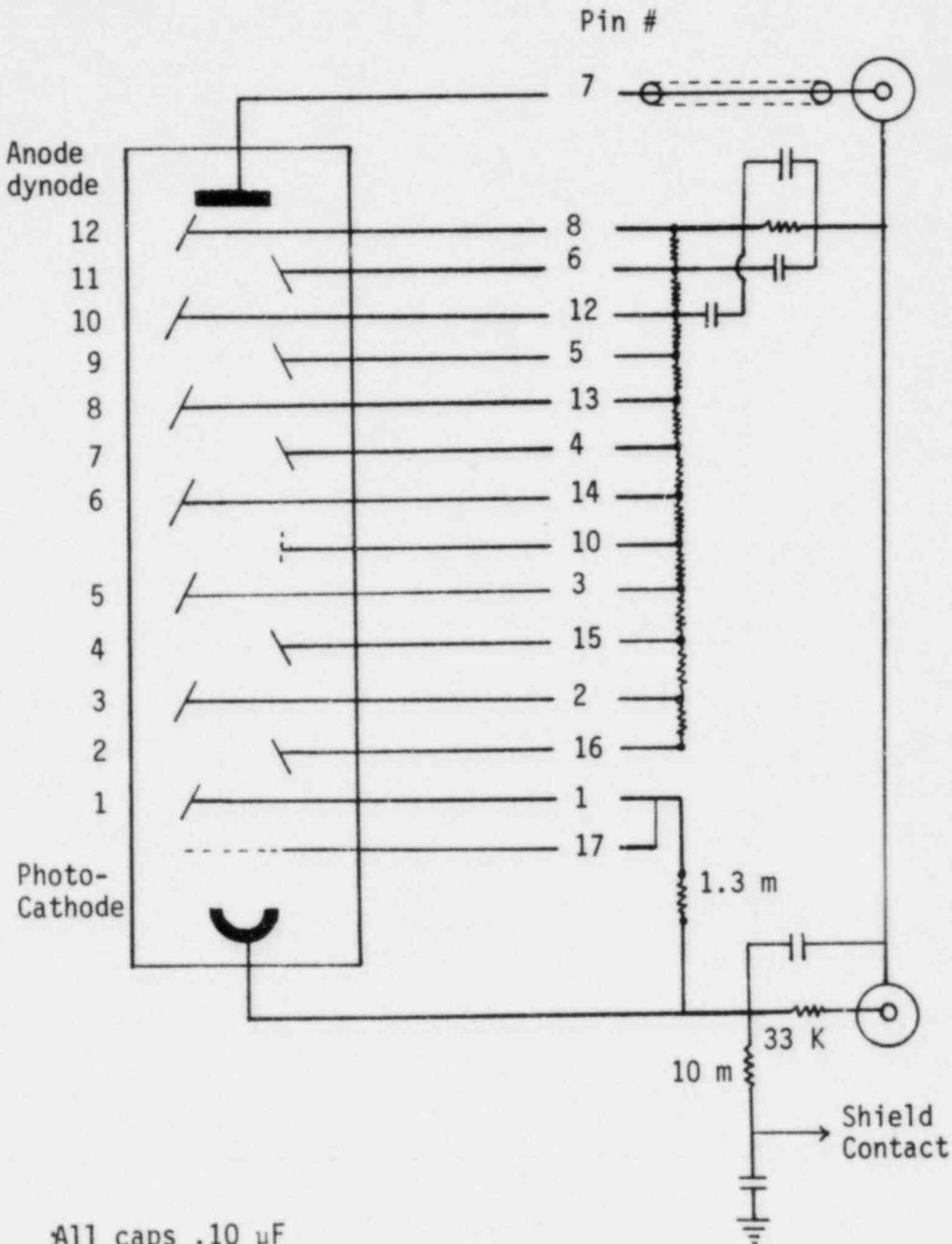

Figure 3.9 PMT voltage divider network

level. The chamber rejects heat to a water cooled heat sink which requires a minimum flow of 0.01 kg/s at room temperature.

3.8 Scan Control Interface

The scan control interface provides the link between the scan controller and the MCA. The interface serves two primary functions, to start and stop MCA data acquisition at the beginning and end of each scan and to coordinate the channel advance of the MCA with the spectrograph scan. The interface is also a convenient location for tapping analog and digital data outputs from the MCA. Figure 3.10 shows the interface with its associated connections. The interface is divided into a start/stop analysis circuit and a channel advance divider circuit. The design and operation of these circuits is described below.

The start/stop analysis circuit was designed to provide an appropriate signal for analysis control. This circuit sends a start analysis pulse to the MCA at the beginning of each forward scan cycle. A similar pulse stops data acquisition after each scan. The scan controller may be programmed for up to 99 repetitive scans. The start/stop analysis circuit starts and stops data acquisition for each scan causing the MCA to add successive scans and display accumulated data between scans.

The MCA start analysis input requires a quiescent 5 volt open collector source. When brought to ground for 15 microseconds, this signal causes analysis to change state, either starting or stopping data acquistion. Four LED's on the scan controller indicate the

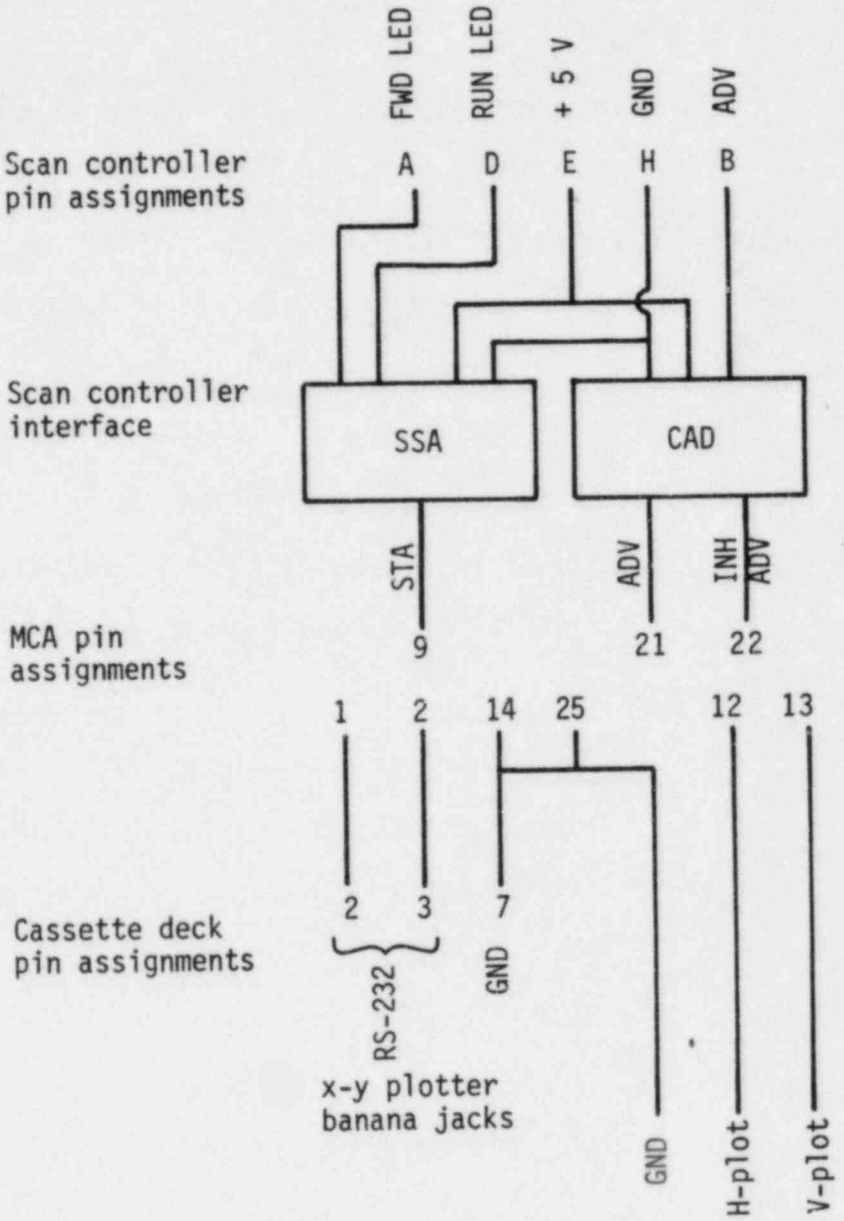

Figure 3.10 Scan control interface

status of the scan in progress. Two of these LED's provide the logic to control the start/stop analysis circuit which is shown in Figure 3.11.

The scan controller steps the spectrograph through the selected wavelength range. Each step advances the spectrograph 0.05 nm in wavelength. The multichannel analyzer accumulates photon counts in one channel during the dwell time between steps. When the spectrograph takes a step, the controller sends a synchronized channel advance pulse through the scan control interface to the MCA. Each channel corresponds to an interval of wavelength. The advance pulse is applied to the channel advance divider circuit which allows the operator to select frequency division by 1, 2, 4, 8, 16, 20, 40, 80 or 160. The channel advance divider permits variation of the wavelength increment corresponding to a single channel from 0.05 to 8 nm.

The channel advance divider circuit is shown in Figure 3.12. The circuit consists of a 7490 decade counter, a 7493 four bit binary counter and an arrangement of switches. The switches permit selection of a frequency division factor up to 160.

The inhibit advance input to the MCA enables external channel advance synchronization. Holding the inhibit advance signal at ground potential inhibits the internal clock. The inhibit advance switch on the scan control interface permits selection of remote control over the MCA with synchronized channel advance or manual control for time based channel advance. Opening the switch effectively disables the scan control interface. Manual control with

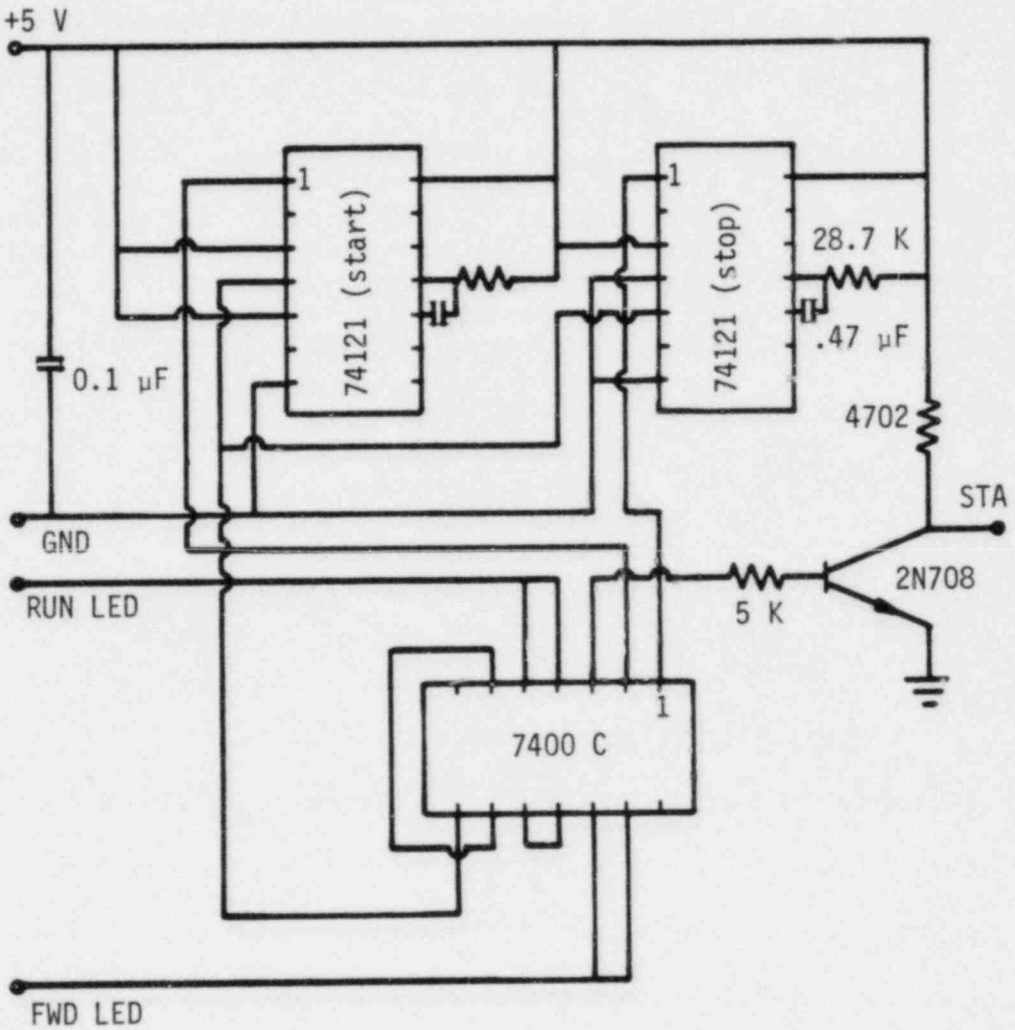

Figure 3.11 Start/stop analysis circuit

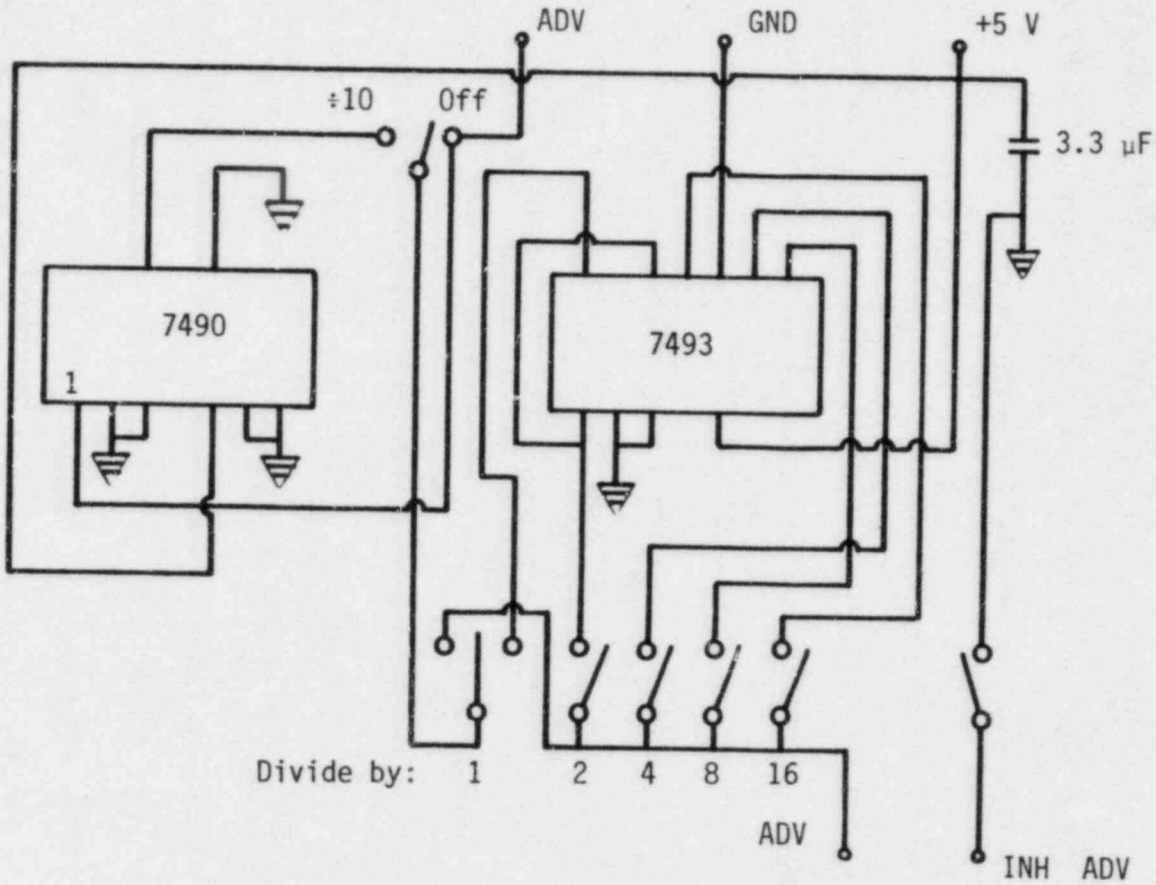

Figure 3.12 Channel advance divider circuit

time based channel advance was used during optics alignment for signal optimization.

Analog and digital data is transmitted to the interface from the MCA 25 pin "D" connector. Banana jacks are provided for analog output to an x-y plotter. The analog signal is 0 to 8 volts full scale. A 25 pin connector is provided for transmission of EIA-RS232 data to a Techtran model 717 digital cassette recorder.

3.9 Steam Generator/Atomizing Spray Nozzle

The purpose of this equipment is to provide superheated single and nonequilibrium two-phase steam samples at known temperatures. No attempt was made to model the thermal hydraulic conditions pertinent to nuclear applications. The plant is shown schematically in Figure 3.13. Single-phase steam samples are produced with up to 200 K vapor superheat ($T-T_{SAT}$, T_{SAT} = 373 K). The steam is mixed with an atomized spray of preheated liquid water droplets to produce nonequilibrium dispersed flow. Two-phase samples having a vapor to liquid mass flow ratio of 2.0 ±.05 are produced with up to 85 K nonequilibrium vapor superheat. The equilibrium quality of these samples ranges from 62 to 71 percent. The samples are not enclosed in a test section and are therefore at atmospheric pressure.

The steam generator is a Scott Engineering Sciences 2.4 KW benchtop boiler. Power is supplied by two banks of resistance heaters. Each bank is made up of three parallel .4 KW heater coils. The coils are switched independently for power selection. The voltage across the heater coils is unregulated. Two sight glasses

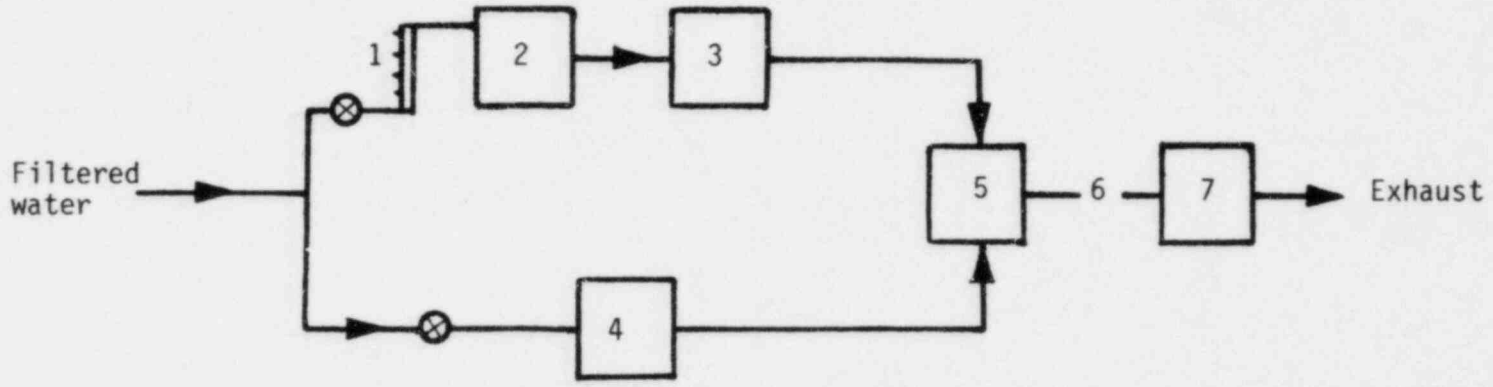

1 Rotameter
2 Boiler (2.4 KW)
3 Superheater (2.7 KW)
4 Preheater (1 KW)
5 Mixing nozzle
6 Sample
7 Exhaust duct and blower

Figure 3.13 Single/two-phase steam generator

and a needle valve are provided for liquid level control. Boiler temperature and pressure are monitored by a pressure gauge and two thermometers. The boiler was insulated to minimize heat losses. The inlet water was filtered to remove particles 5 microns or larger.

The superheater is made of a .75 m long, .051 m diameter steel pipe. The ends were capped with welded flanges. The heating element is a coil of Aeropack resistance wire (~20Ω/m). Resistance wire was also wound on the superheater inlet and outlet tubes as a guard heater. The superheater and tubing were insulated to minimize heat loss. The heating coil in the superheater carries half of the electrical load and the guard heaters on the inlet and outlet tubes each carry one quarter of the load. Power to these heaters may be varied continuously from 0 to 1.7 KW. The voltage across the heater elements is adjusted manually using a 220 volt single-phase Genrad Variac.

The preheater for the liquid spray is a 1 KW open pot boiler. The liquid flows through a 17 mm diameter, 500 mm long copper tube which was wound in a coil and submerged in boiling water. Liquid water was supplied to the spray nozzle at 338 to 348 K. The flow to the spray nozzle was monitored and regulated using a pressure gauge and needle valve.

The mixing nozzle is shown in Figure 3.14. Steam and liquid flow cocurrently through concentric tubes to the mixing region. The liquid is atomized by an oil burner fuel nozzle (Hago 2.50, 45°). Steam flows around the nozzle, mixing with the droplets before

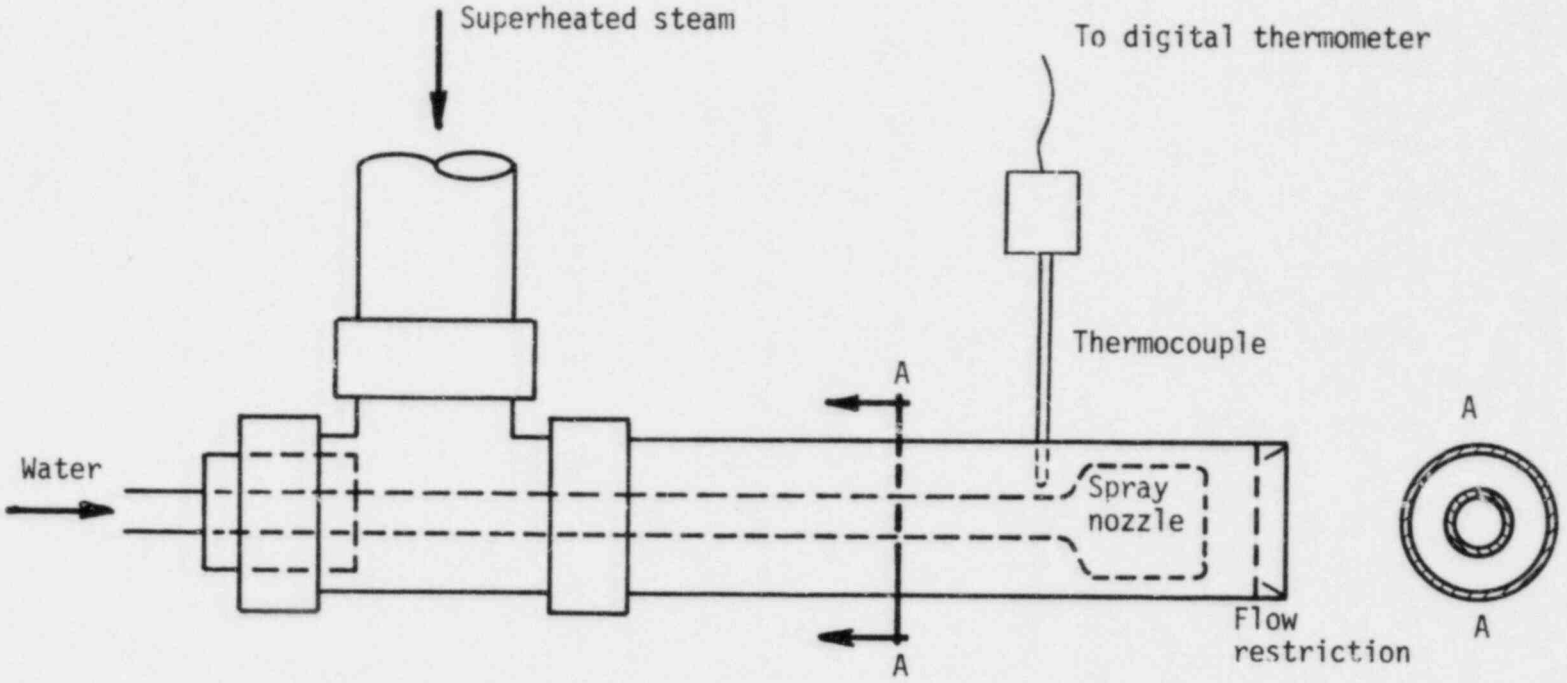

Figure 3.14 Steam/droplet mixing nozzle

entering the sample volume. The nozzle body has been turned down to 12 mm diameter to fit into the 15.8 mm diameter tube, leaving room for the steam to flow. A restriction reduces the flow area of the exit to increase the fluid velocity and concentrate the jet axially.

The steam flow is not enclosed in any kind of test section, eliminating the problem of quenching on walls and windows. Use of an unenclosed flow sample requires that the mixing nozzle produce a concentrated axial jet. The jet must be well defined to limit dilution of the sample by surrounding air.

An exhaust duct collects the steam and droplets downstream of the measurement point. A centrifugal blower draws the steam into a 76 mm diameter exhaust duct. The duct entrance is positioned about 20 mm downstream of the nozzle. The blower draws roughly 10 times the maximum volumetric output of the steam plant. Room air is drawn into the exhaust duct with the steam, cooling the flow. The steam condenses in the duct and is collected for disposal.

The steam generator is monitored and controlled manually. The boiler is operated at maximum power. The inlet flow is fairly unsteady, varying from .3 to 1.5 gm/s. The boiler reservoir is half filled with air providing a capacity to absorb inlet flow variations. The inlet valve is adjusted as necessary to maintain a constant liquid level in the boiler. The steam temperature is monitored at the nozzle inlet by a 1.5 mm diameter sheathed thermocouple (shown in Figure 3.14). The Variac which powers the superheater is adjusted to maintain a constant steam temperature. The plant requires a 30 to 45 minute warmup period from the time steam is

first generated to obtain steady conditions. With practice, the operator can stabilize the plant to maintain steady conditions with minimal adjustment to the Variac and control valves. Pressure in the boiler remains fairly constant (.116 ± .0024 MPa) over a wide range of operating conditions. The outlet temperature can be regulated to within a 10 K range for single-phase steam and a 20 K range for two-phase operation.

The heat loss from the boiler was estimated to be 30 watts or 1.25 percent of the input power. A heat balance on the boiler was used to calculate the steam mass flow rate. The boiler produces .91 to .92 gm/s of saturated steam at .116 MPa. The mass flow rate through the spray nozzle was measured by collecting droplets over a known period of time and weighing the liquid. The flow rate was .485 ± .18 gm/s for a .225 MPa pressure drop across the nozzle. The large uncertainty in the liquid flow rate is due to variations in the flow resistance of the nozzle. The nozzle consists of an outer shell and an inner core. The core moves within the shell when the flow is turned on or off, changing the flow resistance slightly.

Correlation of temperature effects on Raman data requires knowledge of the temperature in the scattering volume. Insertion of a thermocouple or similar probe into the scattering volume would interfere with Raman observations. The temperature in the scattering volume could not be monitored simultaneously with Raman observations. The steam generator operating conditions were monitored

during Raman experiments. The temperature in the scattering volume was measured, using a 2.2 mm diameter differentially aspirated thermocouple probe [3.8] in a later calibration run for the same operating conditions.

Calibration data for both single and two-phase operation indicate that the sample temperature is linearly related to the mixing nozzle inlet temperature (see Figures 3.15, 3.16). The single-phase data were verified to within 4K with a 1.5 mm diameter sheathed thermocouple. Temperatures assigned to Raman spectra were based on the correlations of Figures 3.15 and 3.16.

3.10 Summary

This chapter introduced the Raman system developed for this research. The components which make up the system have been described. Temperature measurements used to correlate Raman spectral data to temperature were presented.

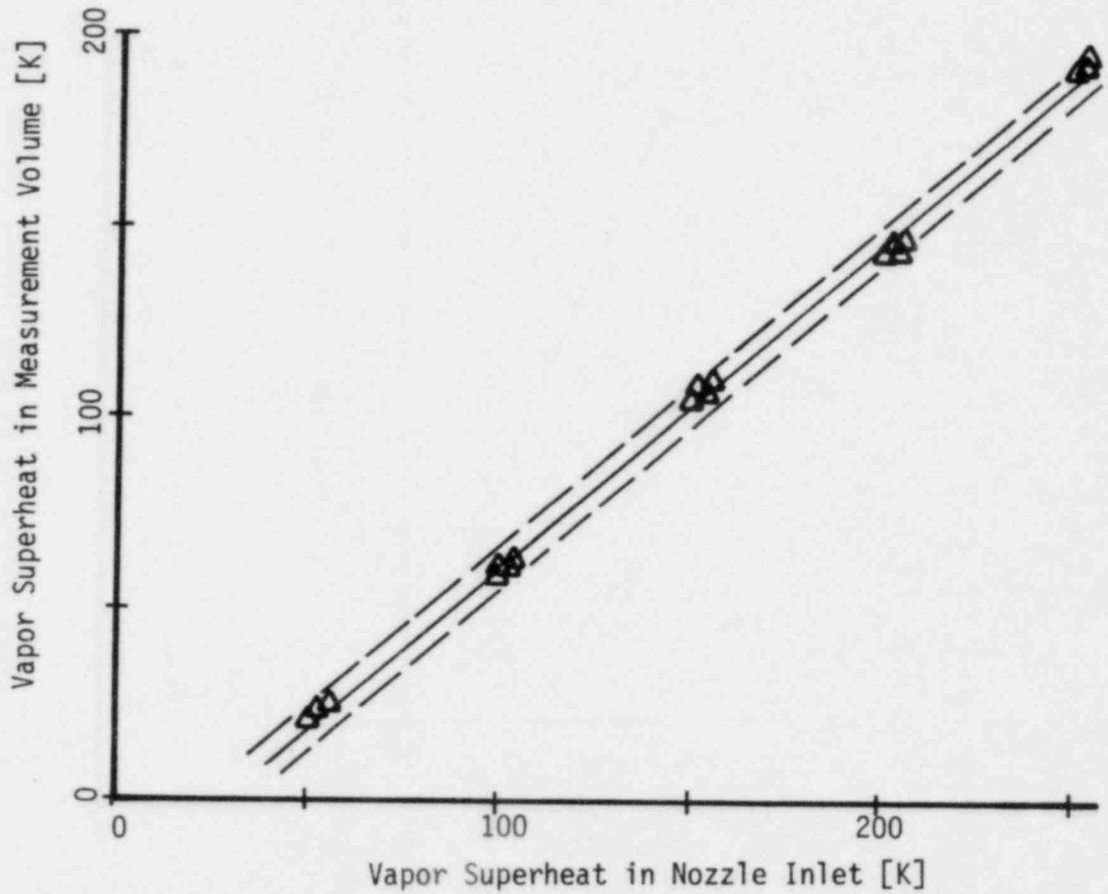

Figure 3.15 Temperature correlation for single-phase samples (Vapor superheat = $T-T_{SAT}$, T_{SAT} = 373 K)

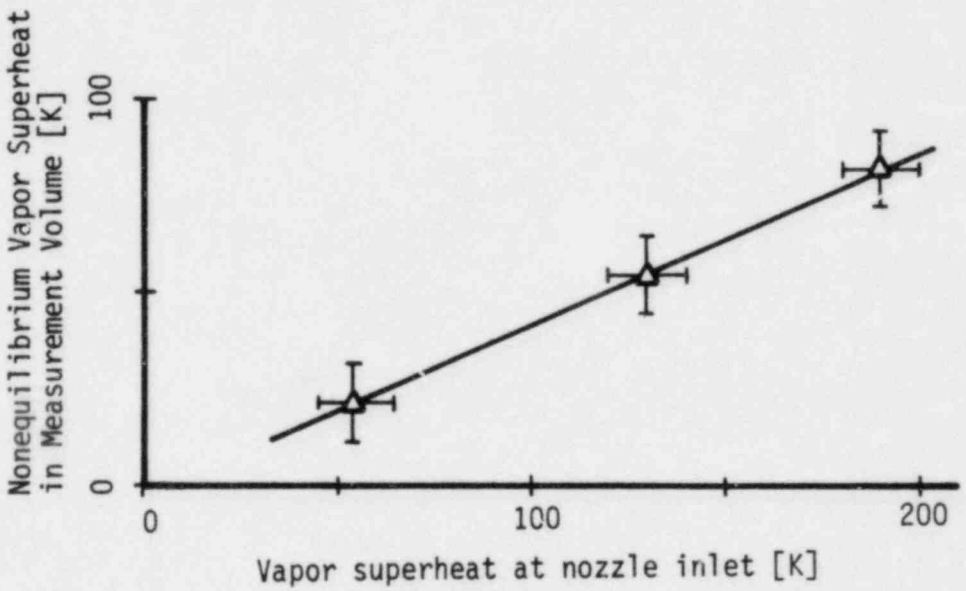

Figure 3.16 Nonequilibrium vapor temperature correlation for two-phase samples (vapor superheat = $T-T_{SAT}$, T_{SAT} = 373 K)

4. SYSTEM DEVELOPMENT AND OPERATION

4.1 Introduction

The Raman system developed for this research consists of three major subsystems.

1. Irradiation system
2. Spectral discrimination system
3. Photodetection system

The development and operation of each subsystem is described in this chapter.

Initial setup of the irradiation and spectral discrimination systems requires alignment of optical components. Alignment of optics was accomplished in two steps. The system was first approximately aligned by estimating the optimal position of each component. A signal optimization procedure was then used to refine optical alignment. Approximate alignment techniques are described in Sections 4.2 and 4.3. The signal optimization procedure leading to final optical alignment is described in Section 4.5. System development also includes optimization of the photodetection system for photon pulse counting. Selection of the MCA amplifier gain and discriminator threshold were based on observation of a controlled light source. This procedure is described in Section 4.4.

4.2 Irradiation System

The irradiation system includes the laser, beam steering mirrors, focusing lens and associated positioning devices. The irradiation

system delivers focused laser light to the sample. The path of the laser beam through the sample defines the scattering volume. The irradiation system is shown in Figure 4.1 along with the Cartesian coordinate system to be used in further discussion. The x axis is taken parallel to the original laser beam. The y axis is parallel to the vertical segment of the beam. The z axis is normal to the x-y plane.

Lens A focusses the laser beam in the sample. Focussing the beam improves spatial resolution by reducing the diameter of the scattering volume. The lens is mounted on a traverse to allow optimization of its position along the laser beam. An iterative procedure was used to align lens A and the traverse with the x axis. The laser was held fixed. A temporary target was placed at the center of the beam approximately 0.5 m in front of the laser. The lens and traverse were placed between the laser and target. The lens was centered, normal to the laser beam so the beam was not deflected from its original path. Movement of the traverse in the x direction revealed misalignment by deflection of the laser beam. The lens and traverse were aligned iteratively by minimizing the deflection of the laser beam while traversing the lens along the x axis. Upon completion of this procedure, the lens was centered, normal to the laser beam and the traverse was aligned with the x axis. Movement of the traverse translates the lens and its focal point a corresponding distance along the laser beam. Final adjustment of the traverse was based on signal optimization to be described in Section 4.5.

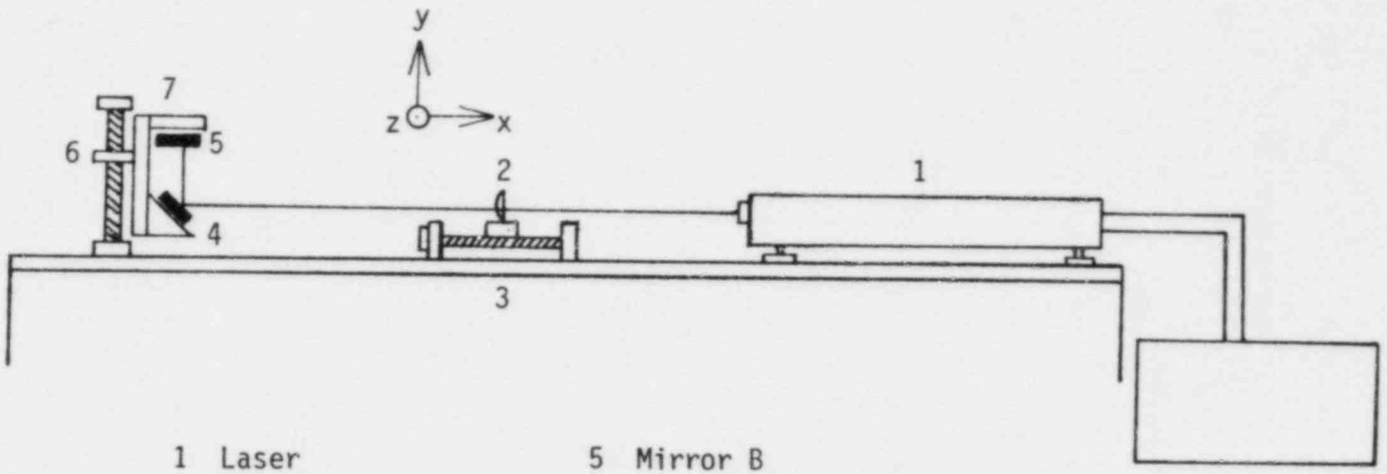

1 Laser
2 Lens A
3 Horizontal traverse
4 Mirror A
5 Mirror B
6 Vertical traverse
7 Angular micropositioner

Figure 4.1 Irradiation system

Mirror A turns the laser beam 90° so it propagates vertically. Vertical orientation allows the use of simple collection optics to image the scattering volume onto the monochromator entrance slit. Mirror B directs the beam back through the scattering volume to the laser. Returning the beam through the scattering volume to the laser doubles the incident intensity in the sample. Previous researchers [4.1] have increased observed Raman intensities using this technique. Improvements have been reported from a factor of 2 for a plane mirror to a factor of 90 for carefully constructed light trapping cells.

Mirror B is mounted on a two axis angular micropositioner about 100 mm above the scattering volume. The angular position was adjusted to maximize the intensity in the scattering volume. The mirror was first aligned visually, so the laser beam retraced its path back to the laser output optic. Fine mirror adjustments were made to peak the laser power meter.

Returning the beam to the laser through the scattering volume approximately doubles the incident power. It is difficult to confirm the actual laser output power when operating with the beam doubled back on itself. The internal laser power meter is actuated by a photodiode which samples the output beam. Higher power meter readings indicate an increase in the actual output power but may be partly attributed to incidence of the returning light on the photodiode. Spectra observed with and without mirror B in place differ in intensity by approximately a factor of two.

Mirrors A and B are mounted on a single vertical traverse. Movement of this assembly translates the scattering volume in the horizontal (x) direction. This adjustment simplifies alignment of the irradiation system with the spectral discrimination system.

4.3 Spectral Discrimination System

The spectral discrimination system includes the collection optics, monochromator and scan controller. Its purpose is to observe the spectral intensity distribution of light scattered from the irradiated sample.

The spectral discrimination system is shown in Figure 4.2. The scattering volume is a segment of the laser beam approximately 10 mm long and 1 mm in diameter. The collection optics image the scattering volume on the monochromator entrance slit. The spectrograph scans a selected spectral band to produce the intensity distribution.

The primary considerations in design of the light collection optics were simplicity and collection efficiency. The simplest collection system consists of a single lens placed on the optical axis of the monochromator. The optimal position of the collection lens was estimated using a back illumination technique. This procedure was used to match the lens position to the monochromator acceptance angle.

The back illumination technique is illustrated in Figure 4.3. The photomultiplier was removed from the spectrograph. A 2.4 mW Helium Neon (HeNe) alignment laser was directed into the monochromator through the exit slit (S_4). The position of the laser

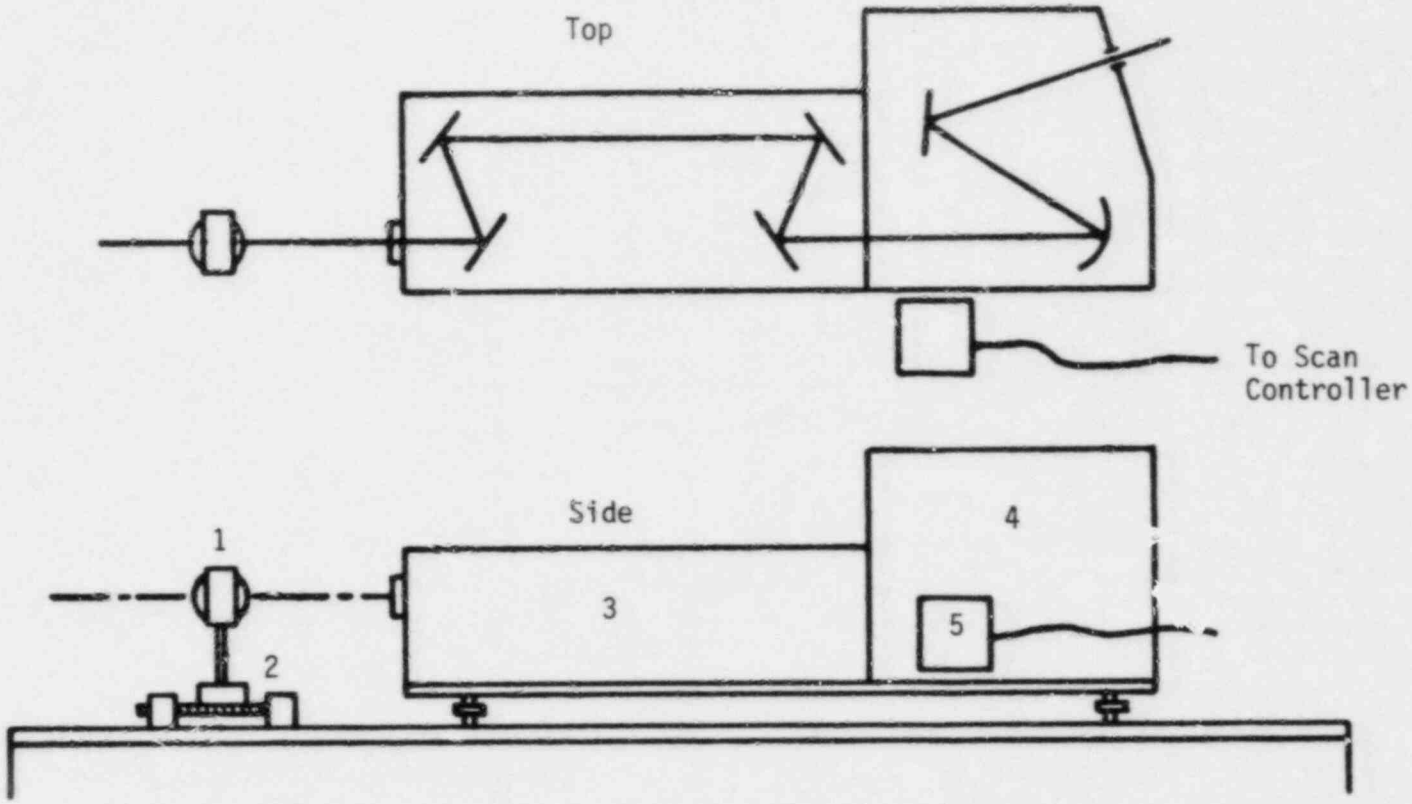

1 Collection Lenses
2 Horizontal traverse
3 Premonochromator
4 Spectrograph
5 Stepping motor

Figure 4.2 Spectral discrimination system

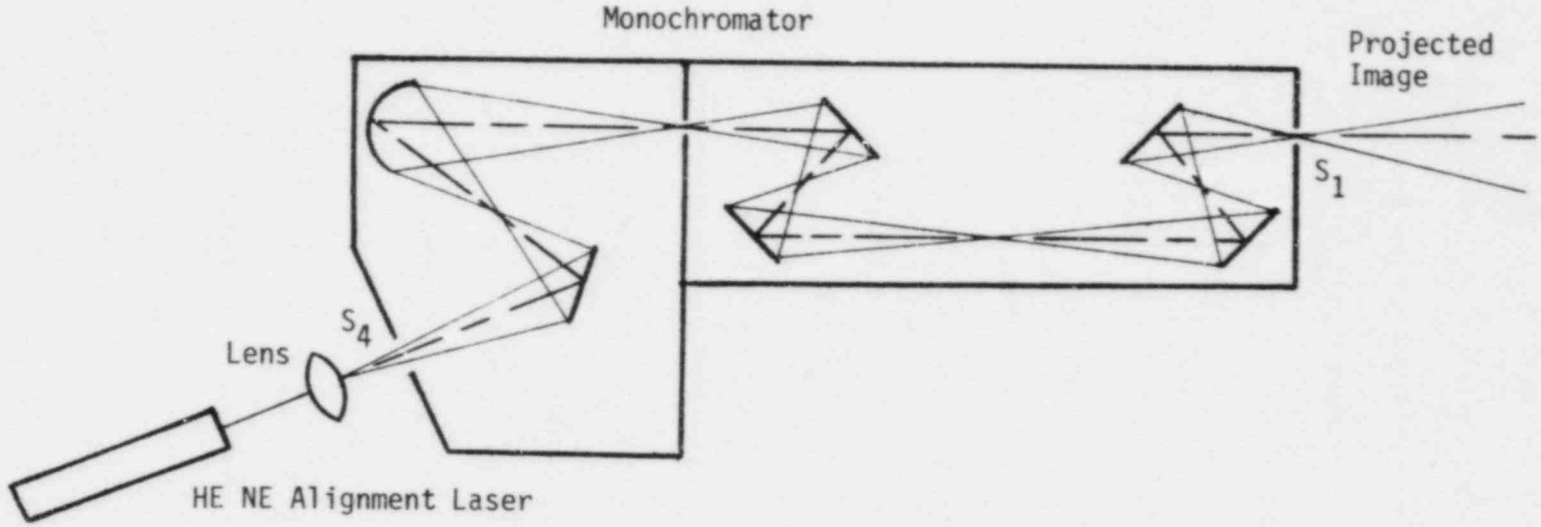

Figure 4.3 Back illumination geometry

was adjusted so the laser beam emerged from the monochromator entrance slit defining its optical axis. A lens was placed between the alignment laser and the monochromator to defocus the beam. The diverging beam covered the monochromator exit slit which served as the back illumination source.

The image projected from the monochromator entrance slit was used to estimate the optimal position of the collection lens, as shown in Figure 4.4. The lens was placed at the distance, d_1, from the entrance slit, where the height of the projected slit image was equal to the diameter of the lens. The solid angle or cone of acceptance was estimated by finding the location where the projected image focused to a point. For the single lens configuration, d_1 was 130 mm and d_2 was 125 mm. The solid angle is 0.073 ster.

Further development of the collection optics led to use of a two lens configuration as shown in Figure 4.5. The observed scattering intensity is proportional to the solid angle subtended by the collection optics. The solid angle may be increased significantly by adding a second lens. The space between lenses B and C determines the effective aperture of the lens combination. The optimal position of the additional lens was found by using back illumination to observe the solid angle for various lens positions. A 5 mm space between the lenses gives a near optimal solid angle of 0.53 ster. For this configuration, d_2 is 54 mm. The effective diameter of the lens combination is 37 mm. The resulting solid angle is about a factor of 7 larger than that of the single lens configuration.

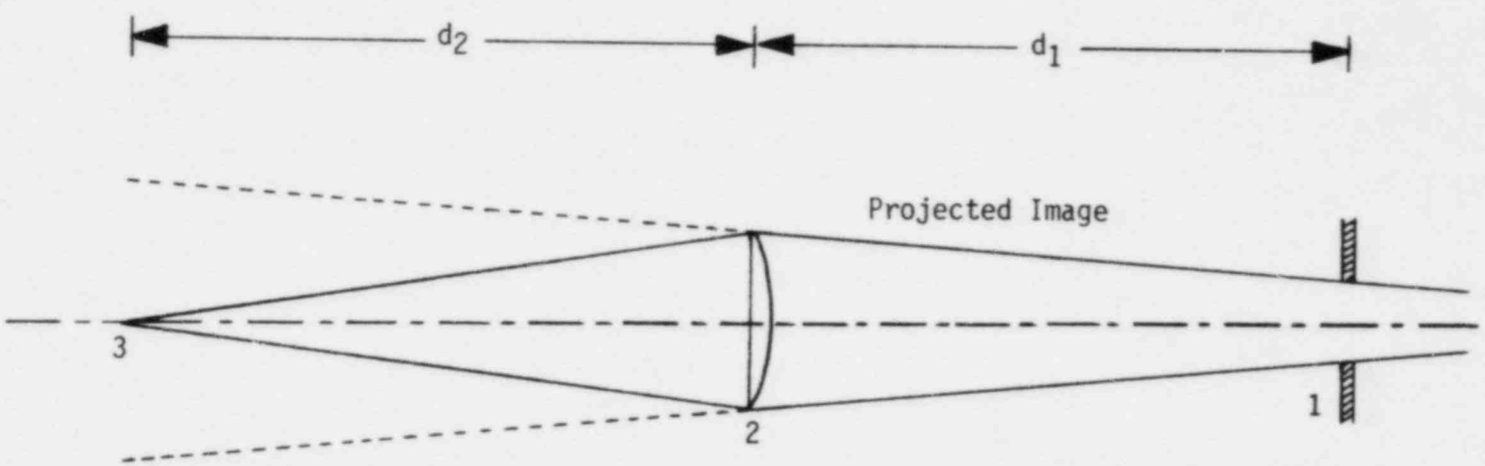

1 Monochromator slit S_1
2 Collection lens B
3 Focus point

Figure 4.4 Single lens collection geometry

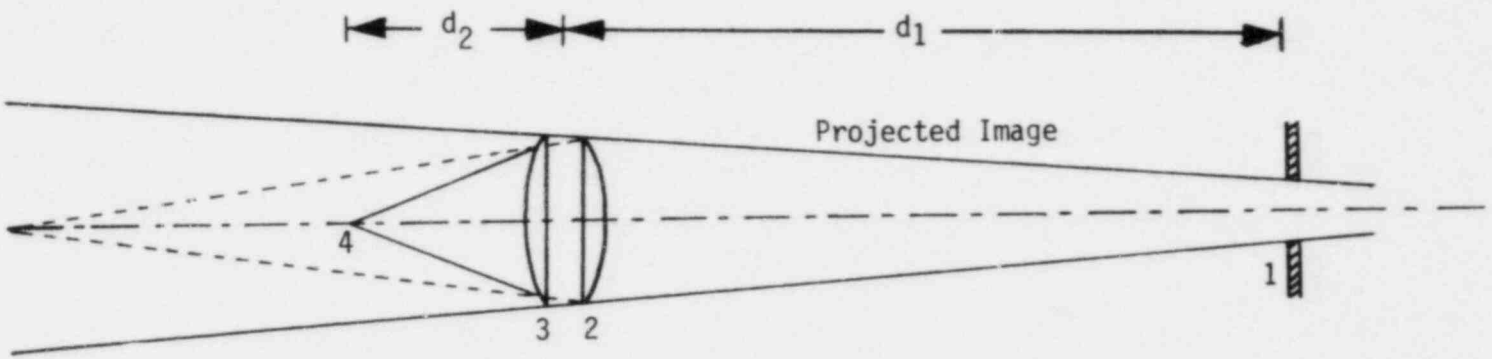

1 Monochromator slit S_1
2 Collection lens B
3 Collection lens C
4 Focus point

Figure 4.5 Dual lens collection geometry

The lenses were installed in a plexiglass holder to maintain a 5 mm space between them. The collection lenses were mounted on a traverse which moves along the monochromator optical axis to allow further optimization of their position.

Having established approximate relative positions for the illumination and collection optics, the spectral discrimination system was aligned with the irradiation system as shown in Figure 4.6. The HeNe alignment laser was again directed backward through the monochromator as in the previously described back illumination procedure (Figure 4.3). The lens used previously to defocus the laser was not used here. The HeNe laser beam was used to visually align the monochromator optical axis with the scattering volume and parallel to the z axis. The monochromator was placed 175 mm from the x-y plane (d_1+d_2 as determined for the two lens collection optics). The vertical traverse which carries laser mirrors A and B was adjusted to bring the scattering volume on line with the monochromator axis.

The collection optics, mounted on their traverse were centered, normal to the monochromator optical axis, 45 mm from the scattering volume. A target was used, as with the laser focusing lens, to align the collection optics and traverse with the monochromator axis. The procedure was to minimize the deflection of the HeNe laser beam. The traverse allows for final adjustment of the collection optics based on signal optimization.

4.4 Photodetection System

The photodetection system includes the photomultiplier tube (PMT),

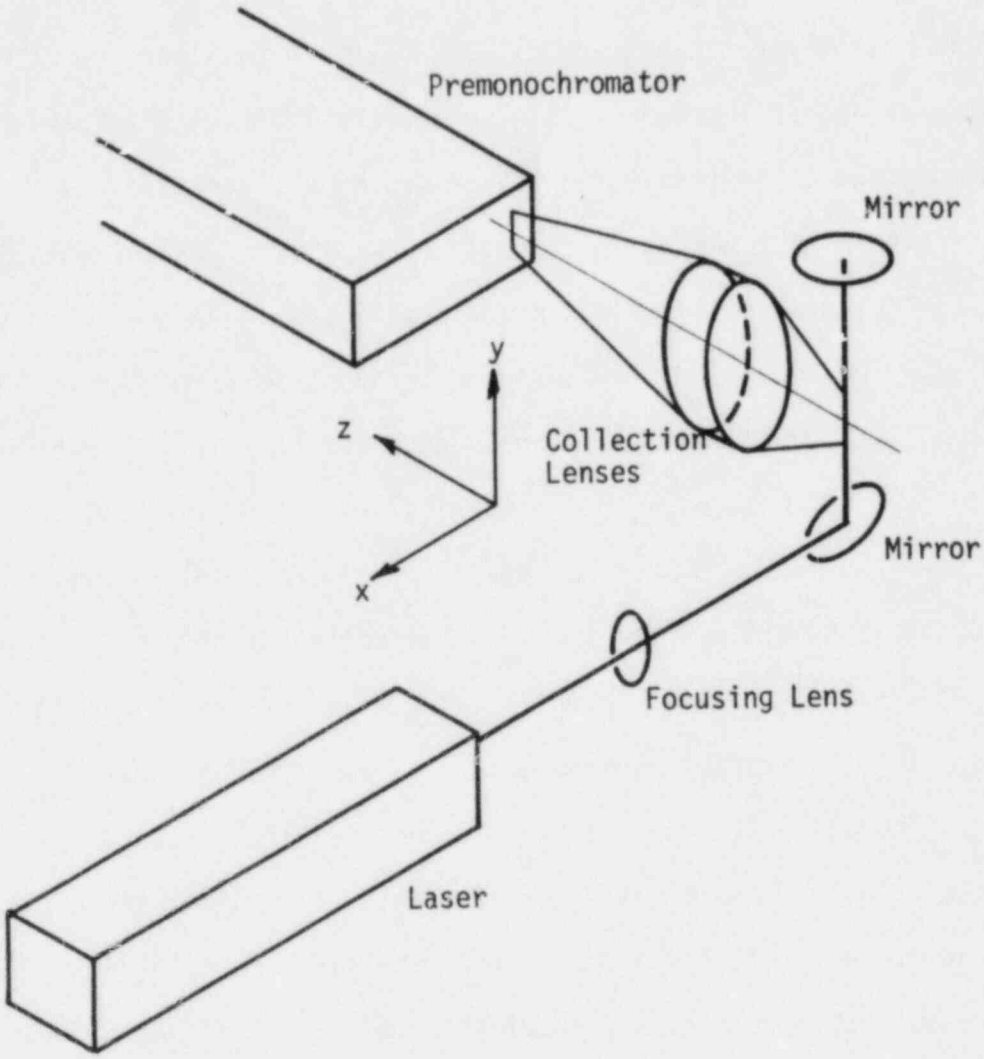

Figure 4.6 Raman system optical configuration

multichannel analyzer (MCA), and scan controller interface. The photodetection system converts the spectral intensity distribution into electronic signals.

The PMT detects individual photons which are counted by the MCA operating in the multichannel scaling mode. Each channel on the analyzer corresponds to an interval of wavelength. Each time the scan controller steps the spectrograph through a wavelength interval, a synchronized channel advance pulse is sent to the MCA by the scan control interface. The output is displayed by the MCA as a plot of intensity (counts) vs. wavelength (channel number). The spectral data is available in analog and digital form for plotting and computer analysis.

Photon pulse counting is a technique used to measure low intensity light. Current pulses, corresponding to events detected by the PMT, are counted over a fixed time period. Each pulse corresponds to a single photon and the total number of pulses is a measure of intensity.

Optimization of the photodetection system for photon pulse counting was accomplished by pulse height analysis of the PMT signal using a controlled light source. The excellent pulse height resolution of the PMT makes it possible to separate pulses corresponding to detected photons from low energy noise. The MCA amplifier gain and discriminator threshold were adjusted so that pulses corresponding to detected photons were counted and much of the low energy tube noise was not.

The equipment used for optimization of the photodetection system is shown in Figure 4.7. The pulse height distribution of the PMT output was measured using a pulsed light source and a coincidence circuit to reduce dark noise. The light source is a gallium phosphide light emitting diode (LED) which has maximum output at 560 nm. The pulse output of a Hewlett Packard Model 222A pulse generator was used to gate the MCA in coincidence with the flash of the LED. According to the MCA specifications, for coincidence operation, the gate pulse must reach its threshold 0.5 μs prior to the peak of the input signal and remain high through the peak time of the input. The synchronization output of pulse generator was used to flash the LED. The synch pulse was delayed by an Ortec model 427A delay amplifier. The delay was adjusted so the peak of the LED pulse occurs 0.5 to 0.75 μs after the gate becomes high. The gate remains high for 2 μs. The duration of the LED pulse is about 0.5 μs. The LED was flashed at 8,000 to 9,000 Hz. Figure 4.8 shows the relative timing of the gate and LED pulses as displayed by the oscilloscope. An Ortec model 472A spectroscopy amplifier was used to vary the intensity of the LED flash.

To determine the proper gain for photon counting, the MCA amplifier gain and the intensity of the LED flash were varied until a photoelectron pulse height distribution similar to that presented in the tube manufacturer's specifications [4.2] was obtained (Figure 4.9). This distribution was obtained with the MCA gain at its minimum value.

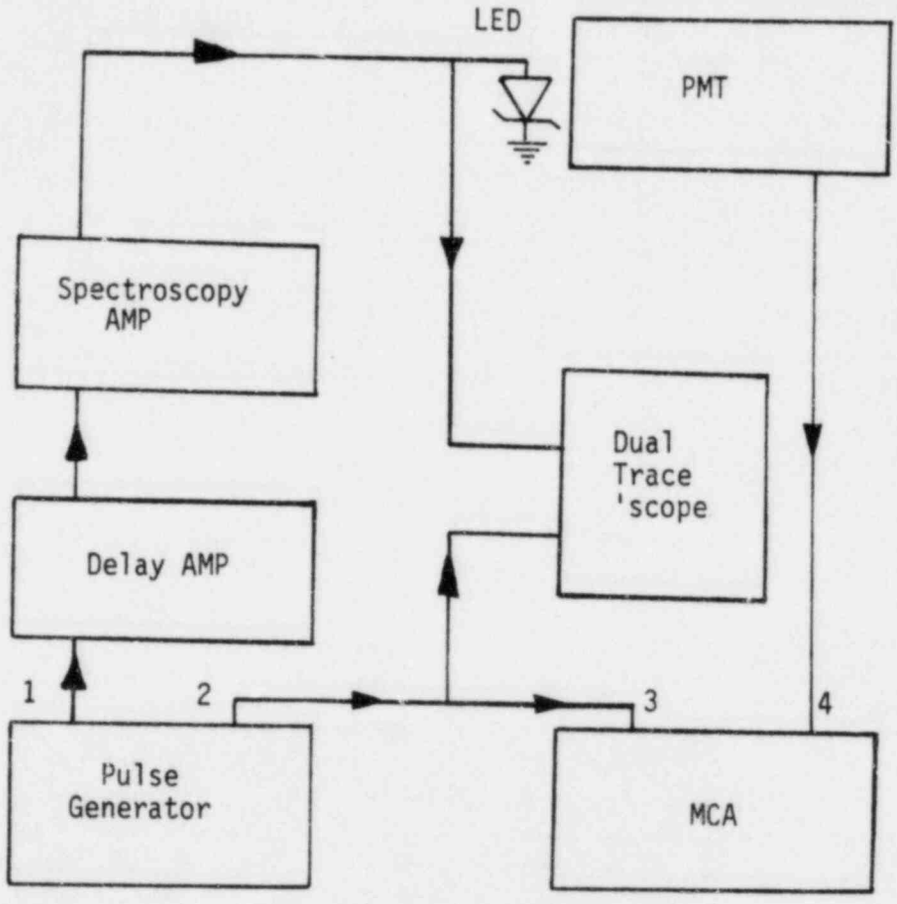

1 Synch output
2 Pulse output
3 Gate input
4 Signal input

Figure 4.7 Equipment for pulse height analysis of PMT output

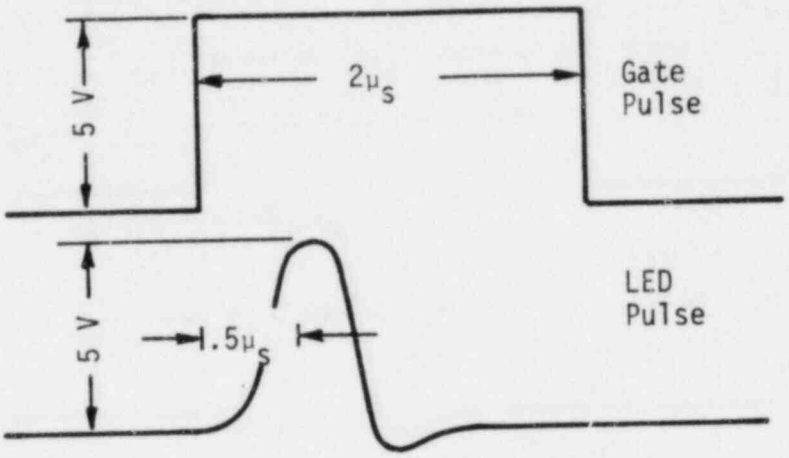

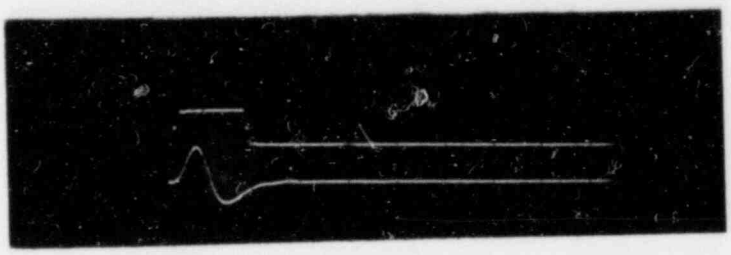

Photo of 'scope trace

Figure 4.8 LED and gate pulse timing

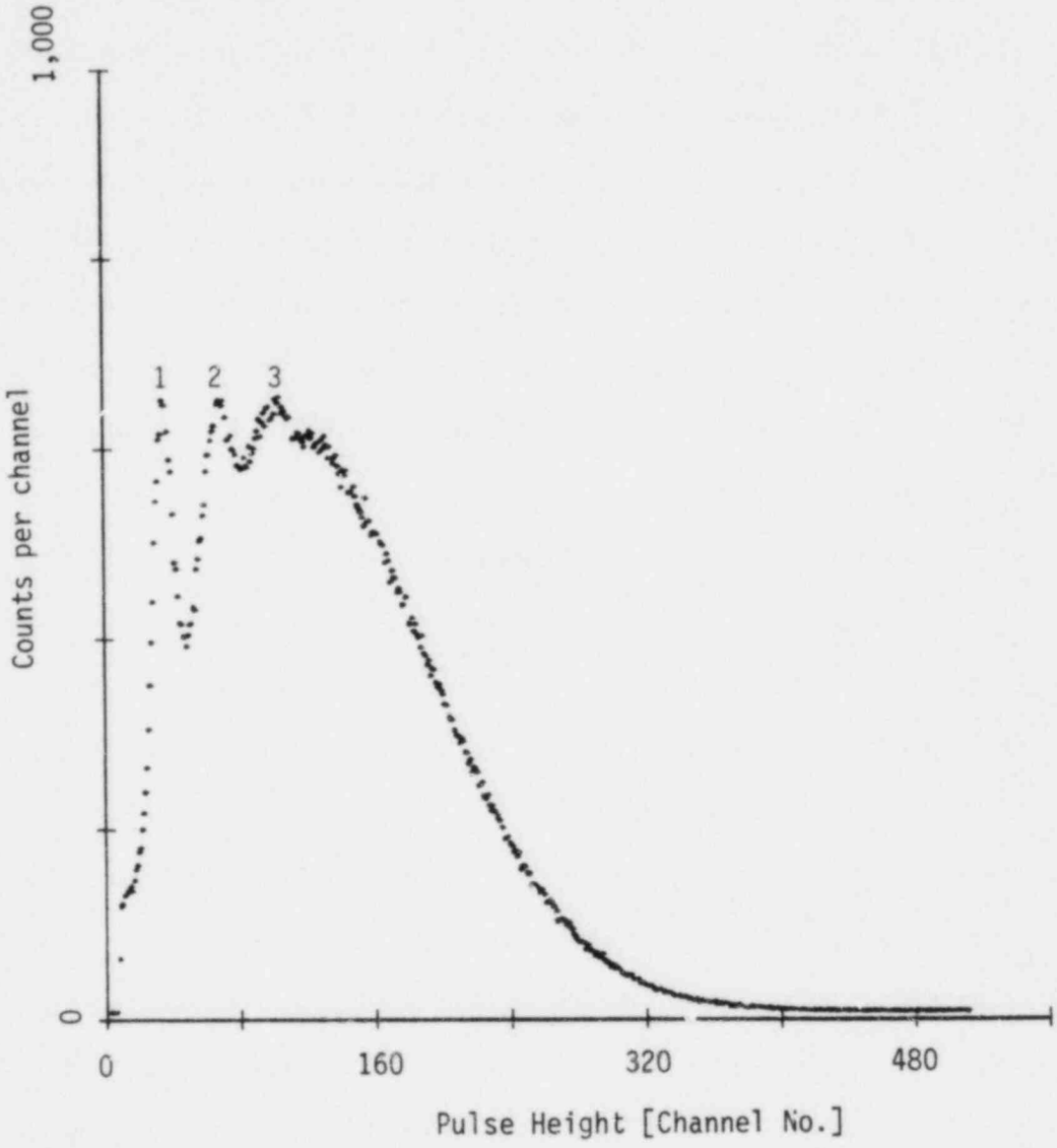

Figure 4.9 Measured photoelectron pulse height distribution

Quantum restrictions on light energy cause the spectrum to break into peaks. The first peak corresponds to the detection of a single photon in the analyzer sampling time. The second peak corresponds to detection of two photons and so on. The characteristics used to identify the photoelectron peaks are described below.

Since the pulse height is proportional to the energy detected by the PMT, the multiple photon peaks should fall in channels which are integral multiples of the first peak. The first, second, and third peaks in Figure 4.9 are in Channels 31, 66, and 93 which are nearly integral multiples. The deviation can be attributed to a slight nonlinearity of the MCA preamplifier.

The peak to valley ratio is the quotient of the maximum counts in the first peak to the minimum counts in the valley between the first and second peaks. The peak to valley ratio is an indication of the pulse height resolution of the tube. It is a characteristic of the PMT and an identifiable feature of the photoelectron pulse height distribution. To measure the peak to valley ratio, the intensity of the LED was varied during acquisition of the pulse height distribution to obtain nearly equal numbers of counts in the first, second, and third photon peaks [4.3]. For the pulse height distribution shown in Figure 4.9, the peak to valley ratio is 1.67. RCA specifies a value between 1.4 and 1.9 for similar conditions.

Calculations based on the sensitivity of the PMT and the gain of the MCA amplifier indicate that the single photon peak should

fall between channels 1 and 24 in Figure 4.9 (see Appendix). Some of the parameters used in this estimate have a large uncertainty. For example, the sensitivity of the PMT is strongly dependent on wavelength and the absolute gain of the amplifier is not well documented. The estimate does show that the order of magnitude of the system gain is correct for photon counting.

The MCA lower level discriminator (LLD) was adjusted to avoid counting low energy noise pulses. The LLD separates photon counts from low energy noise by establishing the energy threshold for pulse counting. The LLD setting reflects a compromise. Setting the discriminator low allows counting of more low energy noise pulses decreasing the signal to noise ratio. Setting the discriminator high inhibits counting of both low energy noise and detected photons, increasing the signal to noise ratio, but decreasing the signal strength.

An empirical approach was used to establish the discriminator level. The pulse height distribution was observed for a range of LLD settings using the equipment shown in Figure 4.7. The MCA was not gated. The intensity of the LED was adjusted so the single photon peak dominates the pulse height distribution as shown in Figure 4.10. The second, third, and higher peaks were eliminated by reducing the intensity of the LED.

In Figure 4.10 there are a significant number of low energy noise pulses in channels 1 to 20. Some of these can be attributed to low energy PMT noise. The background noise level was determined by blocking the light from the LED with an opaque paper shield and

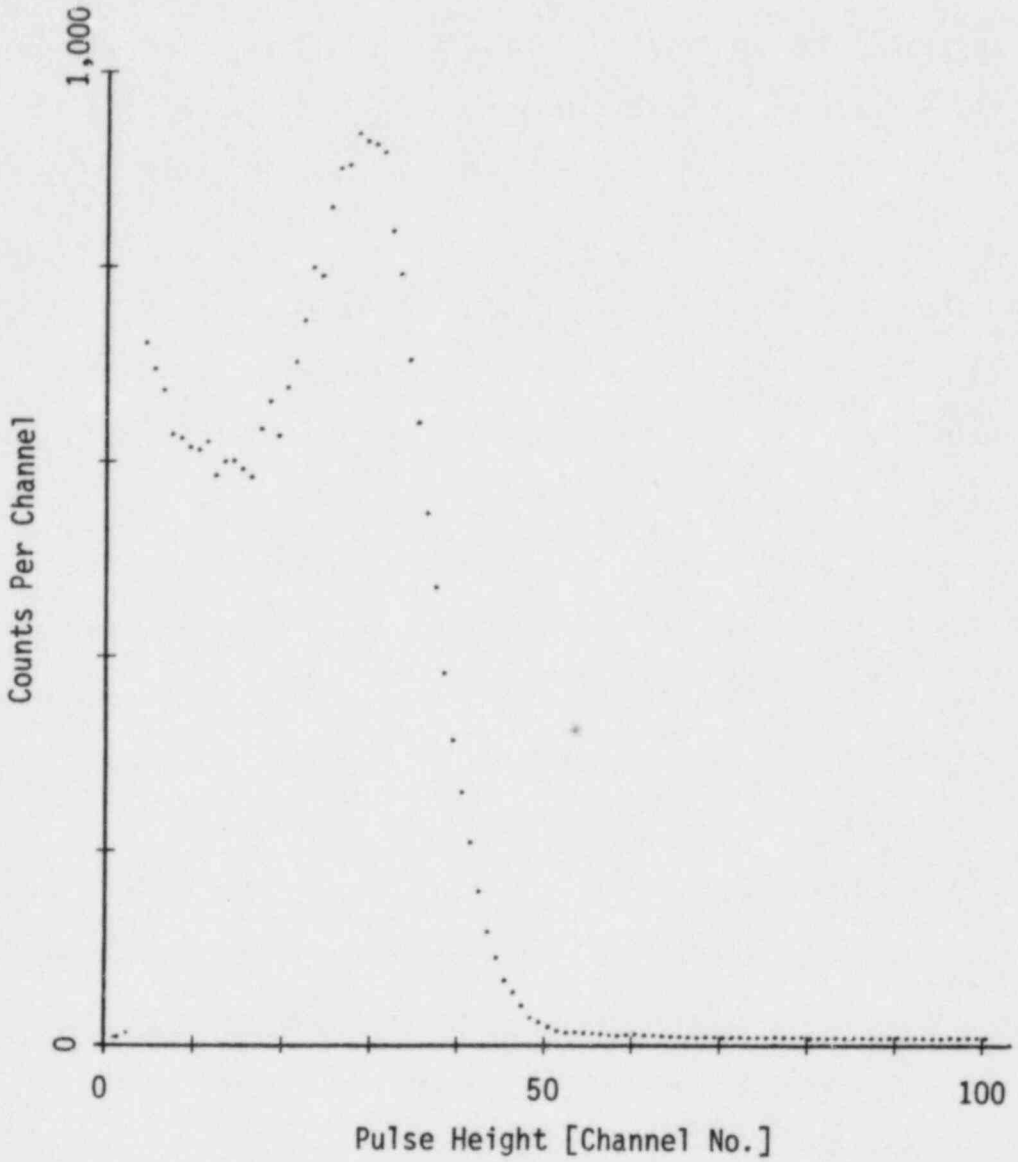

Figure 4.10 Photoelectron pulse height distribution, minimum LLD threshold

repeating the spectrum. The total number of counts in the dark spectrum was subtracted from the total number of counts in the first spectrum to calculate the signal strength and the signal to noise ratio. This process was repeated over a range of LLD settings.

The relative signal strength and signal to noise ratio are plotted in Figure 4.11. The signal strength was normalized by dividing each value by the signal strength for the lowest LLD setting. The LLD setting is characterized by the number of inactive channels. As the threshold is increased, channels receiving low energy signals are deactivated. As expected, the signal strength decreases and the signal to noise ratio increases as the LLD setting is increased. The product of signal to noise ratio and relative signal strength is plotted as a function of discriminator setting in Figure 4.11c. The product does not vary significantly or show strong extrema, thus the LLD setting is probably not critical. The LLD was set at channel 5 which corresponds to approximately 1/6th of the single photon energy level. Figure 4.12 shows the pulse height distribution after adjustment of the LLD. The low energy noise seen previously in the first few channels has been eliminated.

The MCA gain and LLD threshold were set based on pulse height analysis of the PMT output. The energy window defined by these settings is used in the multichannel scaling mode for photon pulse counting. Pulses below the LLD threshold are rejected as noise. Pulses above the threshold are counted.

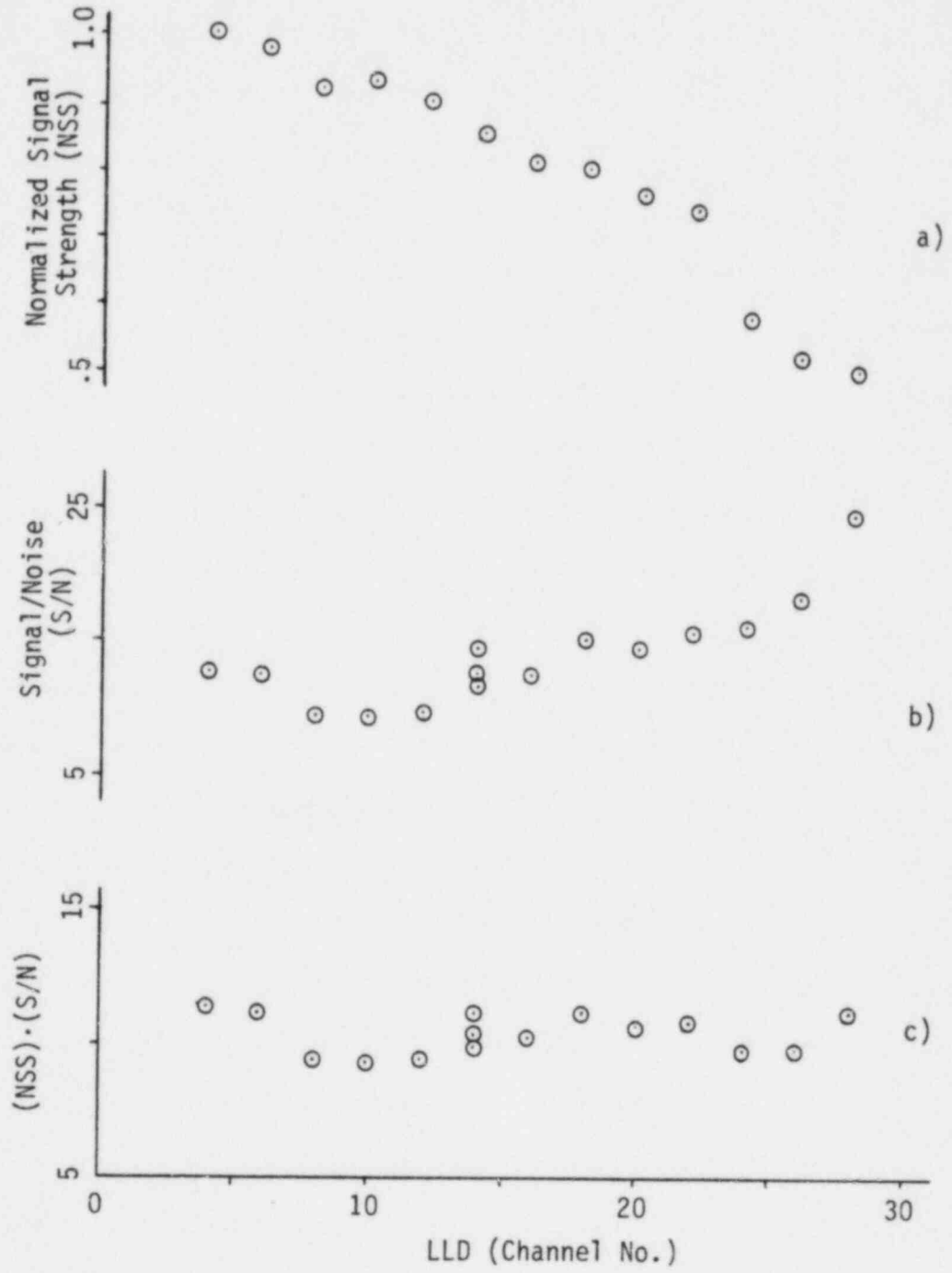

Figure 4.11 LLD optimization data

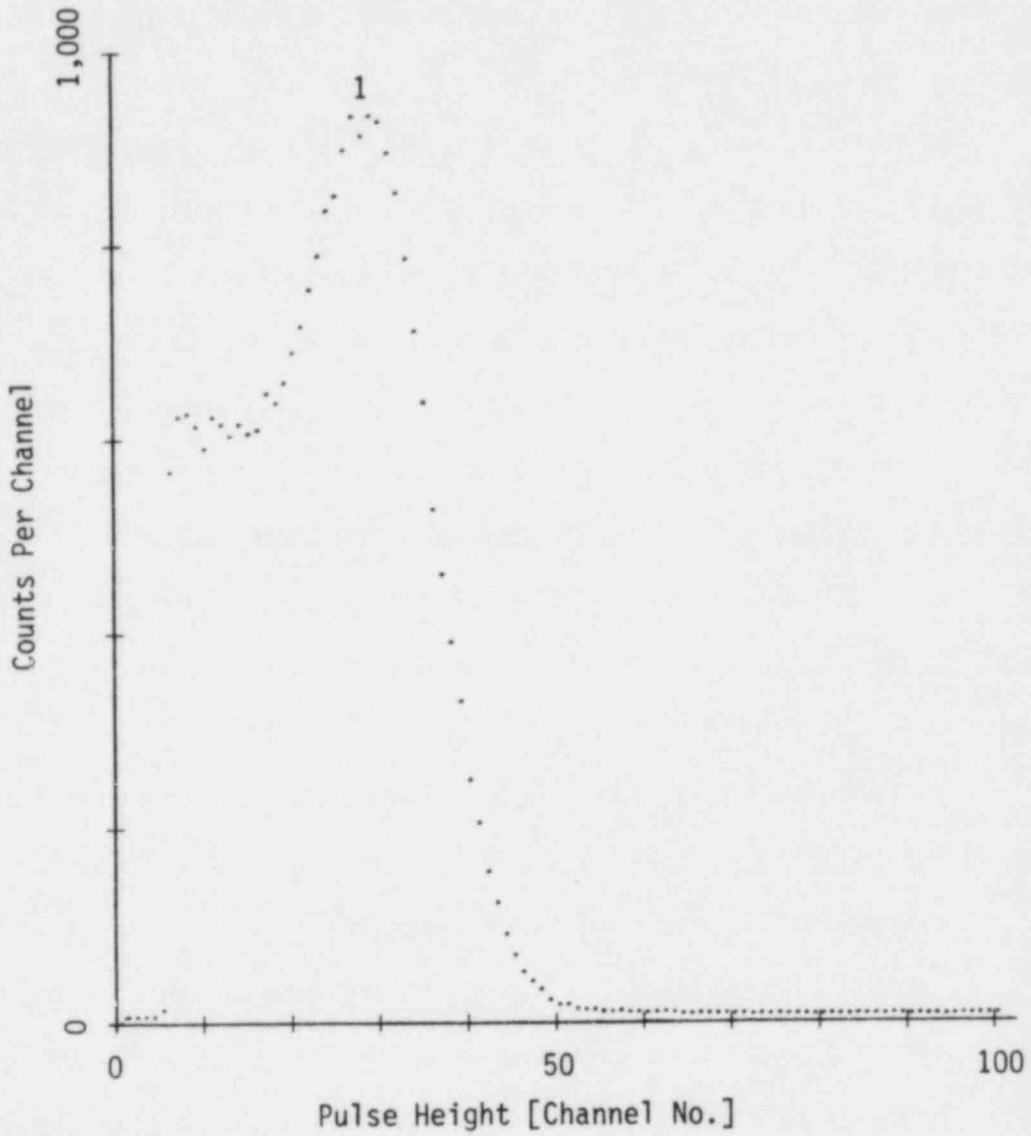

Figure 4.12 Photoelectron pulse height distribution after LLD adjustment

4.5 Final Alignment and System Operation

This section describes the signal optimization procedure used for final optical alignment and some general considerations for acquiring spectral data.

Raman and Rayleigh scattering from liquid water produce intensities which are 10^3 to 10^6 stronger than that of Raman scattering from nitrogen or steam at atmospheric pressure. These relatively strong scattering sources were used to refine the alignment of optical components. The positions of the optical components were adjusted using their traversing mounts to maximize the detected Rayleigh and Raman scattering intensities for liquid water. The optimization process increased the optical efficiency of the system so the weaker intensities, characteristic of Raman scattering from gases, were observable.

Rayleigh scattering from liquid water was observable with the system approximately aligned as described in Sections 4.2 and 4.3. A spectroscopy cell (Precision Cells, type 1P, 45 mm x 10 mm x 10 mm) containing distilled, deionized water was mounted on a temporary sample holder at the measurement point. The laser was adjusted to its minimum output power. The spectrograph was scanned past the Rayleigh wavelength. If no signal was observed, the incident power was increased slightly and the scan repeated. When the sharp Rayleigh peak was observed, the optimization process began.

The spectrograph was set to monitor the wavelength of the Rayleigh peak. The MCA controls were set for multichannel scaling operation. The inhibit advance switch on the scan control interface

was set for manual control over the MCA with time based channel advance. In this mode of operation the system monitors the scattering intensity at one wavelength. In the acquire mode, the MCA displays the detected intensity in real time.

The position of the vertical traverse, on which the laser mirrors were mounted, was adjusted to maximize the detected intensity. The horizontal traverses for the laser focusing lens and collection optics were optimized the same way. Final adjustment required two or three iterations for each traverse because changing the position of one component affects the optimal position of the others.

Precautions against over exposing the PMT were taken when observing the Rayleigh wavelength. Excess light can damage the photocathode. As the optimization procedure increased the detected Rayleigh intensity, the incident laser power was reduced using polarization or neutral density filters to protect the PMT.

Optimization on the Rayleigh wavelength was not used for final optical alignment since Rayleigh scattering from the liquid is indistinguishable from stray laser light scattered from lenses, mirrors and sample cell surfaces. Final optimization was based on observations of Raman scattering from liquid water. The scan controller was set to sweep the 3400 cm^{-1} Raman band for water. The laser power was adjusted to 90 percent of its maximum output. Scanning the band at this stage in the optimization process generally gave a detectable Raman signal. If the signal was weak, the spectrum was compared to a background spectrum for an empty cell to highlight the Raman signal. If no

Raman signal was observed, the Rayleigh line optimization was repeated. When a Raman signal was observed, the system was again set up for signal optimization. The spectograph was set to monitor the Raman band peak. The scan control interface and the MCA were set to display the signal strength in real time. The mirror and lens positions were iteratively adjusted to maximize the detected intensity.

After optimizing the optics, the liquid cell was removed and Raman scattering from atmospheric nitrogen or steam was observed. Acquisition of spectral data required selecting scan parameters such as upper and lower wavelength limits, scan speed and the number of cycles. Initially, the wavelength limits were selected based on information in the literature. After preliminary Raman observations the scan parameters were modified to improve accuracy. Table 4.1 lists the Raman band origins and the spectral range of the bands for liquid water, nitrogen and steam [4.4, 4,5, 4.6].

Table 4.1 Raman Shifts

Sample	Stokes Vibrational Band Origin		Spectral Range	
	$\omega[cm^{-1}]$	$\lambda^1[nm]$	$\omega[cm^{-1}]$	$\lambda^1[nm]$
Liquid water, room temperature	-3400	585	-2900 to -3750	568.0 to 597.0
Atmospheric N_2, room temperature	-2323	550.4	-2303 to -2336	549.8 to 550.8
Steam, atmospheric pressure, 20 to 200 K vapor superheat	-3657	594.0	-3627 to -3662	592.0 to 594.2

[1] Wavelengths based on 488.0 nm incident laser

5. EXPERIMENTAL PROGRAM

5.1 Overview

The experimental program was begun with relatively simple Raman experiments using liquid water and atmospheric nitrogen as samples. The preliminary experiments were used to refine the Raman system and operating procedures. The system was then used for more difficult experiments in which the temperature sensitivity of Raman band shapes was investigated for superheated steam in single and nonequilibrium two-phase flows. The experiments, along with their specific objectives, are listed below.

1. *Raman scattering from liquid water*

   Objectives:

   a. Verify that the equipment is working properly

   b. Gain experience in system operation under favorable intensity conditions

   c. Obtain sample spectra for development of data handling and documentation procedures

2. *Raman scattering from atmospheric nitrogen*

   Objectives:

   a. Show that the optical sensitivity is sufficient for detection of Raman scattering from a gas sample

   b. Obtain sample spectra for development of data analysis procedures

   c. Refine procedures for further experiments

   d. Document reproducibility of Raman band shapes

3. *Raman scattering from superheated steam*

Objectives:

a. Observe temperature effects on Raman vibrational contours of steam

b. Estimate the sensitivity of temperature measurements based on Raman scattering for single-phase steam

4. *Raman scattering from the liquid and gas phases of an air/water mist flow*

Objectives:

a. Show that Raman scattering from a gas is detectable in the presence of Mie scattering caused by liquid droplets in the sample

b. Determine the extent of interference in the spectral region of interest for water vapor, due to Raman scattering from liquid water droplets

5. *Raman scattering from steam in nonequilibrium superheat, dispersed two-phase flow*

Objectives:

a. Show that temperature effects on the Raman band shape for steam are measurable in the presence of dispersed water droplets

b. Estimate the sensitivity of proposed temperature measurements based on Raman scattering for nonequilibrium superheat, dispersed flow

These experiments are discussed in the sections which follow. Procedures for data analysis are described and results are presented.

5.2 Raman Scattering From Liquid Water

The first experiments conducted in this investigation involved analysis of Raman scattering from liquid water. Raman scattering intensities are proportional to the number density of scattering molecules. Liquid water is approximately 1,000 times more dense than steam under the conditions of interest here. The relatively strong scattering intensity from liquid water provided a signal which was used to test the equipment and experimental procedures. These experiments were valuable for gaining experience in system operation under favorable intensity conditions.

A disposable plastic spectroscopy cell containing distilled deionized water was mounted at the focal point of the Raman system. A 10 mm slit was used at S_2 in the premonochromator for a 40 nm bandpass. The bandpass was centered at 585 nm, which is approximately the midpoint of the 3400 cm^{-1} Raman band. The spectrograph was scanned over 48 nm spectral region from 557.5 to 605.5 nm. The scan rate was 5 nm/minute with the intensity recorded in .05 nm increments resulting in a dwell time of 0.6 s/channel. Figure 5.1 shows the data for a single scan. The band shape agrees qualitatively with data published previously by Walrafen [5.1] and Pan, et al. [5.2].

This data was used in development of handling and documentation procedures. Raman spectra were written from the multichannel analyzer memory onto digital data cassettes. The cassettes were read onto a disk file on the University central computer (CYBER 720). Each spectrum was assigned an identification number. The data, type and temperature of the sample, upper and lower wavelength limits, scan

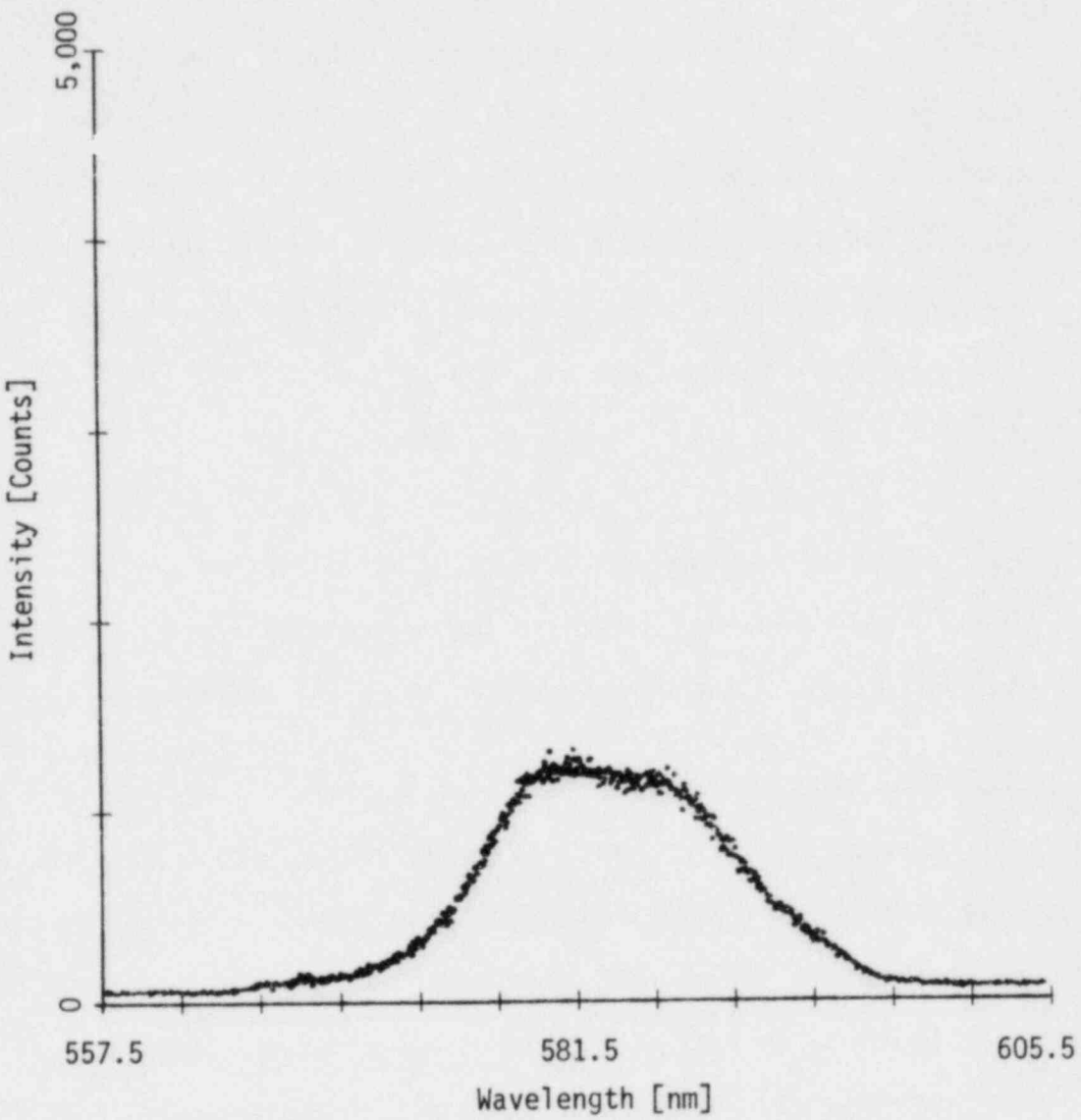

Figure 5.1 3400 cm^{-1} Raman band for liquid water at room temperature (raw data)

rate and number of repetitive cycles were added to the file for use in documentation and analysis programs. Data was kept on the disk file for analysis after which it could be punched on cards for inactive storage. A FORTRAN program entitled RAMDOC was written to document spectral data. Given a spectrum identification number, RAMDOC searches through the file to find the desired data then produces a listing and plot of the raw data. The listing is preceeded by a heading which details the conditions of the experiment. The Appendix of this report contains a sample output listing. Figure 5.1 is typical of the plots produced by RAMDOC.

Raman signals from liquid water were used to optimize the alignment of optics as described in Section 4.5. Preliminary experiments using liquid water as the scattering medium also provided experience in system operation under favorable intensity conditions.

5.3 Raman Scattering From Atmospheric Nitrogen

Nitrogen in the ambient atmosphere can be used to produce reference spectra for testing and comparison of Raman systems. Stokes vibrational scattering from atmospheric N_2 is of approximately the same intensity as from superheated steam under the conditions of present interest. Atmospheric N_2 is not effected by many of the problems (condensation, temperature control, etc.) associated with steam. For these reasons, ambient air was used as the scattering medium in preliminary Raman experiments. Raw data for an early N_2 spectrum is shown in Figure 5.2. This spectrum was recorded using a 2 mm slit at S_2 in the premonochromator. The bandpass covers 8 nm

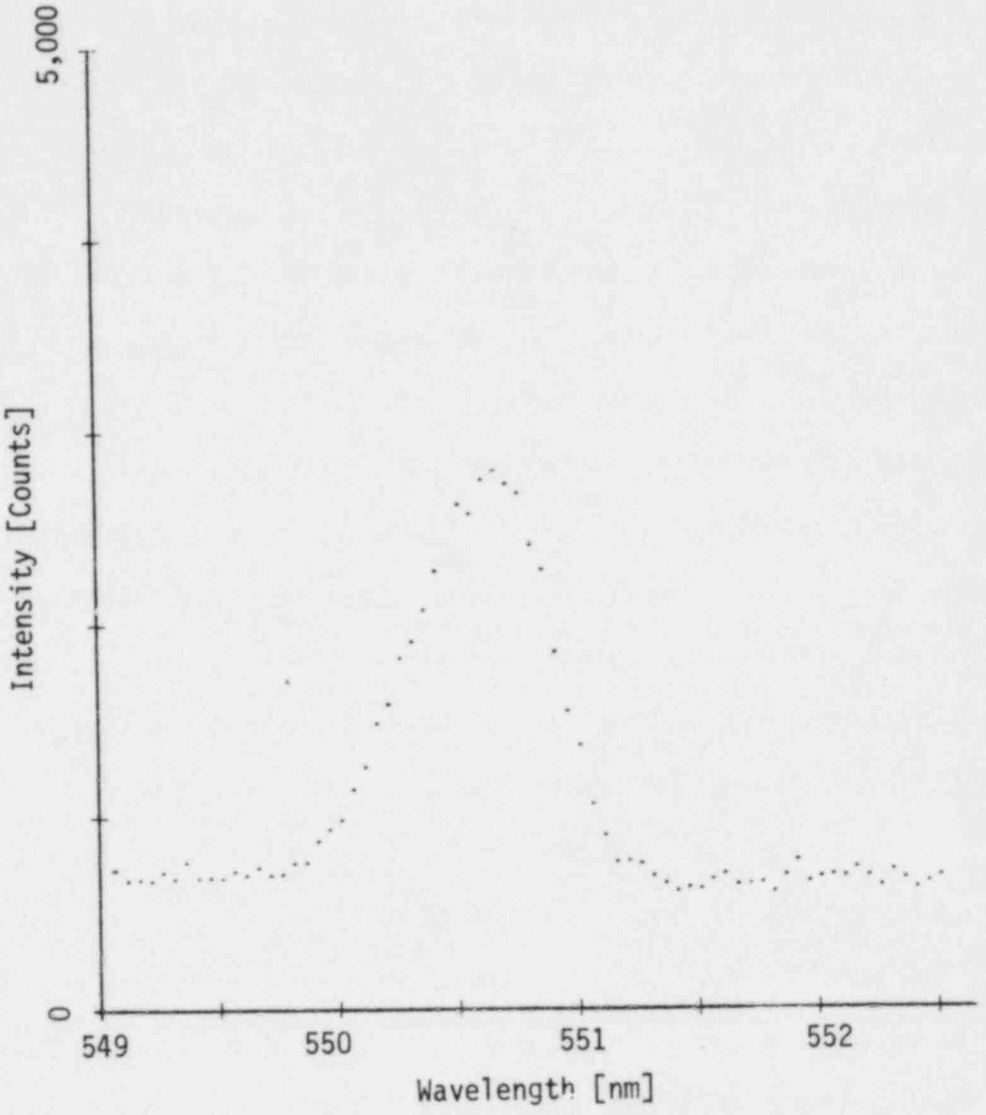

Figure 5.2 Raman spectrum of atmospheric nitrogen at room temperature (raw data)

and was centered at 551 nm, near the midpoint of the 2,323 cm^{-1} vibrational branch for N_2. The spectrograph scanned a 3.5 nm region from 549 to 552.5 nm. The scan rate was 5 nm/minute. The spectrum shown in Figure 5.2 is the sum of 50 repetitive scans for a total dwell time of 30 s/channel. This data agrees qualitatively with previously published nitrogen spectra [5.3, 5.4]. At low temperature (300 K), the 0 to 1 vibrational transition dominates the Stokes band, which appears as a discrete line. The observed bandshape thus corresponds closely to the monochromator slit function.

This data demonstrates the optical sensitivity of the Raman system. The Raman signal in the entire Stokes vibrational branch is approximately 1,000 counts/s. Previous researchers have reported equivalent sensitivities using similar equipment [5.5].

Raman data for atmospheric nitrogen was used to develop data analysis techniques. The objective of the analysis described below is to remove unwanted background noise from the Raman spectrum to allow direct comparison of Raman band shapes.

The baseline level of the data shown in Figure 5.2 is nonzero. The baseline level is associated with background noise. In analysis of Raman signals, it is necessary to note the difference between the constant background offset and random noise [5.6]. The main contributors to background offset and random noise are stray light and photomultiplier dark current.

The observed signals can be divided into three elements.

1. Raman signal

2. Random background noise

3. Constant background offset

These are illustrated in Figure 5.3. Adding the three elements gives a spectrum similar to Figure 5.2. The approach used here, for analysis of Raman data, minimized the effect of the random component then subtracted off the offset, leaving the Raman signal.

The noise component varies randomly about zero in time. Theoretically, an infinite time average would yield a net contribution of zero at all wavelengths. Realistically, averaging signals over a long time period reduces the random component to a small fraction of the total signal. The net contribution due to random noise varies inversely as the square root of the averaging time. Acquisition of the data shown in Figure 5.2 required approximately 45 minutes. To further reduce the random noise by a factor of two, using time averaging, would require three hours of data acquisition.

Averaging in wavelength has been used by previous researchers to reduce the effect of random noise on the Raman band shape [5.7]. In developing a wavelength averaging procedure, the effect on the band shape was considered since the band shape is the characteristic to be used for temperature measurements. Excessive wavelength averaging could reduce temperature sensitivity. The spectral discrimination system used for this investigation can resolve spectral features on the order of 0.6 nm. Averaging over a wavelength interval which is small compared to 0.6 nm has a minimal effect on measured band shapes. A 0.6 nm interval contains 12 data points, thus equally

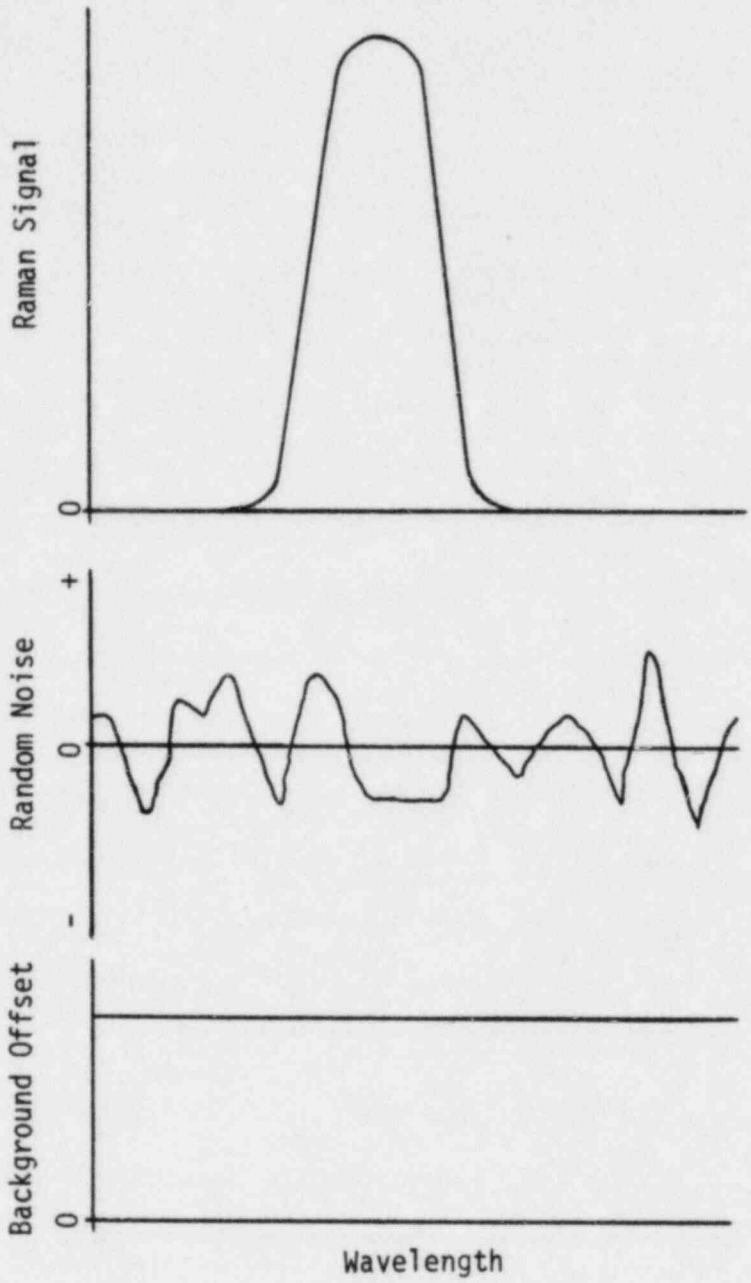

Figure 5.3 Analysis of Raman signals

weighted three point averaging was used as in equation (5.1).

$$\bar{I}_i = (I_{i-1} + I_i + I_{i+1})/3 \qquad i = 2,3,\ldots n-1 \tag{5.1}$$

I represents the intensity or number of counts in each channel. The subscript i refers to the channel number and the overbar denotes the averaged quantity. The first (i=1) and the last (i=n) data points of each spectrum are lost in this calculation.

The effect of three point data averaging is illustrated in Figures 5.4 and 5.5. Figure 5.4 shows two untreated Raman spectra for atmospheric nitrogen obtained under the same conditions as the data of Figure 5.2. The ragged appearance of the contours is due to the effect of random background noise. The smoothed data is shown in Figure 5.5. Wavelength averaging reduces the effect of the random noise without significantly affecting the band shape.

The smoothed Raman band shapes shown in Figure 5.5 should be identical as they were observed under the same conditions. Direct comparison of the smoothed spectral band shapes is difficult because the spectra appear to be of different intensities. Variation of system sensitivity causes changes in the absolute intensity of both the Raman and the background signals. Baseline restoration and normalization were used to compensate for these variations. Temperature measurements require analysis of spectral band shapes. The spectra may be normalized because it is the shape of the contour, not the absolute intensity that contains temperature information.

The baseline was restored to zero by subtracting off the constant

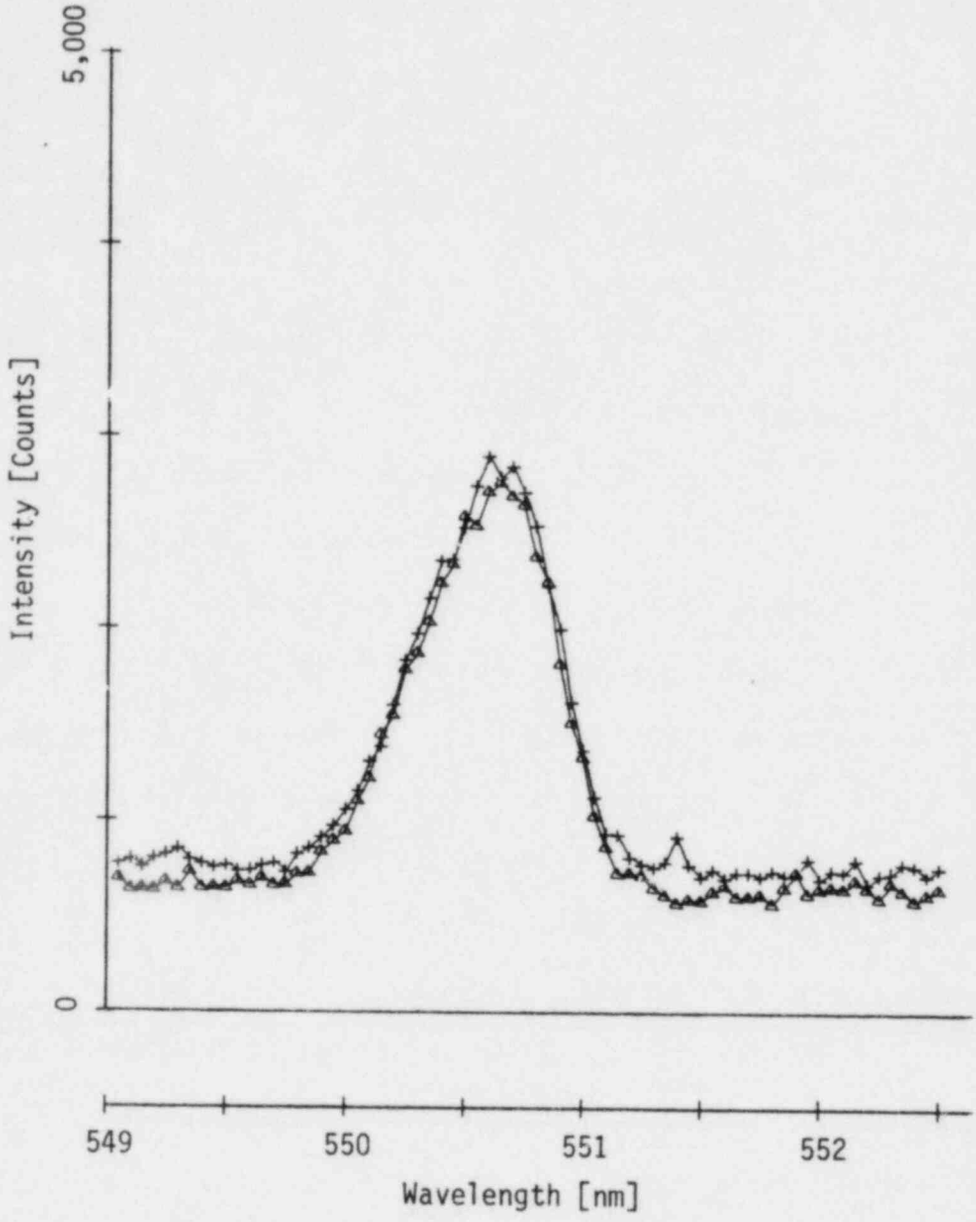

Figure 5.4 Two Raman spectra, atmospheric nitrogen at room temperature (raw data)

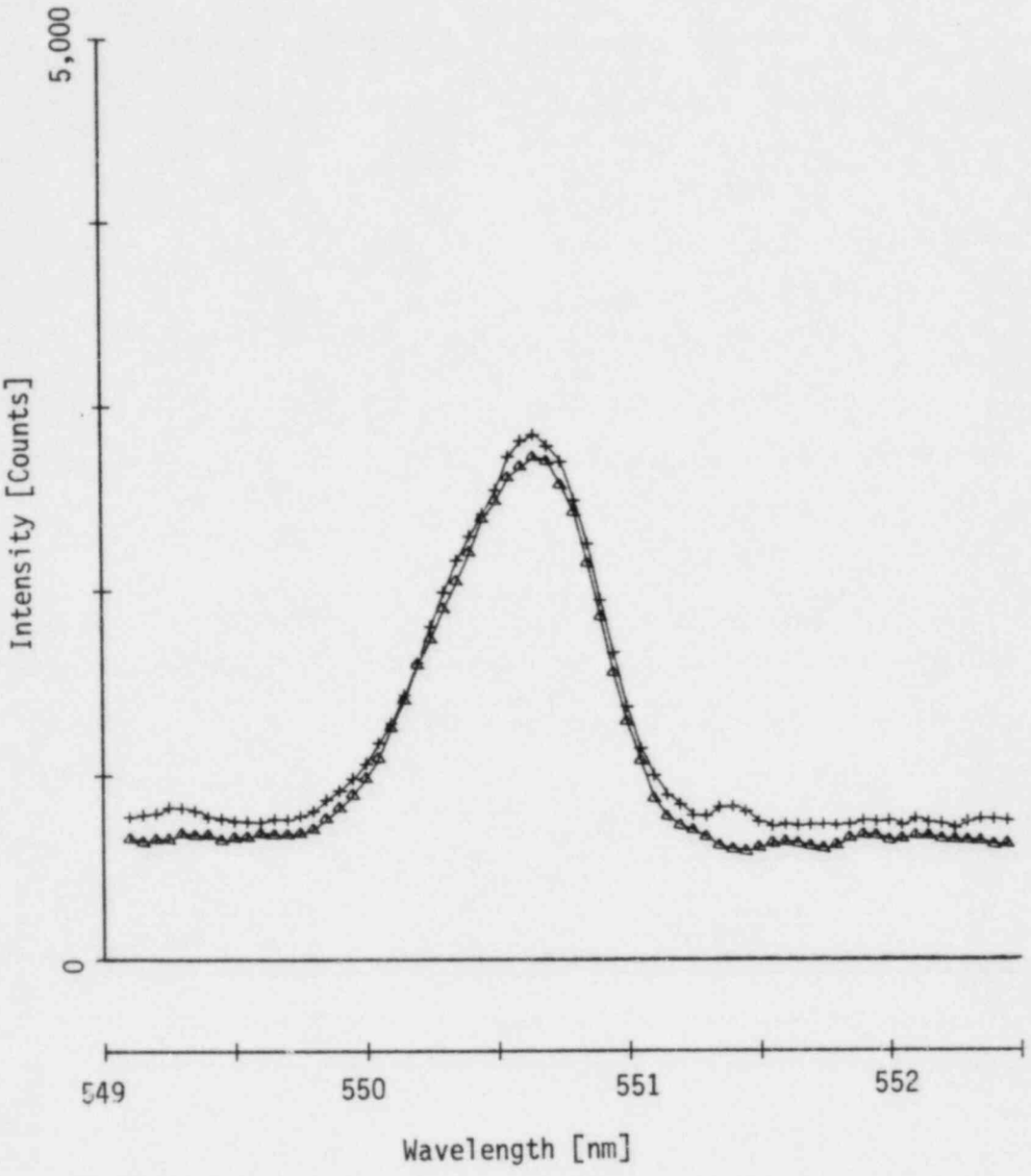

Figure 5.5 Two smoothed Raman spectra, atmospheric nitrogen at room temperature

background offset. The contours were then normalized by integrating the baseline restored Raman signal. The offset intensity, I_o, was estimated using the average of ten data points at each end of the smoothed spectrum.

$$I_o = \left[\sum_{i=2}^{11} \bar{I}_i + \sum_{i=n-10}^{n-1} \bar{I}_i \right] /20 \qquad (5.2)$$

The baseline restored intensity, $\bar{I}_{BR,i}$, was calculated by subtracting the offset from each channel.

$$\bar{I}_{BR,i} = \bar{I}_i - I_o \quad i=2,3,\ldots n-1 \qquad (5.3)$$

The remaining Raman signal was integrated by summing the total number of counts for the baseline restored data.

$$\int_{\lambda_1}^{\lambda_2} I(\lambda) d\lambda \, /(\lambda_2-\lambda_1) = \sum_{i=2}^{n-1} \bar{I}_{BR,i} \qquad (5.4)$$

A spectrum normalization factor, SNF, was calculated which, when multiplied by the baseline restored data, normalized the total Raman signal to an arbitrary 10,000 counts.

$$SNF = 10,000/\sum_{i=2}^{n-1} \bar{I}_{BR,i} \qquad (5.5)$$

The normalized intensity, $\bar{I}_{N,i}$, was calculated by multiplying the baseline restored data by the spectrum normalization factor.

$$\bar{I}_{N,i} = \bar{I}_{BR,i} \cdot SNF \quad i=2,3,\ldots n-1 \qquad (5.6)$$

The effect of these manipulations on the data of Figure 5.4 is illustrated in Figure 5.6. Normalization allows direct comparison of Raman band shapes.

Qualitatively, the normalized band shapes, shown in Figure 5.6, match each other well. Further comparison of the normalized band shapes is made by calculating a mean bandshape, $\bar{I}_{M,i}$, for the two runs and the deviation, $D_{i,j}$, of each run from the mean.

$$\bar{I}_{M,i} = \left[\sum_{j=1}^{NSP} I_{N,i,j}\right] /NSP \quad i=2,3,...n-1 \tag{5.7}$$

The subscript j indicates that the summation is over a number of spectra, NSP.

$$D_{i,j} = \bar{I}_{N,i,j} - \bar{I}_{M,i,j} \quad i=2,3,...n-1, j=1,2,...NSP \tag{5.8}$$

The resulting difference spectra are shown in Figure 5.7. The difference between the normalized band shapes is small and varies randomly about zero. The maximum deviation from the mean spectrum is 3 percent of the mean peak intensity. The scatter in the normalized spectra is given here in terms of σ, the root mean square (RMS) deviation from the mean band shape. For the spectra of Figure 5.6, σ is 1.5 percent of the mean peak intensity.

These calculations have been incorporated into the FORTRAN program, RAMCOM. Given the number of spectra to be analyzed (up to eight) and the appropriate spectrum identification numbers, the program is set up to read the desired data from the spectral data file and perform the analysis automatically. The output consists of a set of plots similar to Figures 5.4 through 5.7 and a data listing.

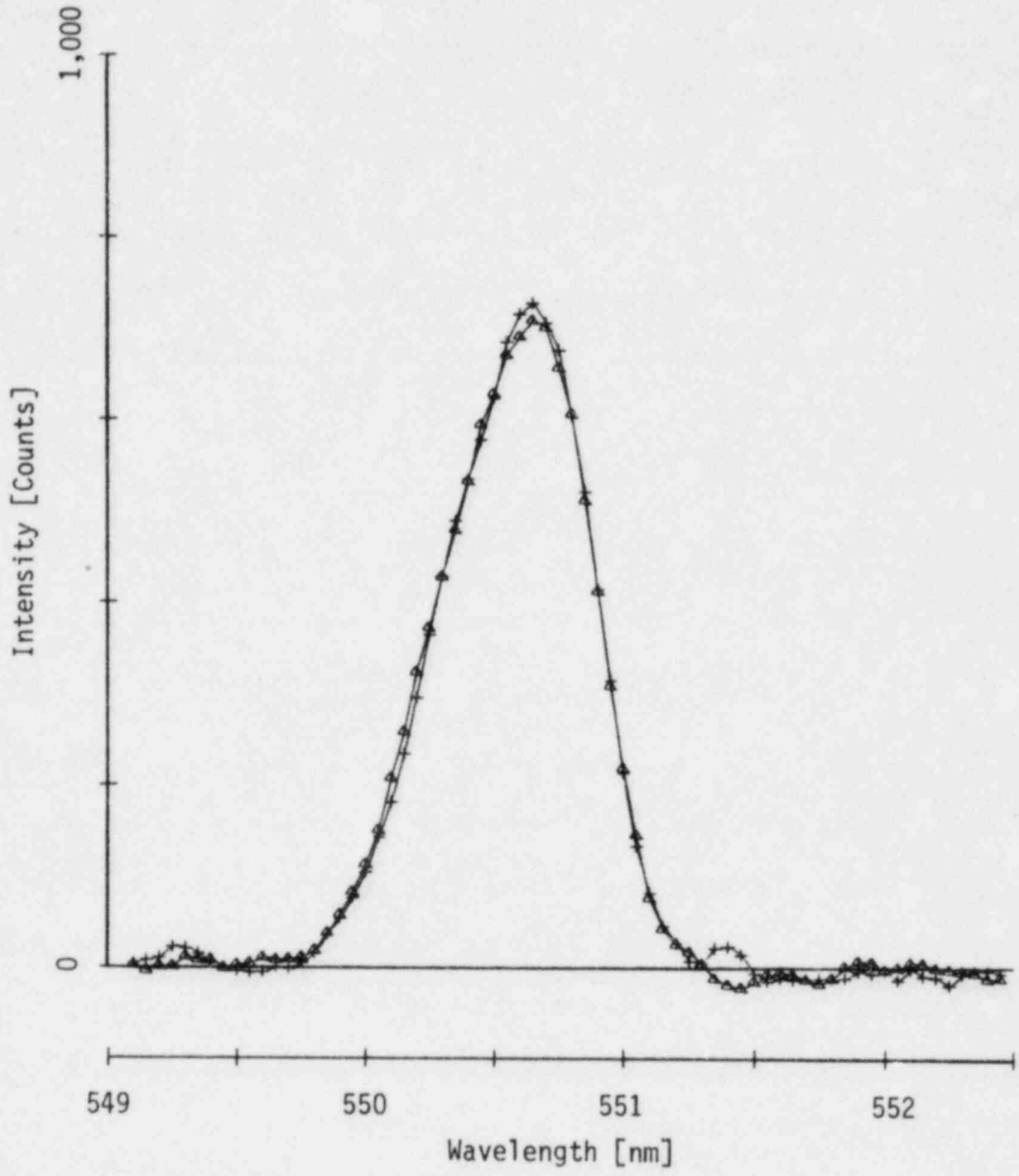

Figure 5.6 Two normalized Raman spectra, atmospheric nitrogen at room temperature

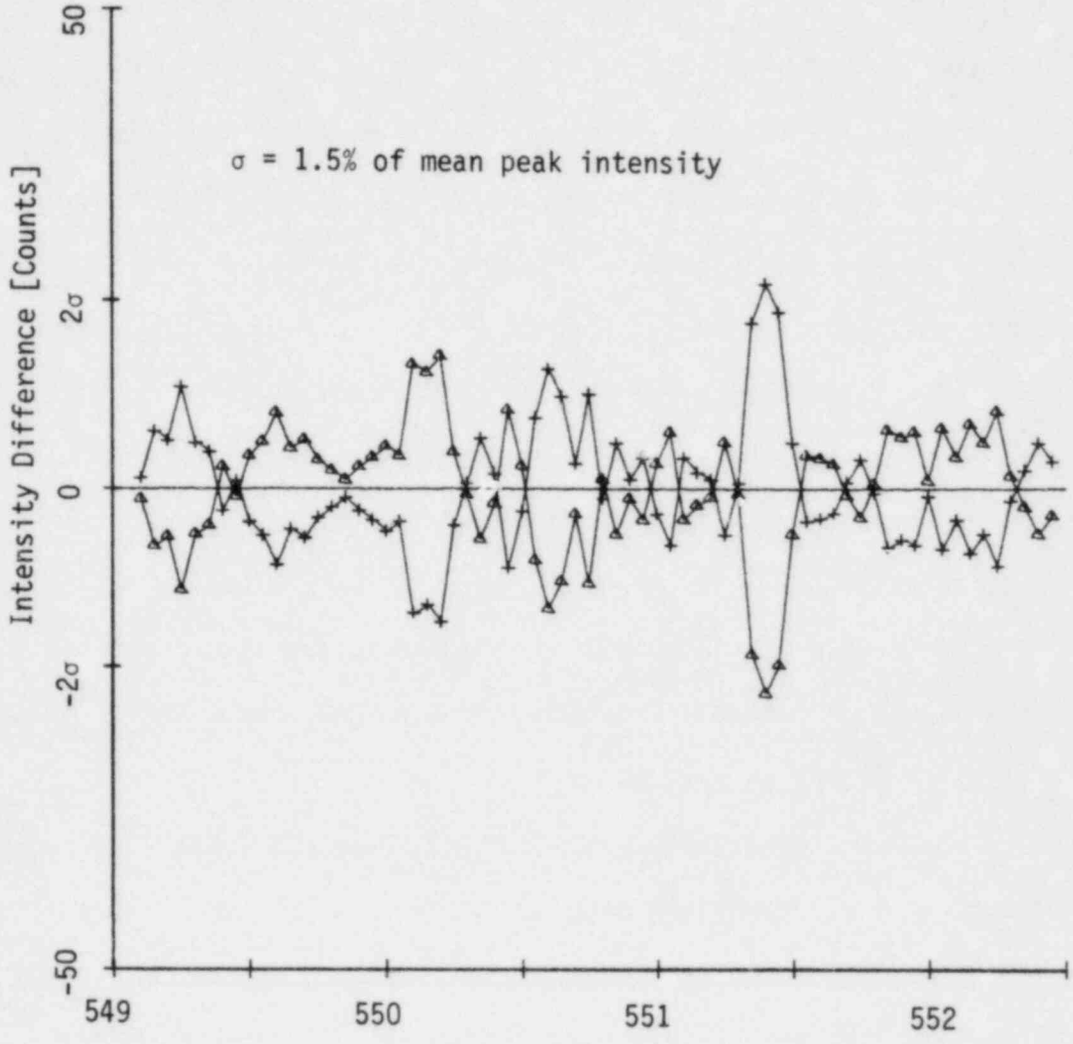

Figure 5.7 Difference between two atmospheric nitrogen spectra

A sample listing is given in the Appendix of this report.

Differences between band shapes recorded under identical conditions result from experimental uncertainty. In developing procedures for further experiments, the objective was to minimize this uncertainty.

Early observations of Raman spectra showed that changes in the premonochromator wavelength setting,or adjustment of the illumination or collection optics,added a systematic error to observed spectral contours. Unfortunately, the system required daily adjustment as described in Section 4.5. The signal optimization procedure required both, changes in the premonochromator wavelength and adjustment of optical components. To avoid introducing systematic errors, the premonochromator wavelength setting and the positions of optical components were not adjusted during the experiments. Experiments were limited to one day and comparisons of band shapes were limited to data acquired on the same day.

Further studies of Raman scattering from atmospheric nitrogen showed that extending the scan limits and increasing the data acquisition time lead to a reduction of experimental uncertainty. Figure 5.8 shows four normalized Raman spectra for atmospheric nitrogen at room temperature. The premonochromator bandpass was 8 nm, the same as for the N_2 spectra presented earlier. The spectrograph scan was extended from 3.5 to 5.0 nm. The upper and lower wavelength limits were 548 and 553 nm. Extending the scan limits provided for a better estimate of the background offset. The scan rate was 5 nm/minute as before but the number of cycles was increased from 50 to

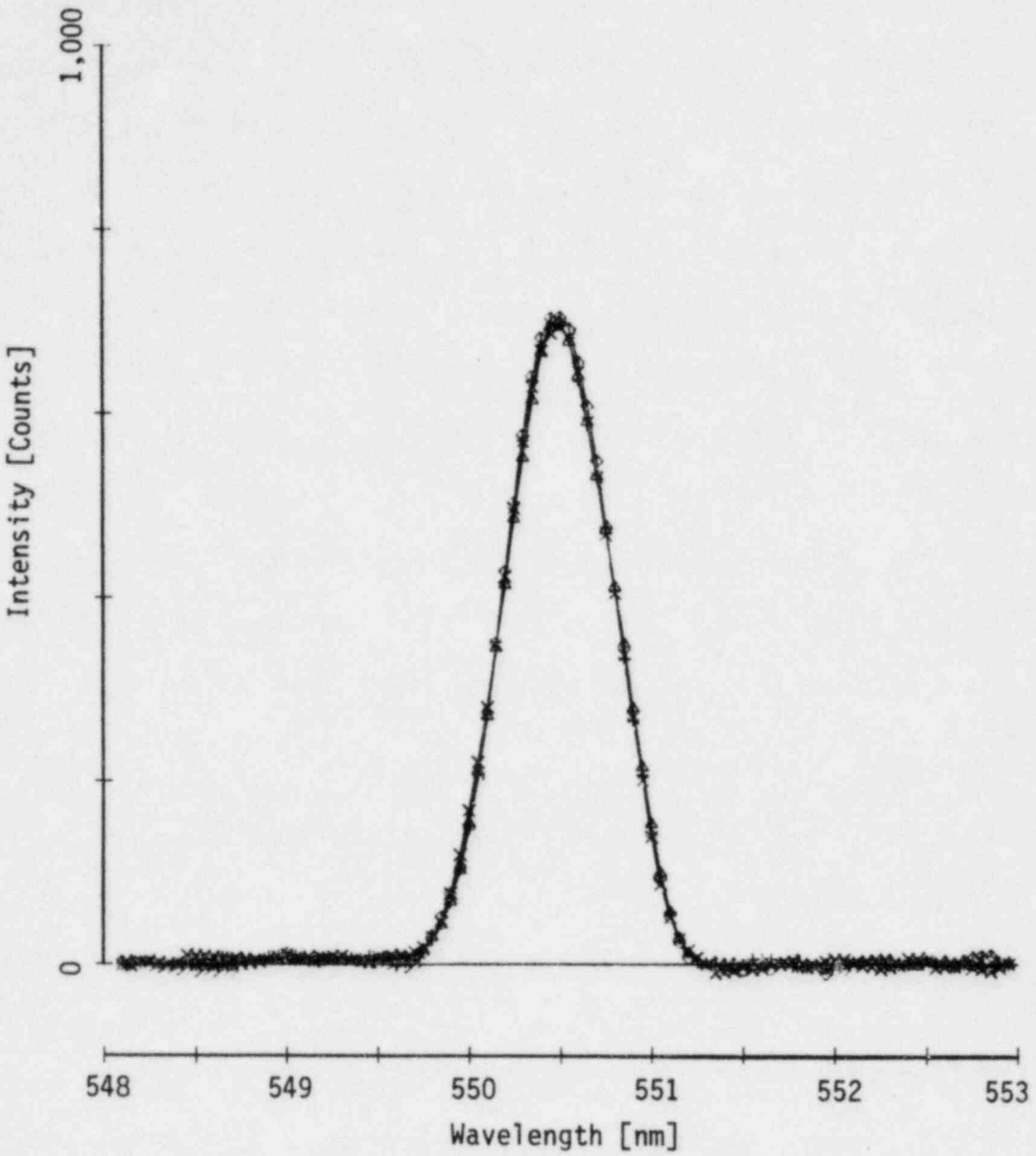

Figure 5.8 Four normalized Raman spectra, atmospheric nitorgen at room temperature

75 for a total dwell time of 45 s/channel. The increased dwell time further reduced the effect of the random noise. Difference spectra for these band shapes are given in Figure 5.9. The RMS deviation from the mean of the four runs is 0.7 percent of the mean peak intensity. These spectra illustrate the reproducibility of Raman band shapes observed with the system developed for this research.

Raman scattering from atmospheric nitrogen was used to demonstrate the optical sensitivity of the system. Data obtained through these observations was used to develop a data analysis procedure. Additional observations led to improved experimental procedures which were applicable to further experiments. The uncertainty of normalized band shapes observed for nitrogen was shown to be small.

5.4 Raman Spectra of Single-Phase Steam

The procedures and data reduction techniques developed in the previous experiments were used to observe the effect of temperature on Raman spectra of superheated steam. Two experiments were conducted. In the first, a series of Stokes vibrational spectra were recorded from a superheated steam sample at a constant temperature. Analysis of this data showed the degree of experimental uncertainty in the normalized band shapes for steam. In the second experiment, Raman scattering from superheated steam was observed over a range of temperatures. These observations were used to estimate the temperature sensitivity of the band shapes. Intensity ratios, calculated from the normalized band shapes, were used to estimate the temperature sensitivity quantitatively.

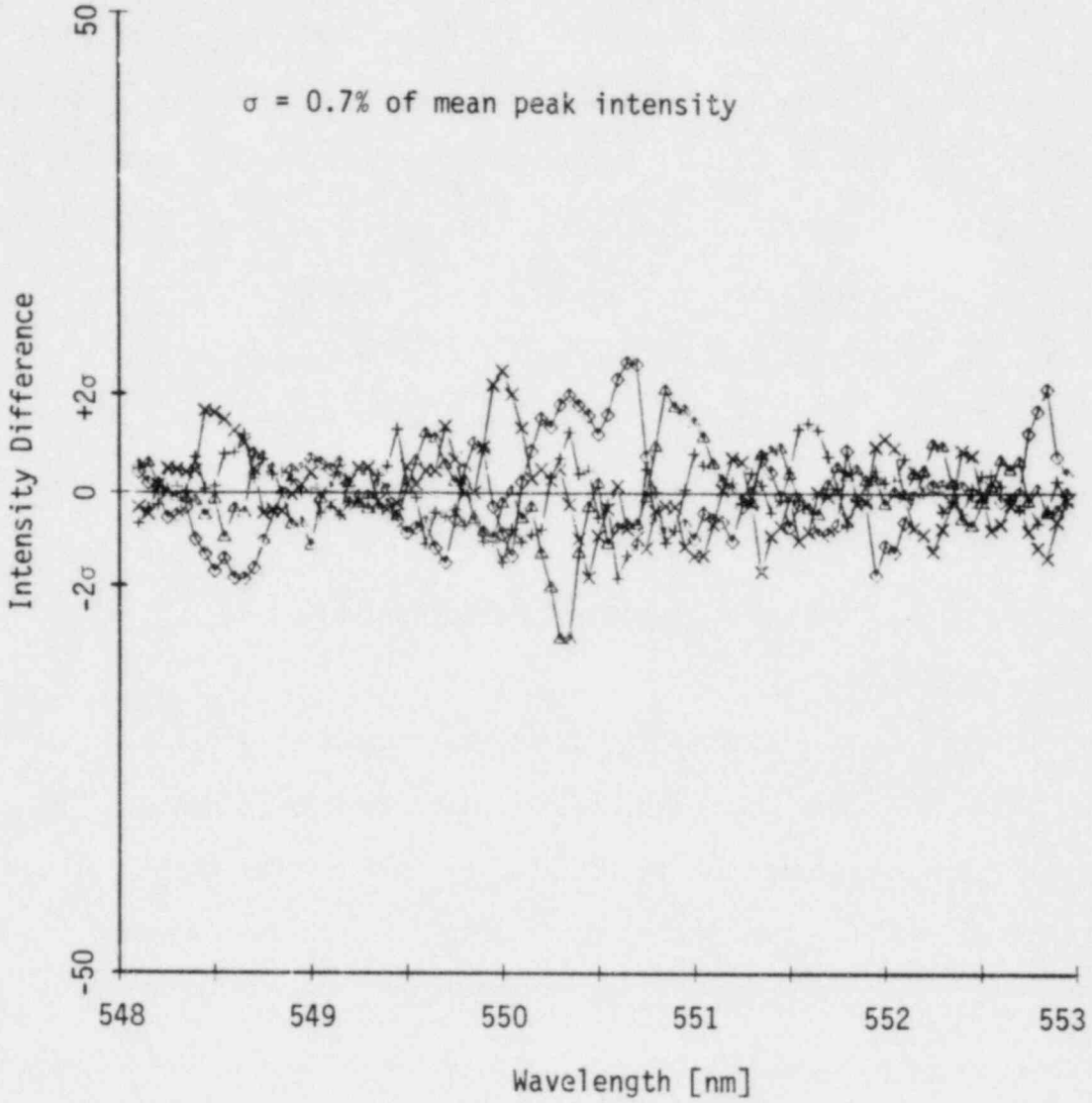

Figure 5.9 Four difference spectra, atmospheric nitrogen at room temperature

The steam generator, described in Chapter 3, produced a steady jet of steam at atmospheric pressure with a vapor superheat ($T-T_{SAT}$, T_{SAT}=373K) of 20 to 200 K. During the Raman experiments, the vapor superheat at the nozzle inlet was monitored and held constant within ±5 K. The average nozzle inlet temperature for each run was used to estimate the temperature in the measurement volume from Figure 3.15.

Prior to the steam experiments, the optics were aligned using the signal optimization procedure of Section 4.5. The positions of optical components and the premonochromator wavelength were not adjusted during the experiment to minimize uncertainty. The laser beam passed through the steam jet about 10 mm downstream of the nozzle outlet probing a sample volume approximately 10 mm long and 1 mm in diameter.

Raman scattering from the steam was observed using a 2 mm slit at S_2 in the premonochromator resulting in an 8 nm bandpass. The bandpass was centered at 594 nm, near the midpoint of the 3,650 cm^{-1} Stokes vibrational band. The spectrograph scanned a 5 nm range from 592 to 597 nm. The scan rate was 5 nm/minute. Each spectrum is the sum of 75 repetitive scans, resulting in a total dwell time of 45 s/channel. All of the data presented in this section were obtained using the above procedures.

The objective of the first experiment was to demonstrate the reproducibility of the Raman band shapes for steam. This experiment also showed the applicability of the previously developed data analysis procedure to steam spectra.

Four Raman spectra were recorded for steam at atmospheric pressure and 110 K vapor superheat ($T-T_{SAT}$, T_{SAT}=373 K). The raw data for these runs is shown in Figure 5.10. The effect of smoothing and normalization is shown in Figures 5.11 and 5.12. The normalized band shapes show good agreement. The deviation of the normalized band shapes from the mean of the four runs is shown in Figure 5.13. Differences between the band shapes are relatively small and vary randomly about zero. The RMS deviation from the mean band shape is 1.0 percent of the mean peak intensity.

The uncertainty in the Raman band shapes observed for steam is slightly larger than that observed for atmospheric nitrogen in the preliminary experiments. This increase is at least partly attributable to variation of the steam sample temperature. In the preliminary studies of atmospheric nitrogen, the sample temperature was constant within less than 1 K, whereas the steam temperature varied over a 10 K range due to boiler fluctuations.

In the second experiment, variations in the Raman vibrational band shape were observed as a function of temperature. Raman spectra were recorded from the steam jet at atmospheric pressure for vapor superheats ($T-T_{SAT}$, T_{SAT}=373 K) ranging from 20 to 190 K. Two spectra were observed at each temperature to illustrate reproducibility.

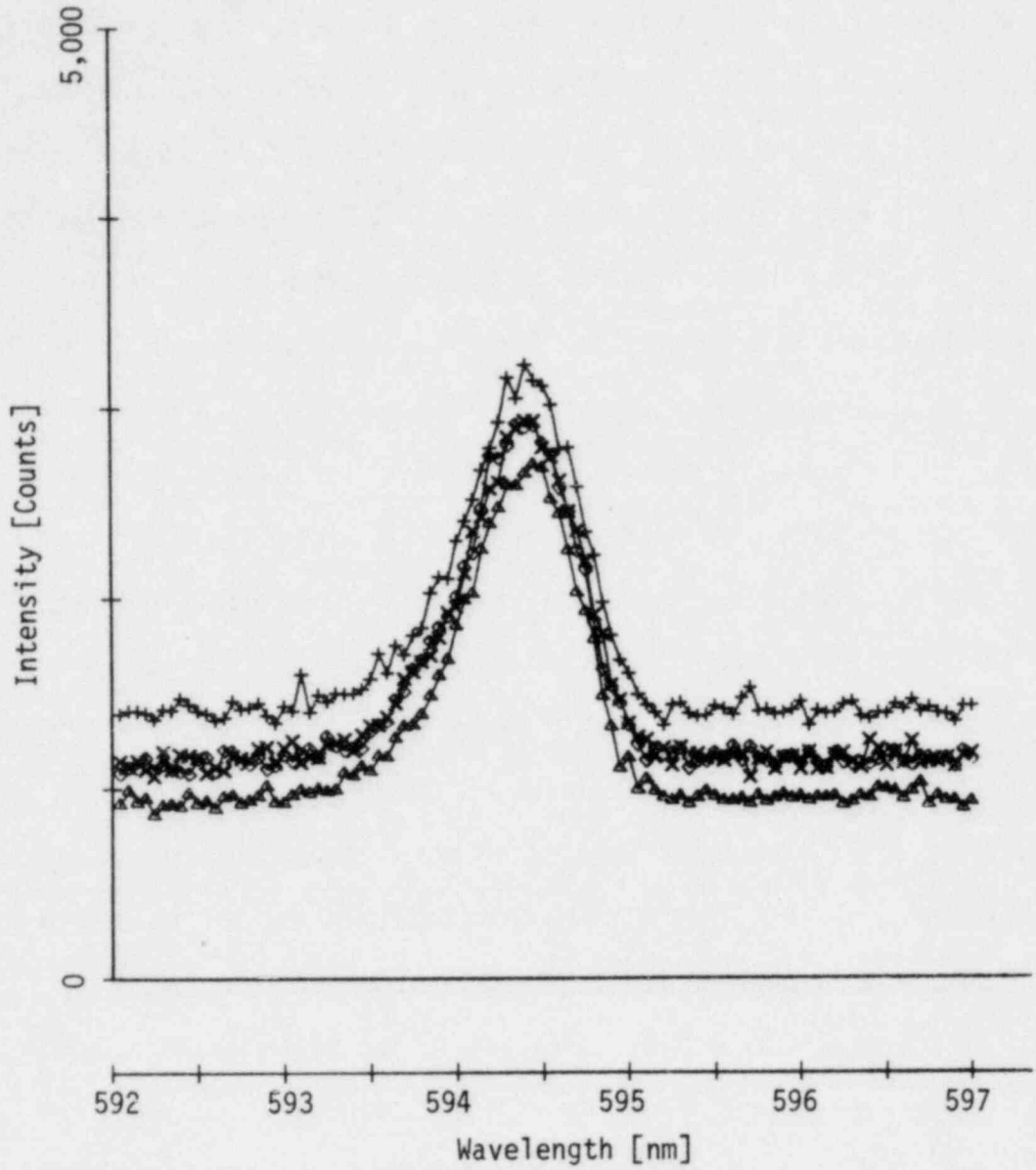

Figure 5.10 Four Raman spectra, steam at atmospheric pressure, 110 K vapor superheat ($T-T_{SAT}$, T_{SAT} = 373 K) (raw data)

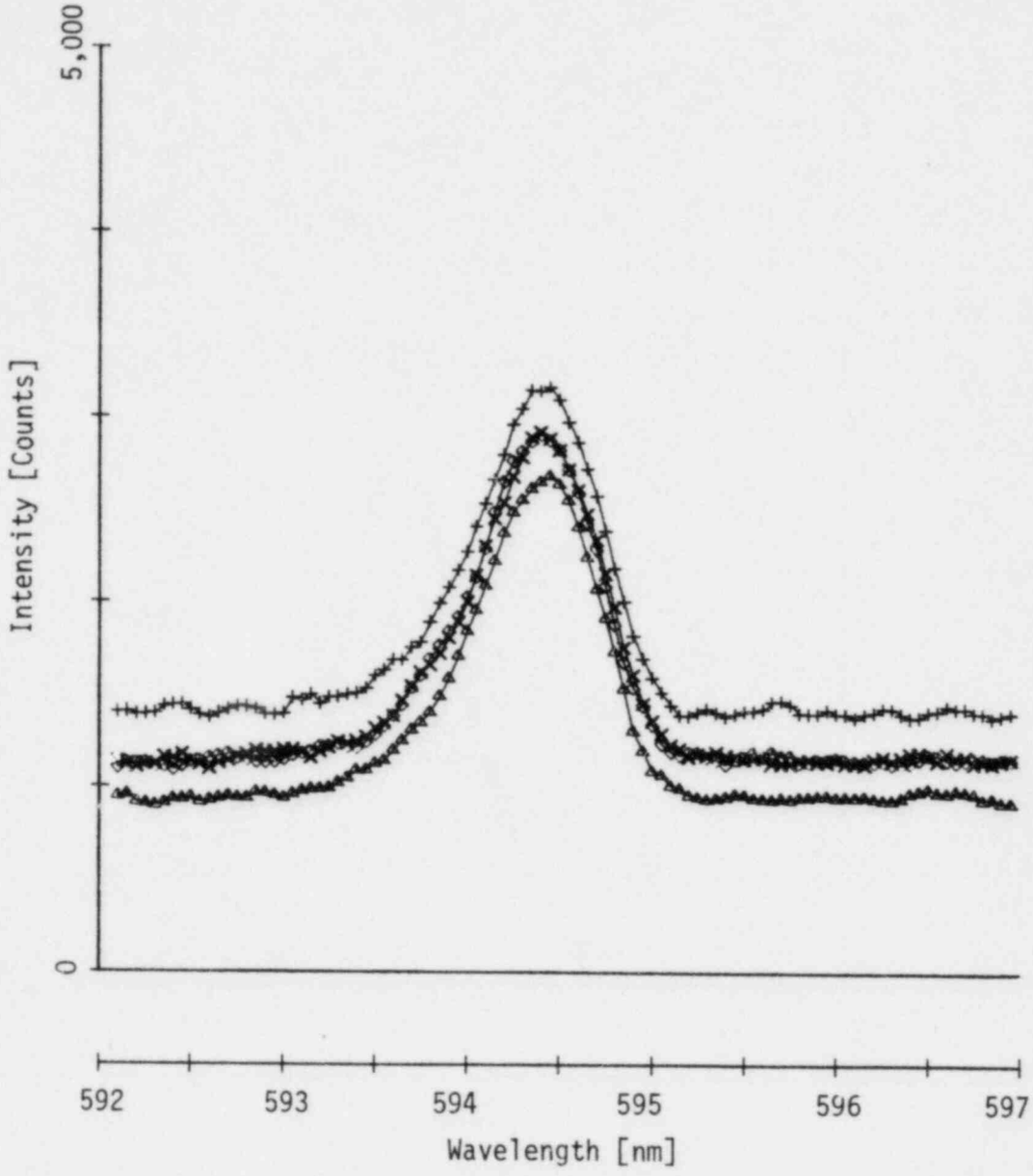

Figure 5.11 Four smoothed Raman spectra, steam at atmospheric pressure, 110 K vapor superheat

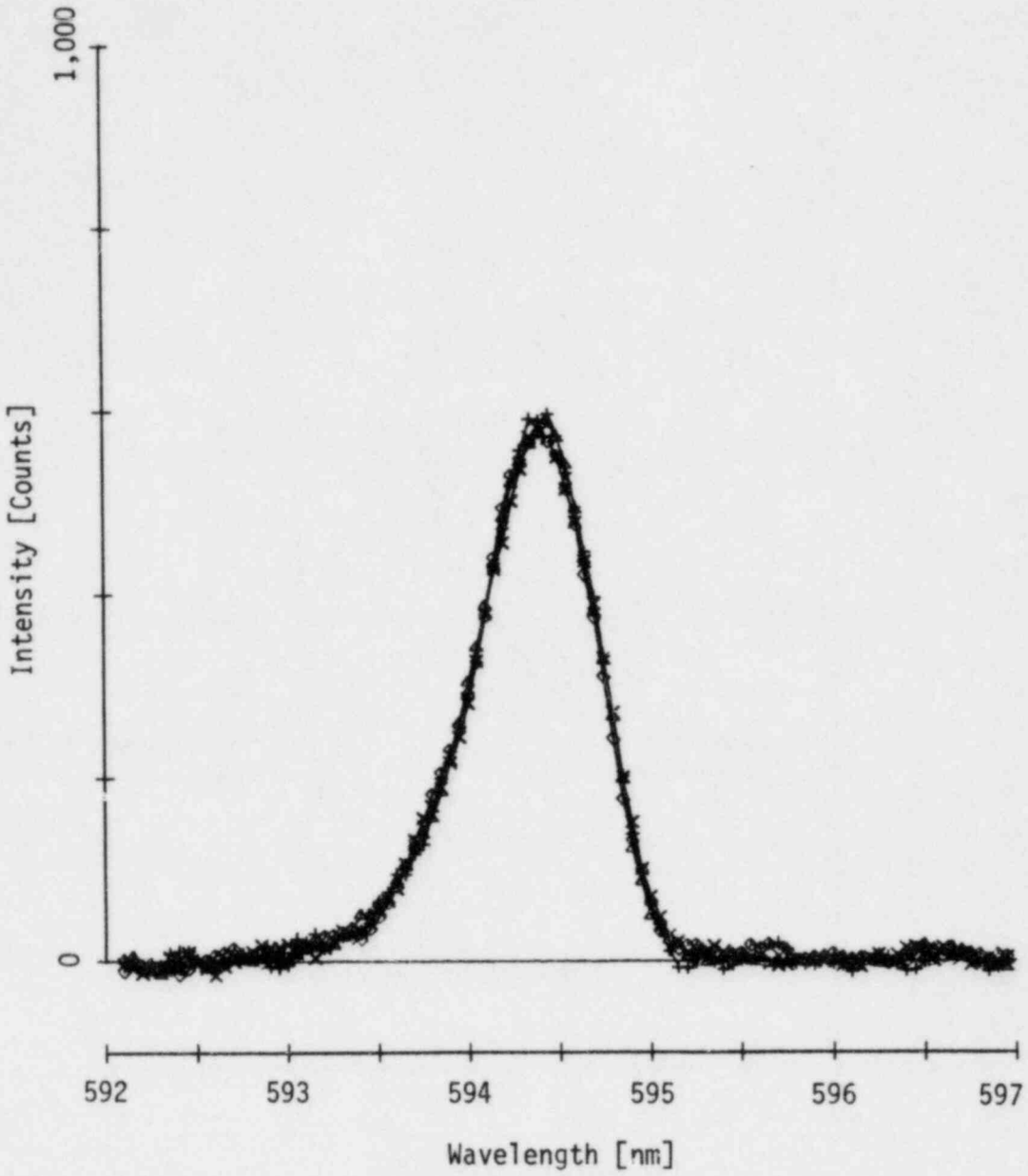

Figure 5.12 Four normalized Raman spectra, steam at atmospheric pressure, 110 K vapor superheat

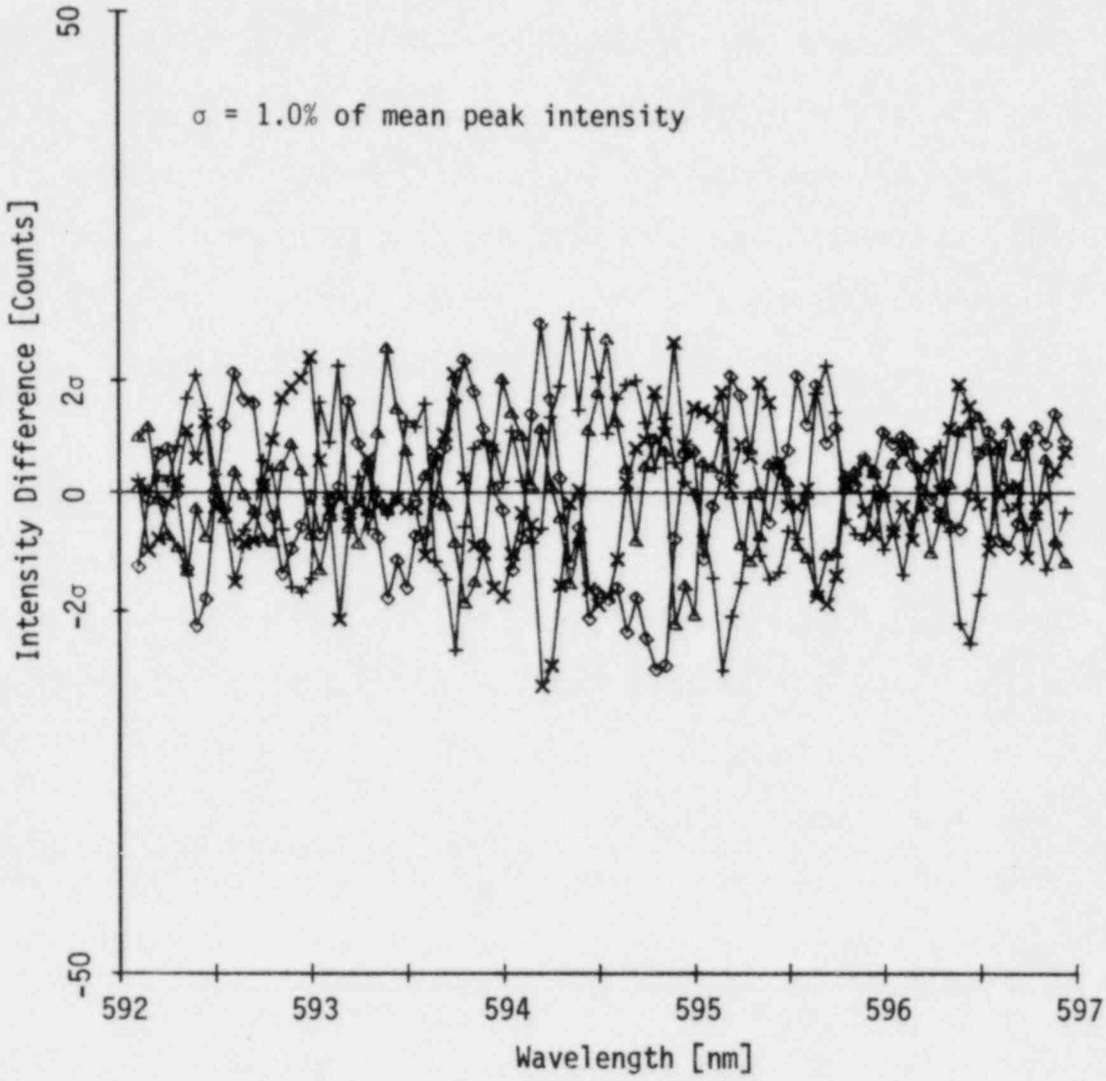

Figure 5.13 Four difference spectra, steam at atmospheric pressure, 110 K vapor superheat

Typical raw data are shown in Figures 5.14 and 5.15. The total Raman signal into the band ranged from 600 to 1,000 counts/s. The scattering intensity is proportional to the density of the sample; so, as the temperature increased at constant pressure, the density, and thus the signal decreased.

Normalized band shapes for pairs of spectra observed at the same temperature show close agreement (see Figures 5.16 to 5.19). The RMS deviation from the mean of these pairs ranged from 0.8 to 1.4 percent of the mean peak intensity as shown in Figures 5.17 and 5.19.

Normalized band shapes for 20, 105 and 190 K vapor superheat ($T-T_{SAT}$, T_{SAT}=373 K) are shown in Figure 5.20. Data for 60 and 150 K vapor superheat have been omitted from the plot for clarity. Careful comparison of the band shapes reveals the effect of temperature. At the lowest temperature, the spectrum is narrowest. At the higher temperatures, the normalized peak intensity is lower and the spectrum is broader. The intensity increases with temperature over the left side of the spectrum and decreases with temperature over the right side. These trends agree qualitatively with previously published Raman vibrational contours for steam in this temperature range [5.8].

Variation of the band shapes with temperature is highlighted in Figure 5.21. This figure shows the difference between each of the normalized band shapes and the mean of the two 20 K vapor superheat runs. This plot clearly shows that variation of the band shapes

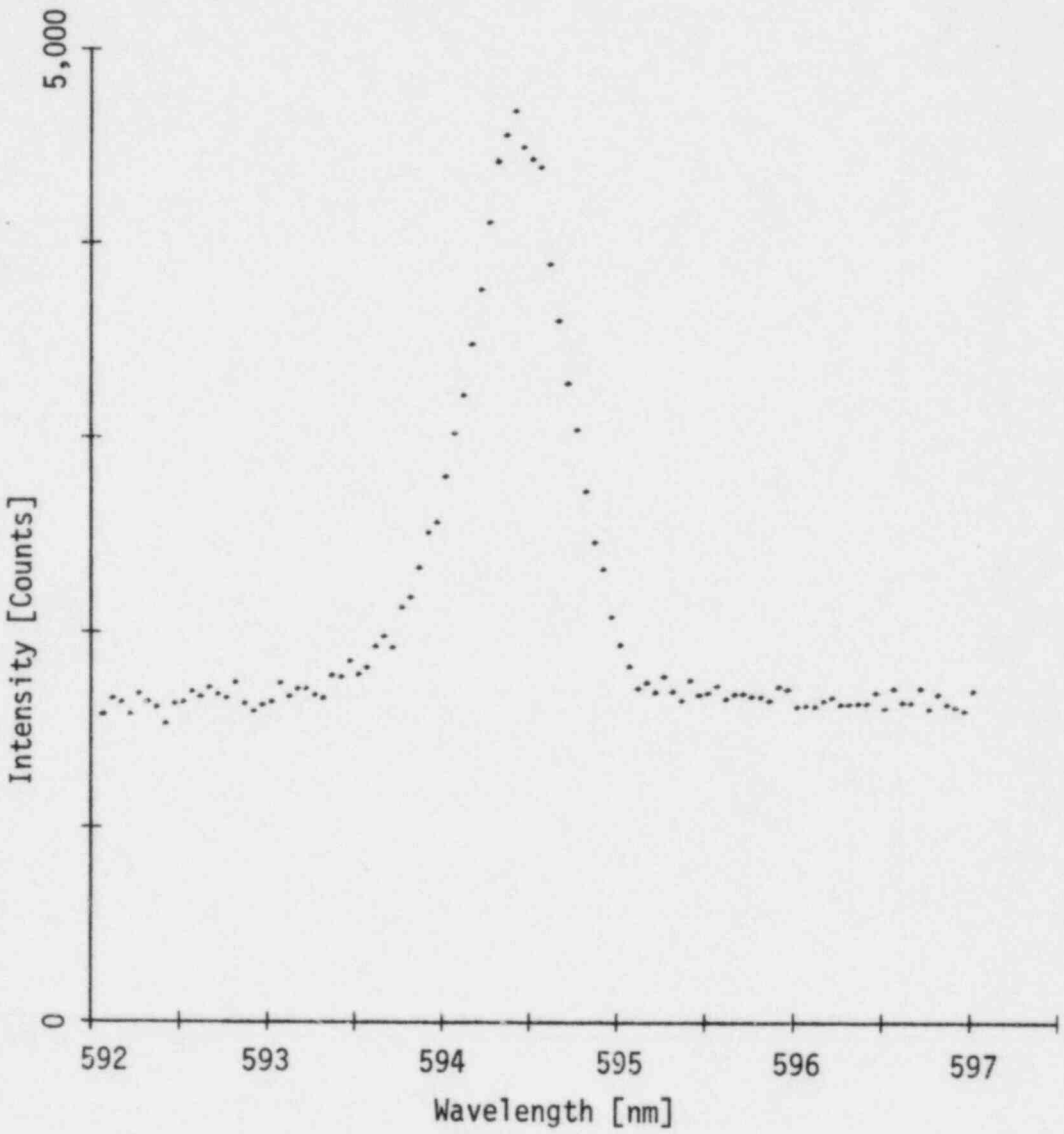

Figure 5.14 Raman spectrum of steam at atmospheric pressure, 20 K vapor superheat ($T-T_{SAT}$, T_{SAT} = 373 K) (raw data)

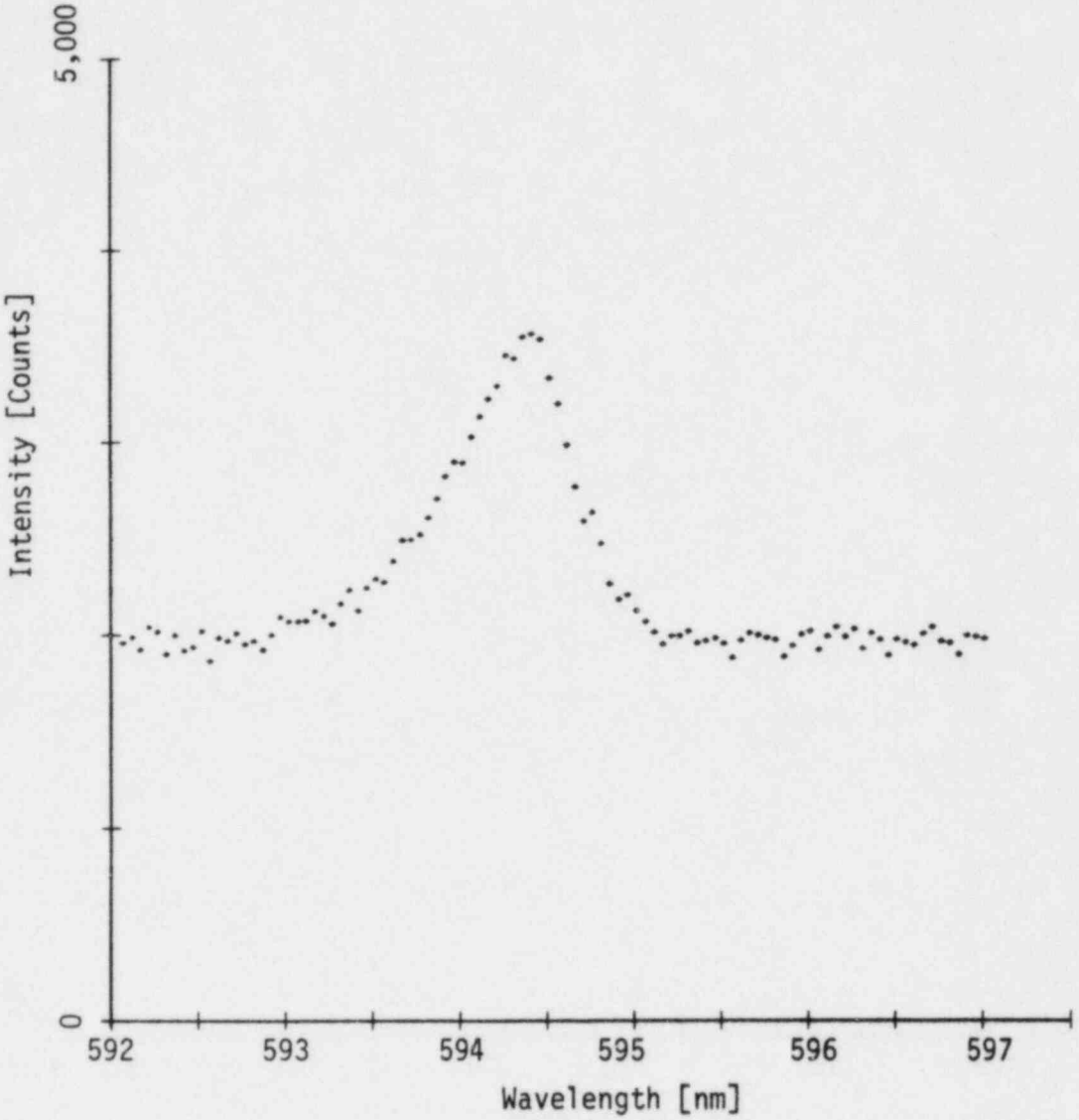

Figure 5.15 Raman spectrum of steam at atmospheric pressure, 190 K vapor superheat ($T-T_{SAT}$, $T_{SAT} = 373$ K) (raw data)

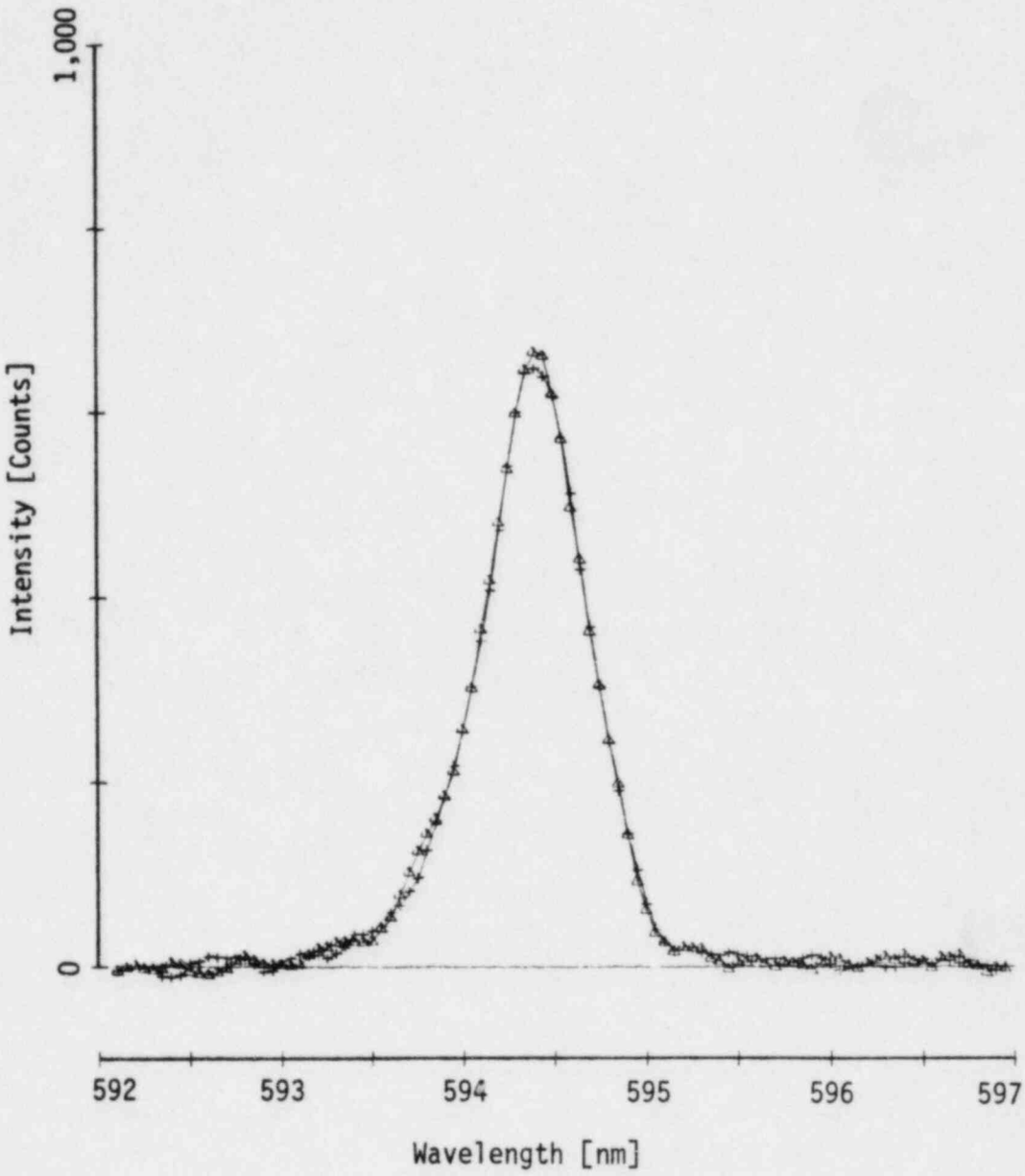

Figure 5.16 Two normalized Raman spectra, steam at atmospheric pressure, 20 K vapor superheat

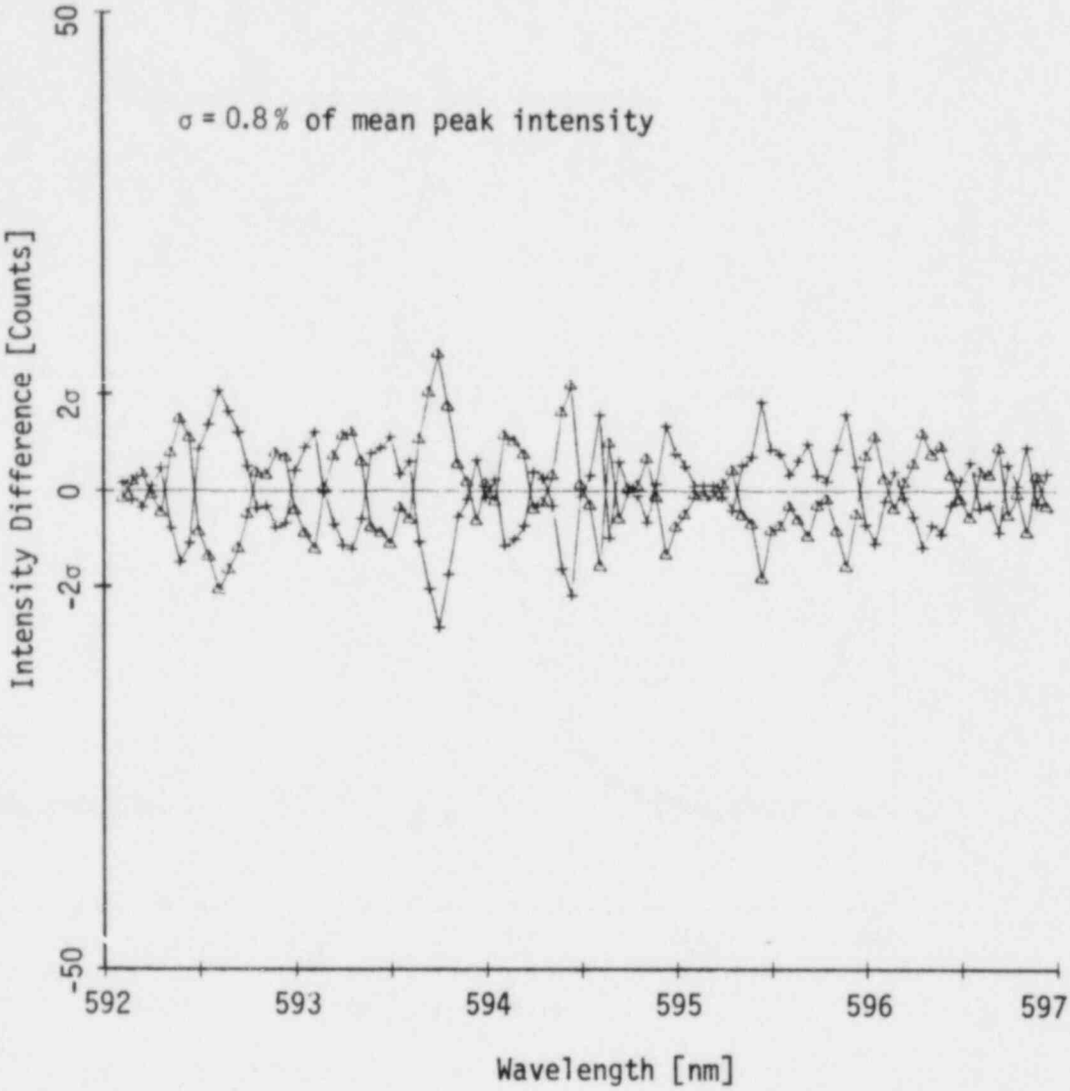

Figure 5.17 Two difference spectra, steam at atmospheric pressure, 20 K vapor superheat

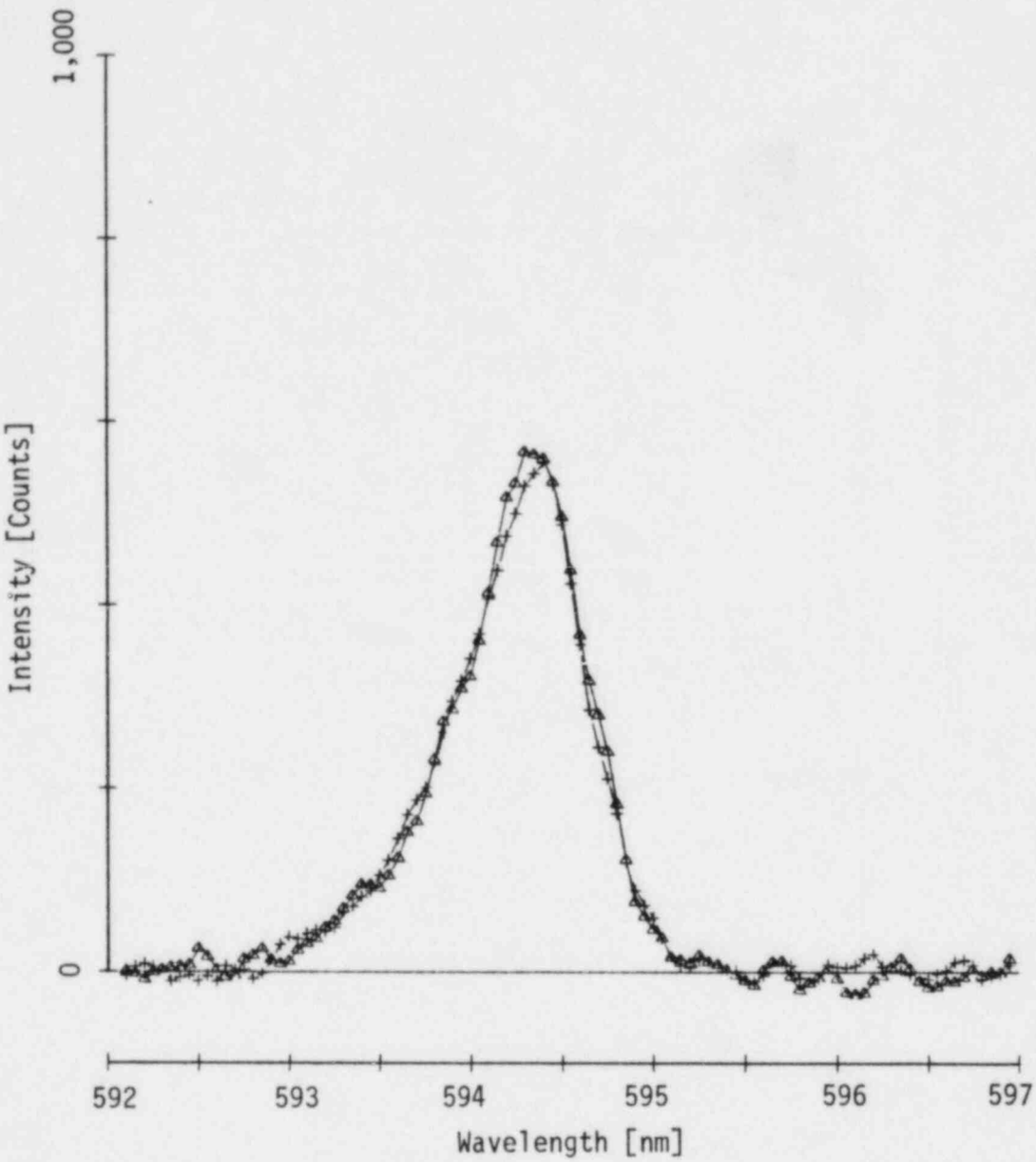

Figure 5.18 Two normalized Raman spectra, steam at atmospheric pressure, 190 K vapor superheat

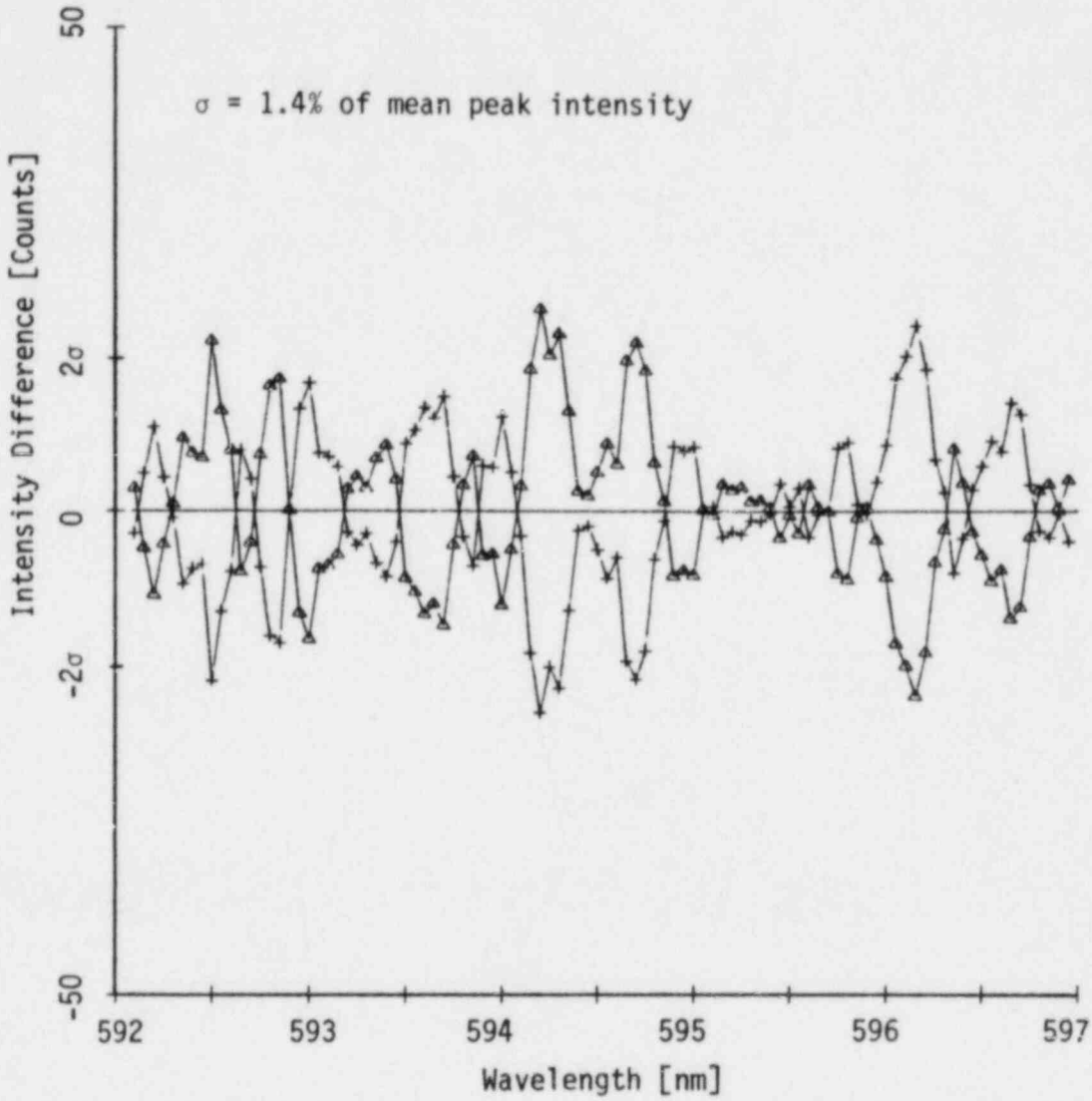

Figure 5.19 Two difference spectra, steam at atmospheric pressure, 190 K vapor superheat

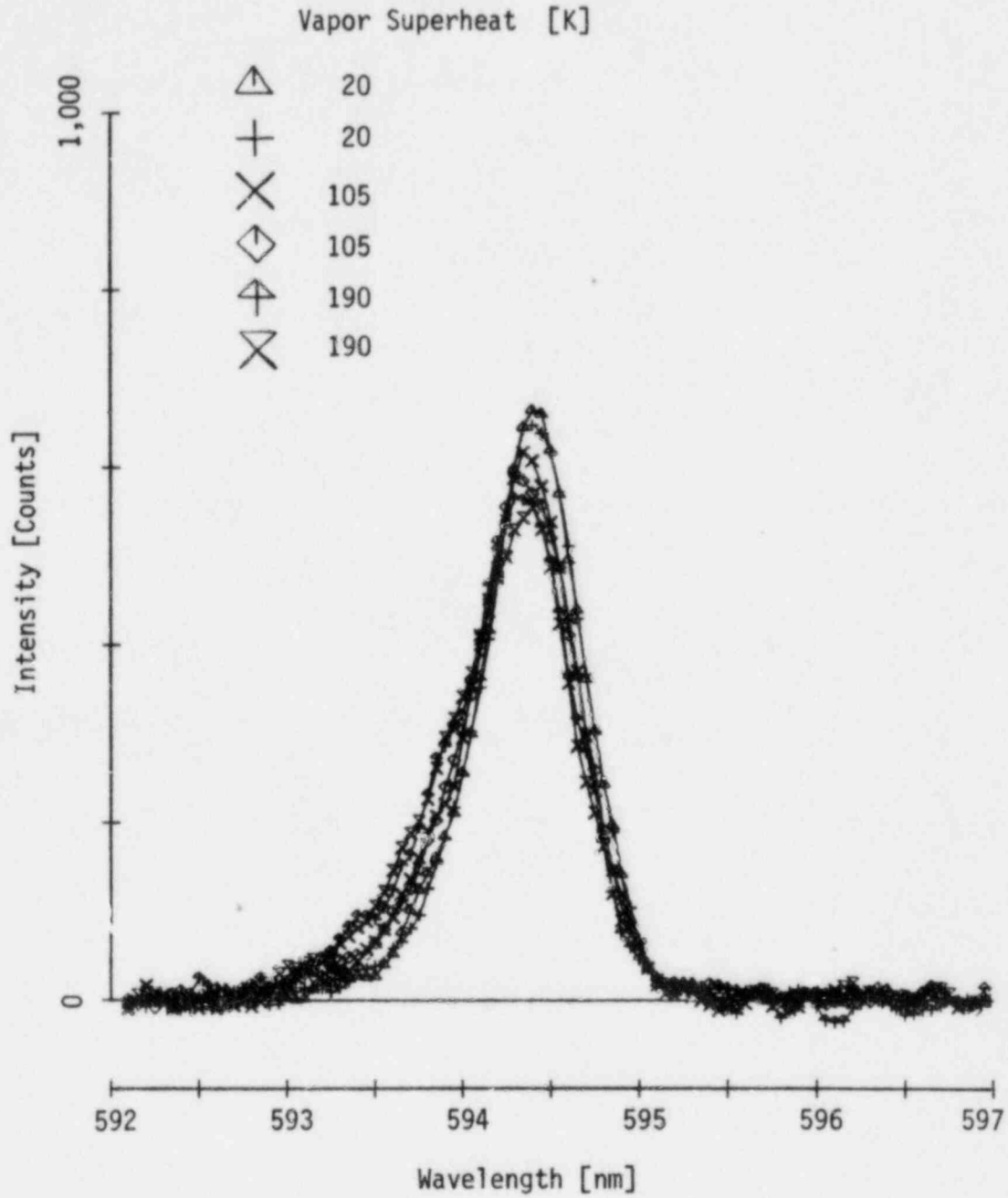

Figure 5.20 Six normalized Raman spectra, steam at atmospheric pressure, 20, 105, and 190 K vapor superheat

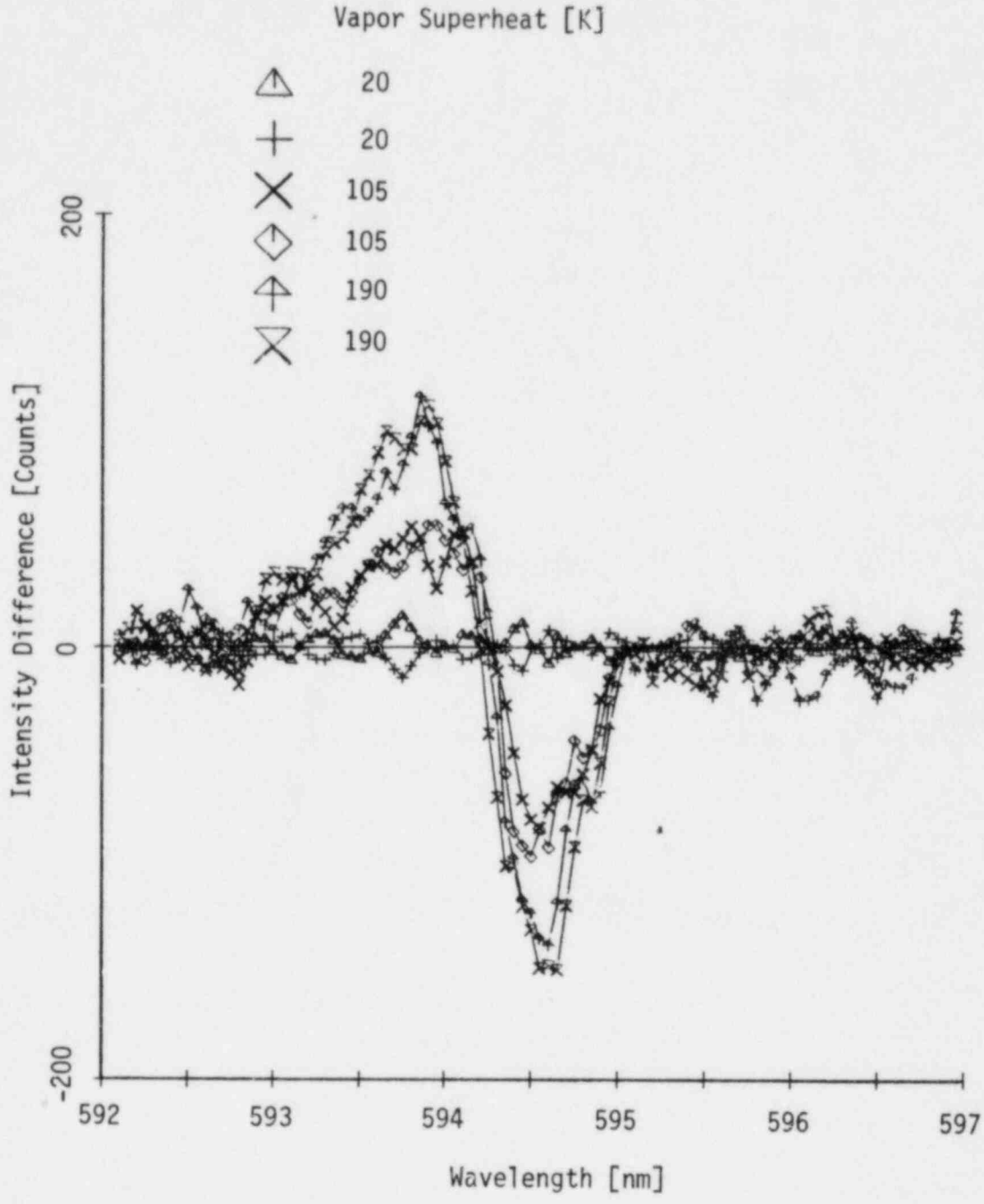

Figure 5.21 Difference between normalized steam spectra for 20, 105, and 190 K vapor superheat and mean of two 20 K vapor superheat spectra

with temperature is larger than the uncertainty between runs at the same temperature.

The above discussion qualitatively illustrates the effect of temperature on the observed band shapes. Intensity ratios calculated from these band shapes were used to estimate the temperature sensitivity quantitatively.

As mentioned previously, Figures 5.20 and 5.21 show that the intensity increases with temperature over the left side of the spectrum and decreases with temperature over the right side. A temperature sensitive ratio, R, was formed by dividing the spectrum in two and taking the ratio of the intensity integrated over the two sides.

$$R(T) = \left[\int_{592\ nm}^{\lambda_D} I(\lambda)d\lambda/(\lambda_D-592)\right] \Big/ \left[\int_{\lambda_D}^{597\ nm} I(\lambda)d\lambda/(597-\lambda_D)\right] \tag{5.9}$$

These integrals were calculated from the normalized band shapes by summing the intensity over the appropriate channel numbers using equation (5.10).

$$R(T) = \sum_{i=2}^{d} \bar{I}_{N,i} \Big/ \sum_{i=d+1}^{n-1} \bar{I}_{N,i} \tag{5.10}$$

where d is the channel number corresponding to wavelength λ_D.

The normalized band shapes for all of the temperatures intersect in the range from 594.0 to 594.4 nm. For maximum temperature sensitivity, λ_D should be within this range. The effect of varying

λ_D was investigated by calculating R(T) for a range of values of d.

The intensity ratios calculated from the normalized steam spectra are listed in Table 5.1 and plotted in Figure 5.22. The lines and uncertainty bands plotted with the intensity ratios were calculated using least square linear regression. Regression and correlation coefficients are listed in Table 5.2. These results show that λ_D has a strong effect on the intensity ratios.

The accuracy of temperature measurements using these ratios depends on how the intensity ratio varies with temperature and on how accurately the ratio can be measured [5.9]. The uncertainty of a temperature measurement, ΔT is given by equation (5.11).

$$\Delta T = \Delta R/(dR/dT) \tag{5.11}$$

where ΔR is the uncertainty in the measured intensity ratio and dR/dT is the variation of the ratio with temperature.

In selecting the optimal value for λ_D we sought to minimize ΔT. The uncertainty in the measured intensity ratio, ΔR, was estimated to be twice the RMS deviation of the measured ratios from the regression line. The variation of the intensity ratio with temperature, dR/dT, was estimated by the slope of the regression line. The resulting uncertainties, ΔT, are listed in Table 5.2. This analysis shows that the optimal temperature sensitivity is obtained by dividing the spectrum at λ_D = 594.2 nm.

Table 5.1 Integrated intensity ratios for single-phase steam

Spectrum No.	Vapor Superheat [K] ($T-T_{SAT}$, T_{SAT}=373 K)	λ_D[nm] 594.0	594.1	594.2	594.3	594.4
		Intensity Ratios, R				
81	20	.227	.358	.576	.961	1.652
82	20	.227	.353	.568	.948	1.599
83	60	.253	.401	.660	1.117	1.919
84	60	.302	.466	.751	1.239	2.115
85	105	.349	.527	.811	1.318	2.199
86	105	.355	.531	.830	1.333	2.170
87	150	.409	.612	.951	1.523	2.565
88	150	.408	.606	.938	1.581	2.588
89	190	.482	.704	1.075	1.712	2.854
90	190	.502	.720	1.068	1.660	2.742

$$R = \left[\int_{592\ nm}^{\lambda_D} I(\lambda)d\lambda/(\lambda_D-592)\right] / \left[\int_{\lambda_D}^{597} I(\lambda)d\lambda/(597-\lambda_D)\right]$$

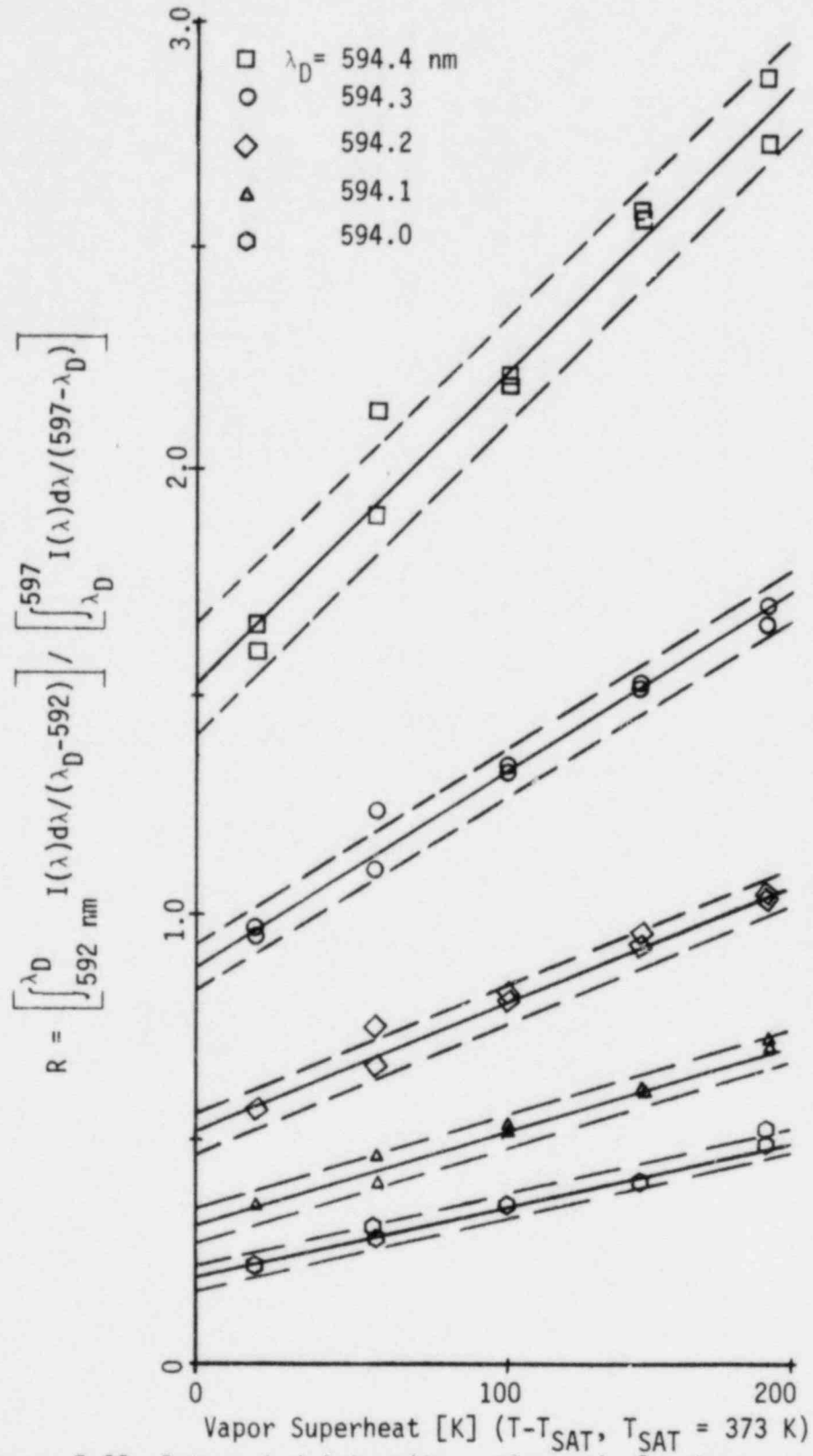

Figure 5.22 Integrated intensity ratios, single-phase steam data

Table 5.2 Correlation of integrated intensity ratios with vapor superheat for single-phase steam

λ_D [nm]	m[1/K][1]	b[1]	c[2]	σ_R[3]	ΔT [K][4]
594.0	.00154	.190	.987	.014	18.2
594.1	.00206	.311	.992	.017	16.5
594.2	.00287	.521	.992	.022	15.3
594.3	.00419	.893	.991	.035	16.7
594.4	.00675	1.532	.985	.073	21.6

Notes:

1 $R = m \cdot T + b$, R = intensity ratio, m = slope of regression line [1/K], T = vapor superheat [K], b = intercept

2 correlation coefficient

3 RMS deviation from regression line

4 $\Delta T = 2\sigma_R/m$, uncertainty in the vapor superheat correlation

$$R_1(T) = \left[\int_{592\ nm}^{594.2} I(\lambda)d\lambda/(594.2-592)\right] / \left[\int_{594.2}^{597} I(\lambda)d\lambda/(597-594.2)\right] = \sum_{i=2}^{44} \bar{I}_{N,i} / \sum_{i=45}^{99} \bar{I}_{N,i} \qquad (5.12)$$

The estimated uncertainty of temperature measurements using this intensity ratio is ±15 K.

Alternative intensity ratios were formed by considering narrow spectral regions where variation of the band shape with temperature is strongest. The largest increase and decrease of intensity with temperature occur at 593.85 and 594.60 nm respectively. The ratio of the intensities for these wavelengths is a temperature sensitive parameter.

$$R_2(T) = I(\lambda=593.85)/I(\lambda=594.60) \qquad (5.13)$$

This ratio uses only two data points from each spectrum and is simple to calculate. Values for $R_2(T)$ are listed in Table 5.3 and plotted in Figure 5.23. The uncertainty of a temperature measurement based on this ratio was evaluated using equation (5.11) as with the integrated intensity ratios presented earlier (see Table 5.4). The uncertainty, ΔT, is ±28 K which is much worse than the integrated intensity ratio, $R_1(T)$. In an attempt to reduce the uncertainty, the intensity was integrated over one channel on each side of 593.85 and 594.60 nm. The resulting intensity ratio, $R_3(T)$,

Table 5.3 Single wavelength and narrow band integrated intensity ratios for single-phase steam

Spectrum No.	Vapor Superheat K ($T-T_{SAT}$, T_{SAT}=373 K)	R_2	R_3
81	20	.322	.324
82	20	.302	.306
83	60	.418	.420
84	60	.393	.391
85	105	.482	.481
86	105	.495	.493
87	150	.555	.571
88	150	.549	.562
89	190	.743	.705
90	190	.732	.734

$$R_2 = I(\lambda = 593.85)/I(\lambda = 594.60)$$

$$R_3 = \left[\int_{593.80\ nm}^{593.90} I(\lambda)d\lambda/(.1nm)\right] / \left[\int_{594.55\ nm}^{594.65} I(\lambda)d\lambda/(.1nm)\right]$$

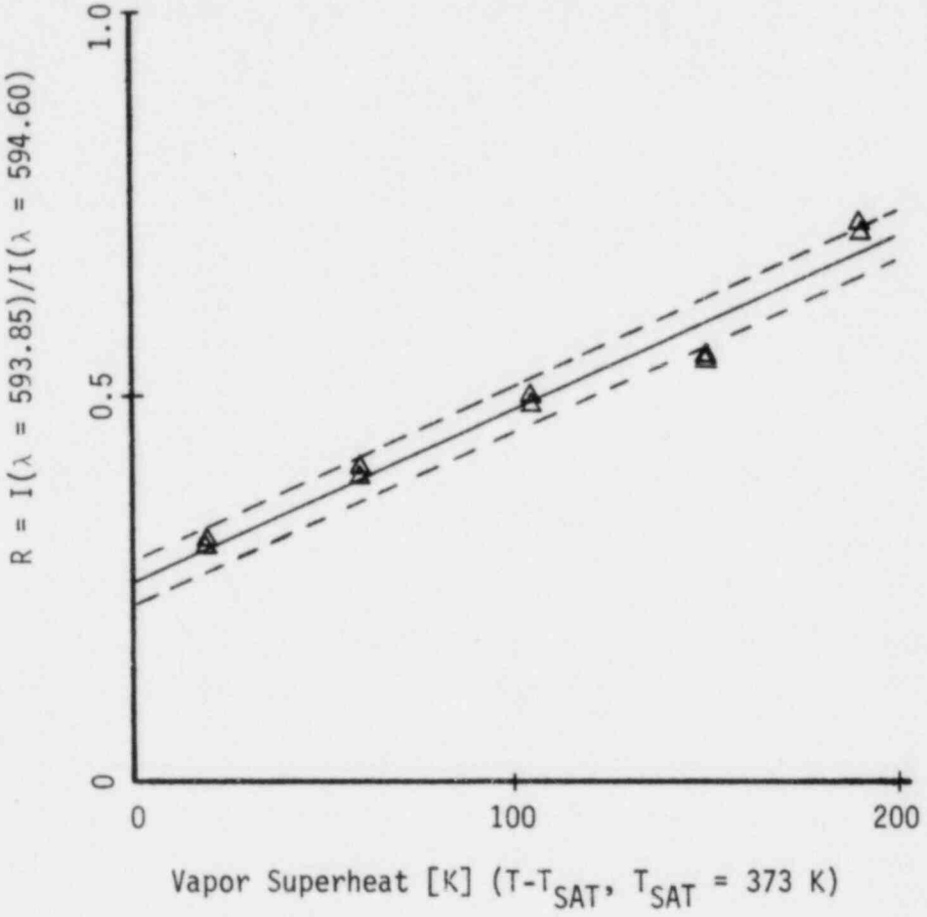

Figure 5.23 Ratio of intensities at two wavelengths as a function of temperature

Table 5.4 Correlation of single wavelength and narrow band integrated intensity ratios with vapor superheat for single-phase steam

Ratio	m[1/K][1]	b[1]	c[2]	σ_R[3]	ΔT[K][4]
R_2	.00231	.256	.976	.032	27.7
R_3	.00225	.262	.985	.024	21.3

Notes:

1 $R = m \cdot T + b$, R = intensity ratio, m = slope of regression line [1/K], T = vapor superheat [K], b = intercept

2 correlation coefficient

3 RMS deviation from regression line

4 $\Delta T = 2\sigma_R/m$, uncertainty in the vapor superheat correlation

is given by equation (5.14).

$$R_3(T) = \left[\int_{593.80\ nm}^{593.90} I(\lambda)d\lambda/(.1nm)\right] / \left[\int_{594.55\ nm}^{594.65} I(\lambda)d\lambda/(.1nm)\right] \quad (5.14)$$

This ratio uses 6 data points from each spectrum. Values for $R_3(T)$ are listed in Table 5.3 and plotted in Figure 5.24. The uncertainty of a temperature measurement based on $R_3(T)$ was estimated to be ±21 K, using equation (5.11) as for $R_1(T)$ and $R_2(T)$. There was a slight reduction in ΔT from the ratio using only two data points, $R_2(T)$, but, the sensitivity is still not as good as the ratio integrated over the entire band, $R_1(T)$.

The first order analysis used above to estimate ΔT gives approximate values for the uncertainty of temperature measurements based on the intensity ratios described. The lack of precisely controlled experimental conditions and the relatively small number of runs do not justify more rigorous statistical analysis.

These experiments showed that the Stokes vibrational Raman band shape for steam can be measured with good reproducibility. The procedures developed earlier for analysis of Raman spectra of atmospheric N_2 were found to be directly applicable to steam spectra. Variations in the Raman band shape for steam have been measured and the effect of temperature has been discussed qualitatively. Intensity ratios were used to characterize the temperature sensitivity of the Raman spectra quantitatively.

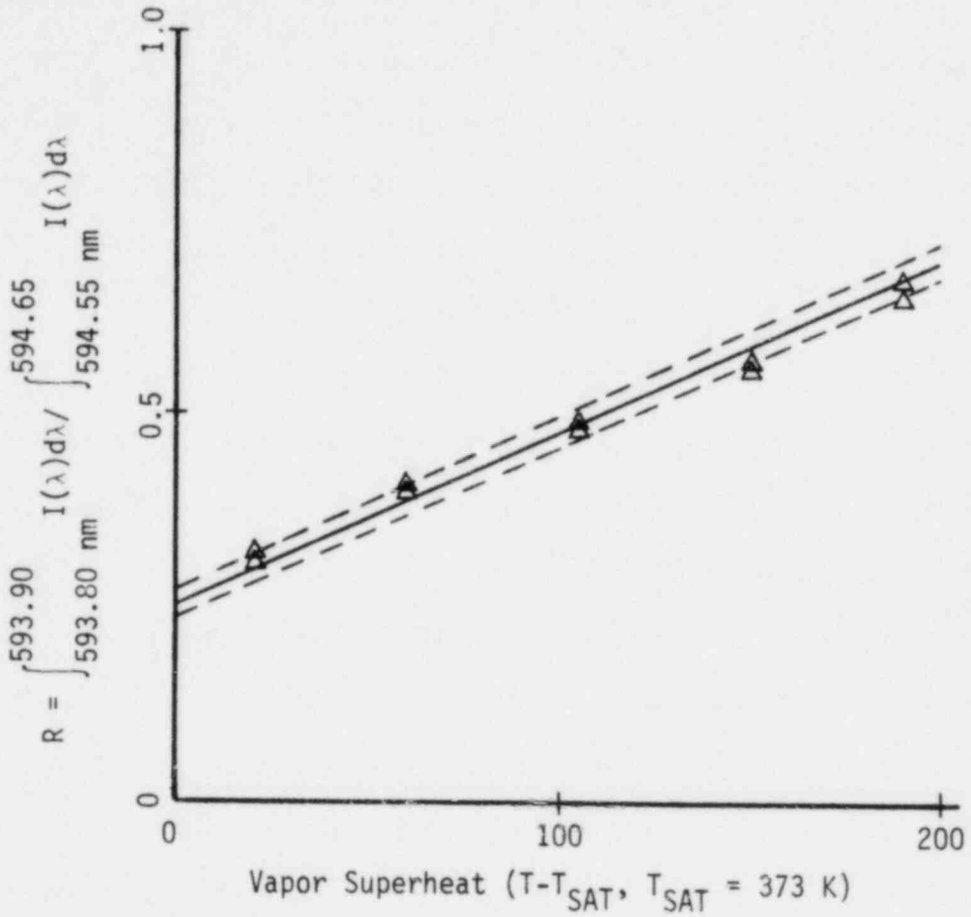

Figure 5.24 Narrow band integrated intensity ratios as a function of temperature

5.5 Raman Scattering From an Air/Water Mist

This section describes observations of Raman scattering from both the gas and liquid phases of an air/water mist. Air was selected as the gas phase for these studies to eliminate condensation and temperature control problems associated with steam. The Raman vibrational band for nitrogen in the ambient air is well separated from the Raman band for liquid water allowing investigation of the effect of Mie scattering independent of the spectral interference between water droplets and water vapor.

The geometry of the sample is illustrated in Figure 5.25. An atomizing nozzle, described in Chapter 3, was used to produce a mist of water droplets in the measurement volume. The laser beam passed through the mist about 10 mm from the nozzle. The mist was drawn into an exhaust duct downstream of the measurement volume.

The water flow rate through the nozzle was about 0.5 gm/s. The void fraction in the measurement volume was estimated to be 70 to 90 percent based on still photographs of the spray.

Raman scattering was first observed from nitrogen in the gas phase of the mist. The bandpass (8 nm), scan limits (548 to 553 nm), speed (5 nm/minute) and number of cycles (75) were the same as those used in earlier observations of Raman scattering from atmospheric nitrogen.

Four spectra were acquired to document the reproducibility of the results. Figure 5.26 shows the raw data for one of these spectra. The presence of liquid droplets in the sample reduced the signal strength by approximately 30 percent and increased the background

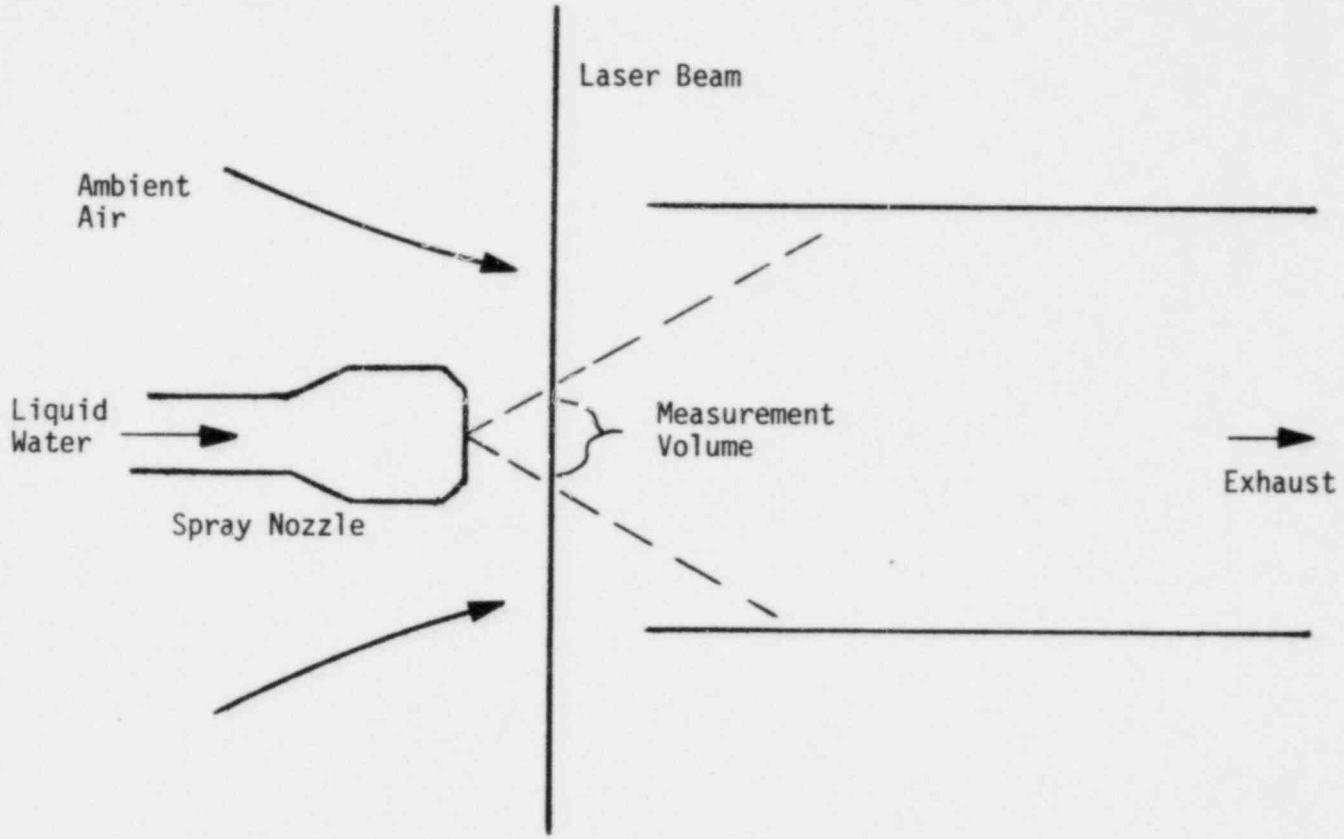

Figure 5.25 Geometry for Raman scattering from an air/water mist

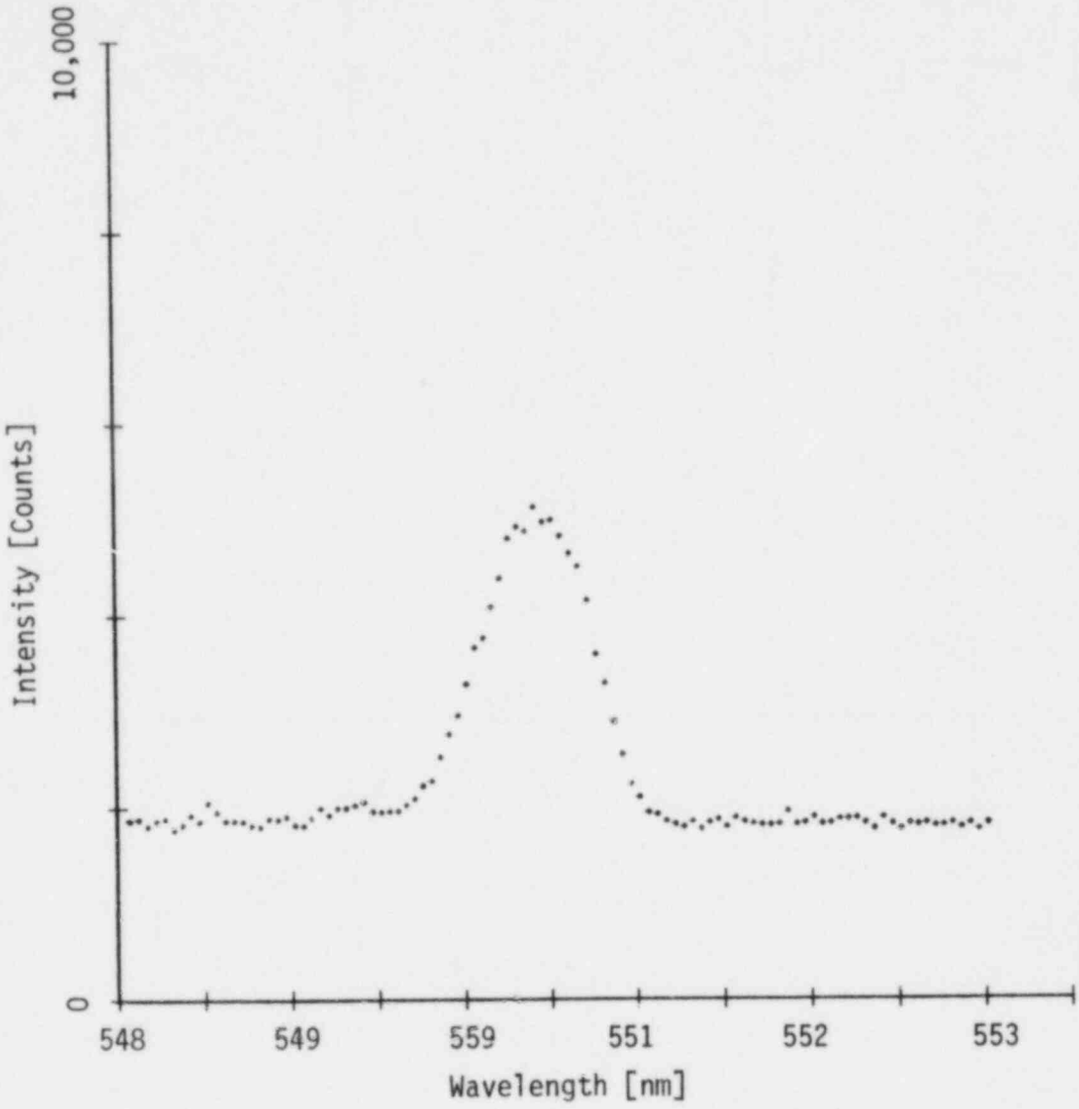

Figure 5.26 Raman spectrum at atmospheric nigrogen at room temperature with dispersed water droplets (raw data)

offset by about 12 percent. In spite of these effects, the band shape is distinct. The spectra were analyzed using the procedure described earlier. The results are shown in Figures 5.27 and 5.28. Three of the normalized band shapes show good agreement. The peak of one spectrum varies slightly from the other three. The RMS deviation from the mean of the four runs is 1.2 percent of the mean peak intensity. The scatter in this data is nearly double that for single-phase samples; however, the uncertainty is still a small fraction of the Raman signal.

In a second experiment, Raman scattering from the liquid droplets was observed. The bandpass (40 nm), scan limits (557.5 to 605.5 nm), and speed used in preliminary observations of the 3400 cm^{-1} Raman band for liquid water were used again here. This experiment showed that Raman scattering can be observed from water droplets at the estimated void fraction of 70 to 90 percent. The detected Raman intensity from the droplets was approximately a factor of 10 less than that observed from a single-phase liquid sample (see Figure 5.29). Raman scattering from the droplets is weak in the spectral region of interest for steam. For measurement of steam spectra, a narrower bandpass (8 nm) is used, off the peak of the liquid band, further reducing the detected intensity from the liquid droplets.

These experiments showed that, although the presence of liquid droplets causes an increase in uncertainty, vibrational band shapes can still be observed from the gas phase of a two-phase mixture with reasonable accuracy. Raman scattering from liquid droplets,

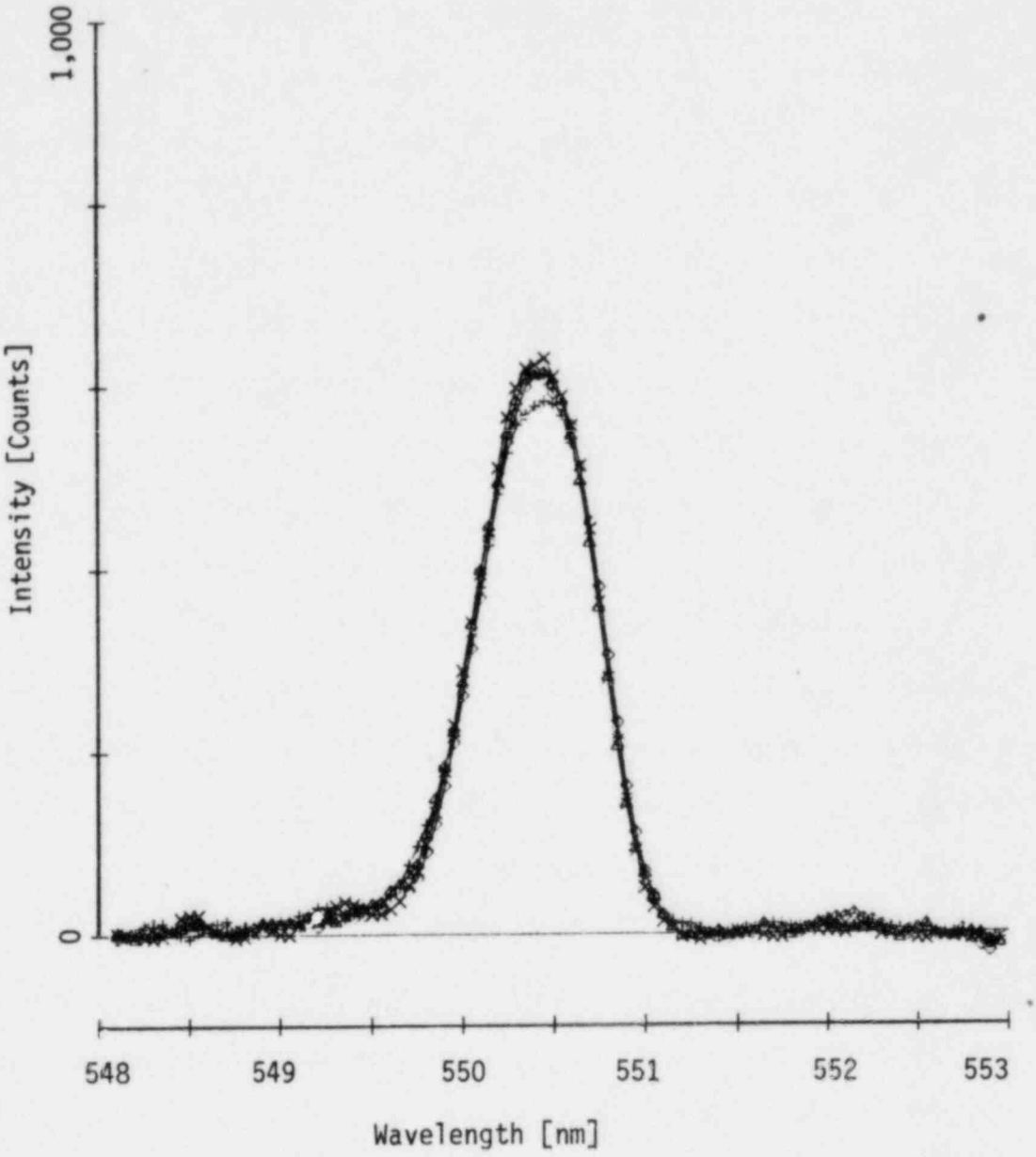

Figure 5.27 Four normalized Raman spectra, atmospheric nitrogen at room temperature with dispersed water droplets

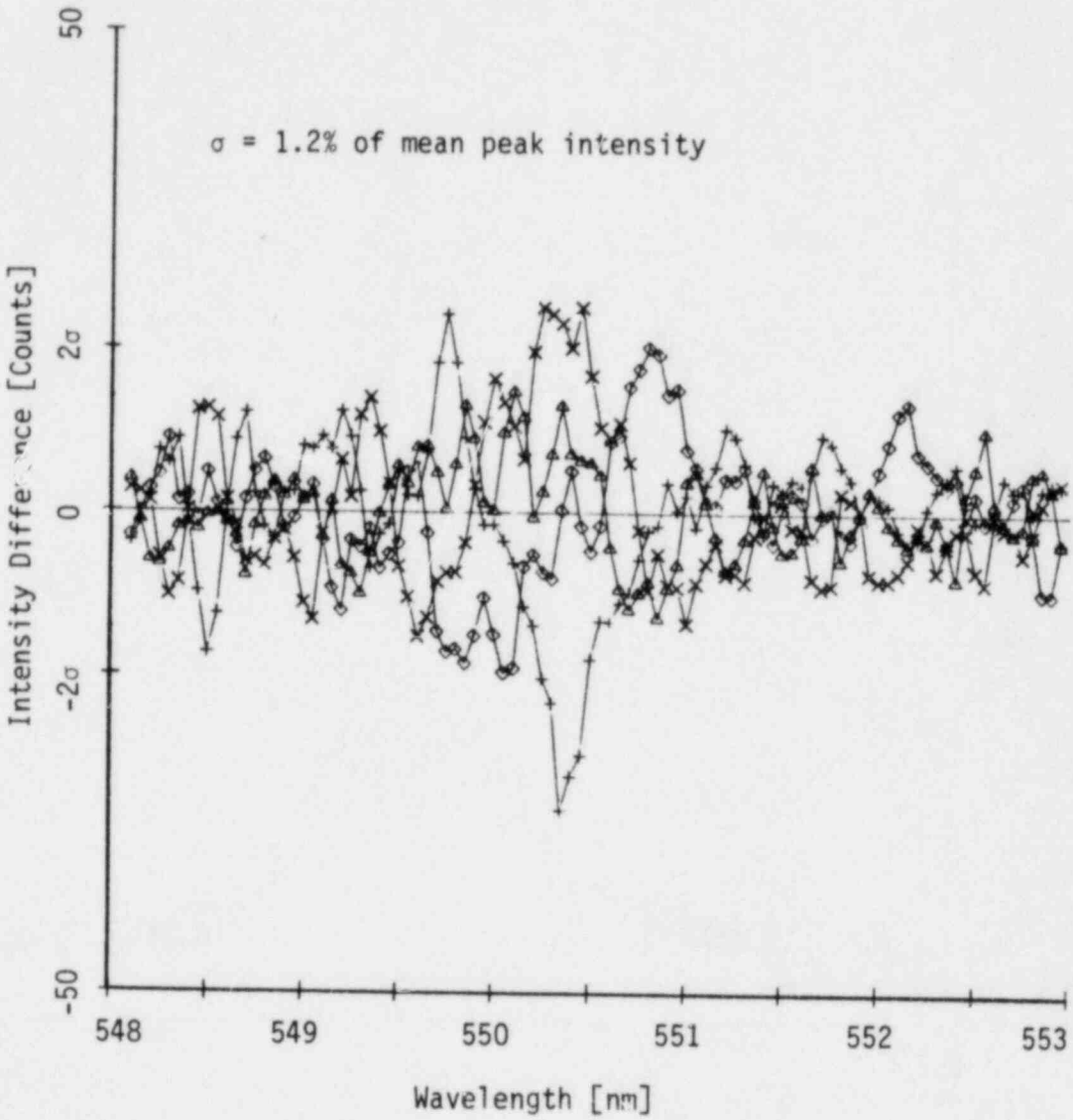

Figure 5.28 Four difference spectra, atmospheric nitrogen at room temperature with dispersed water droplets

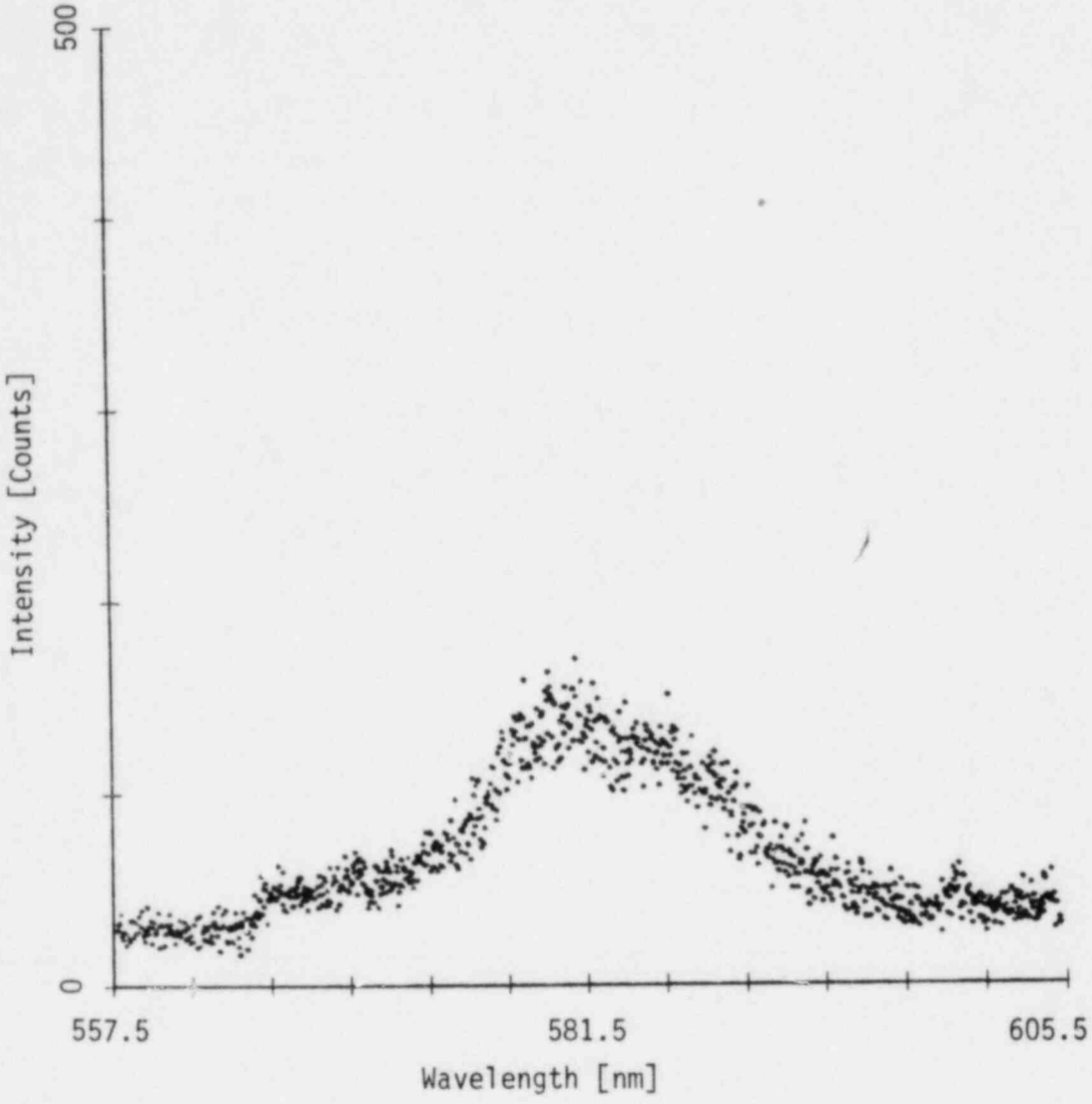

Figure 5.29 Raman spectrum for water droplets in a 70 to 90 percent void fraction mist (raw data)

in the spectral region of interest for steam, is weak but measurable. Scattering from the droplets was expected to make a small contribution to the background offset for steam spectra in nonequilibrium, dispersed two-phase flows, but the effect of this interference was expected to be negligible.

5.6 Raman Spectra of Nonequilibrium Superheated Steam in Dispersed Flow

The final set of experiments conducted in this investigation involved analysis of Raman scattering from nonequilibrium superheated steam with dispersed water droplets. These experiments show that temperature effects on Raman band shapes for steam seen previously in single-phase studies are observable in the presence of liquid droplets. The results have been used to estimate the temperature sensitivity of Raman band shapes for steam in dispersed two-phase flow.

The procedure was similar to that used for investigation of temperature effects on Raman scattering from single-phase superheated steam. A series of spectra were recorded for a constant nonequilibrium vapor superheat to demonstrate the reproducibility of the band shapes. A second series of spectra were recorded over a range of nonequilibrium vapor superheats to determine the effect of temperature on the band shapes.

The steam generator and spray nozzle, described in Chapter 3 were used to produce two-phase samples. Figure 5.30 illustrates the sample geometry. Atomized water droplets mix with superheated steam in the nozzle exit. The steam supply was regulated to

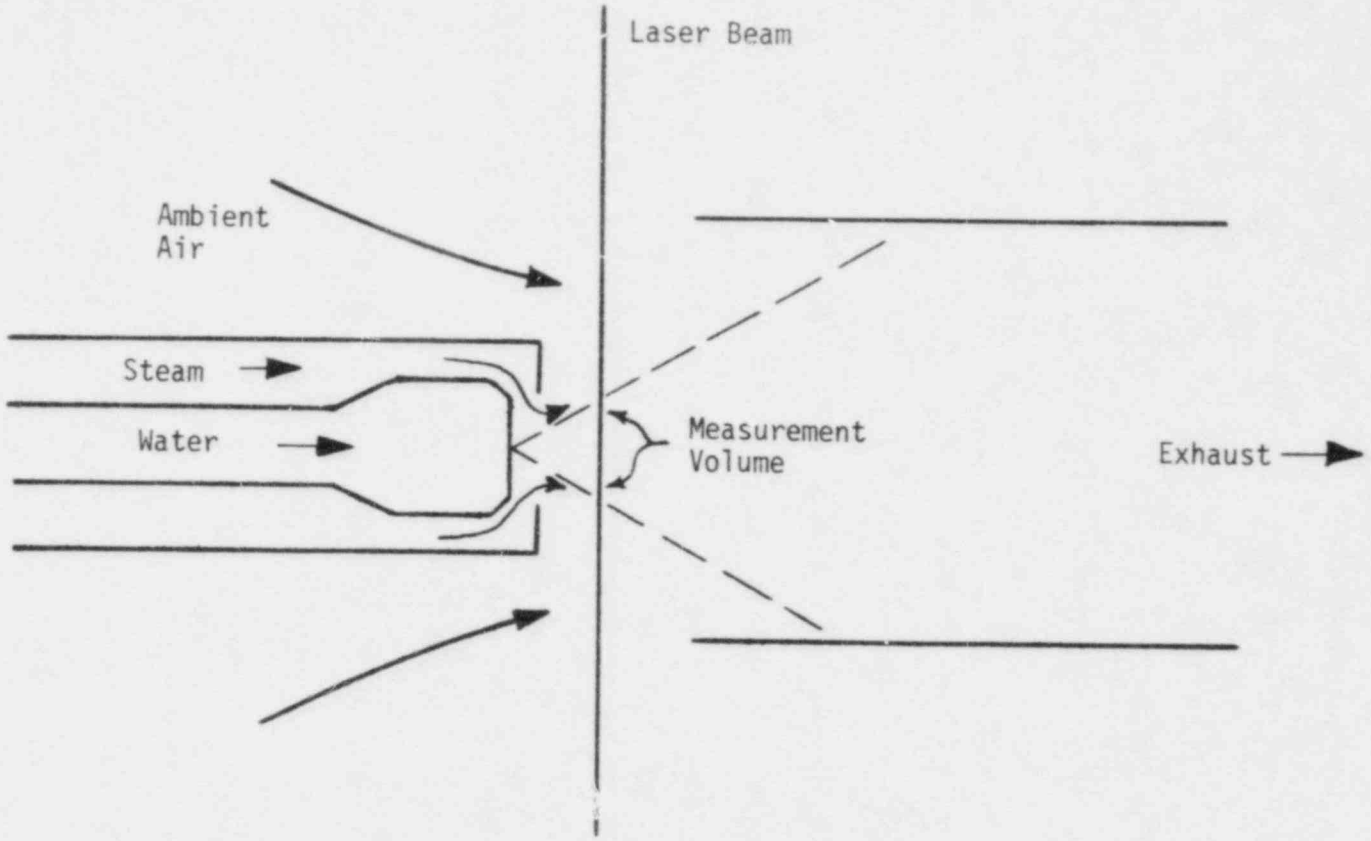

Figure 5.30 Geometry for Raman scattering from nonequilibrium dispersed flow

maintain constant conditions at the nozzle inlet. The average nozzle inlet temperature for each run was used to estimate the nonequilibrium vapor superheat in the measurement volume using the aspirated thermocouple data of Figure 3.16.

The same bandpass (8 nm), scan limits (592 to 597 nm), speed (5 nm/minute) and number of cycles used for earlier measurements in single-phase steam were used again in these two-phase experiments.

In the first experiment, four Raman spectra were observed from a nonequilibrium two-phase sample having a vapor superheat ($T-T_{SAT}$, T_{SAT}=373 K) of about 53 K. The vapor to liquid mass flow ratio was 2.0 ±0.5 and the equilibrium quality was about 67 percent. The estimated void fraction was 70 to 90 percent. Raw data for one of these runs is given in Figure 5.31. The total Raman signal in the band is about 620 counts/s. The average noise level is about 15 counts/s. The relatively low background shows that the effect of Mie and Raman scattering from the liquid droplets is small.

Normalized band shapes for the four runs are shown in Figure 5.32. The RMS deviation of the normalized contours from the mean of the four runs is 1.6 percent of the mean peak intensity as shown in Figure 5.33. The band shapes have been measured with a relatively small uncertainty in spite of dispersed water droplets in the sample.

The second series of spectra were recorded from two-phase dispersed flow samples at atmospheric pressure and nonequilibrium

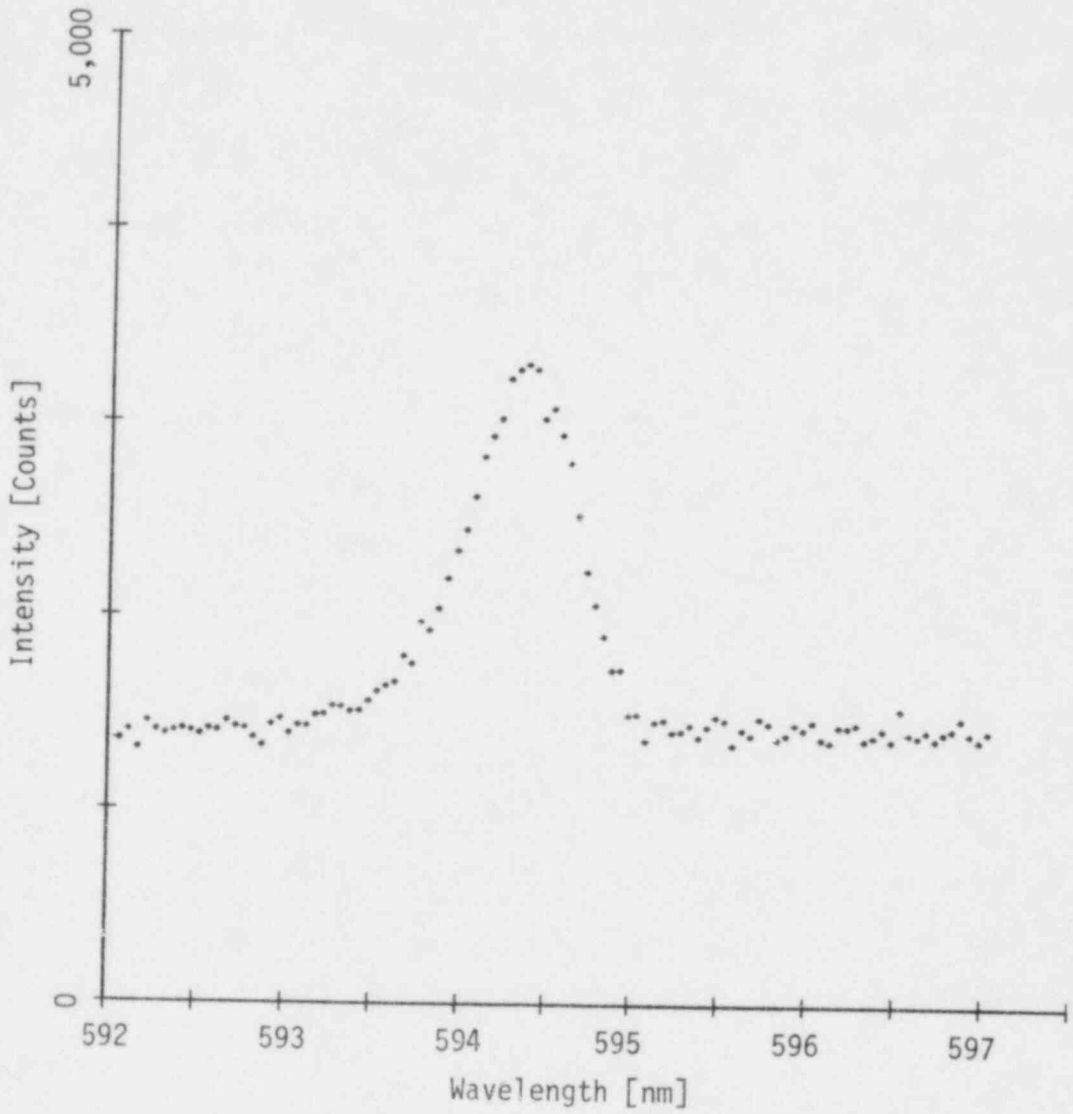

Figure 5.31 Raman spectrum for steam in nonequilibrium dispersed flow, atmospheric pressure, 53 K vapor superheat ($T-T_{SAT}$, T_{SAT} = 373 K) (raw data)

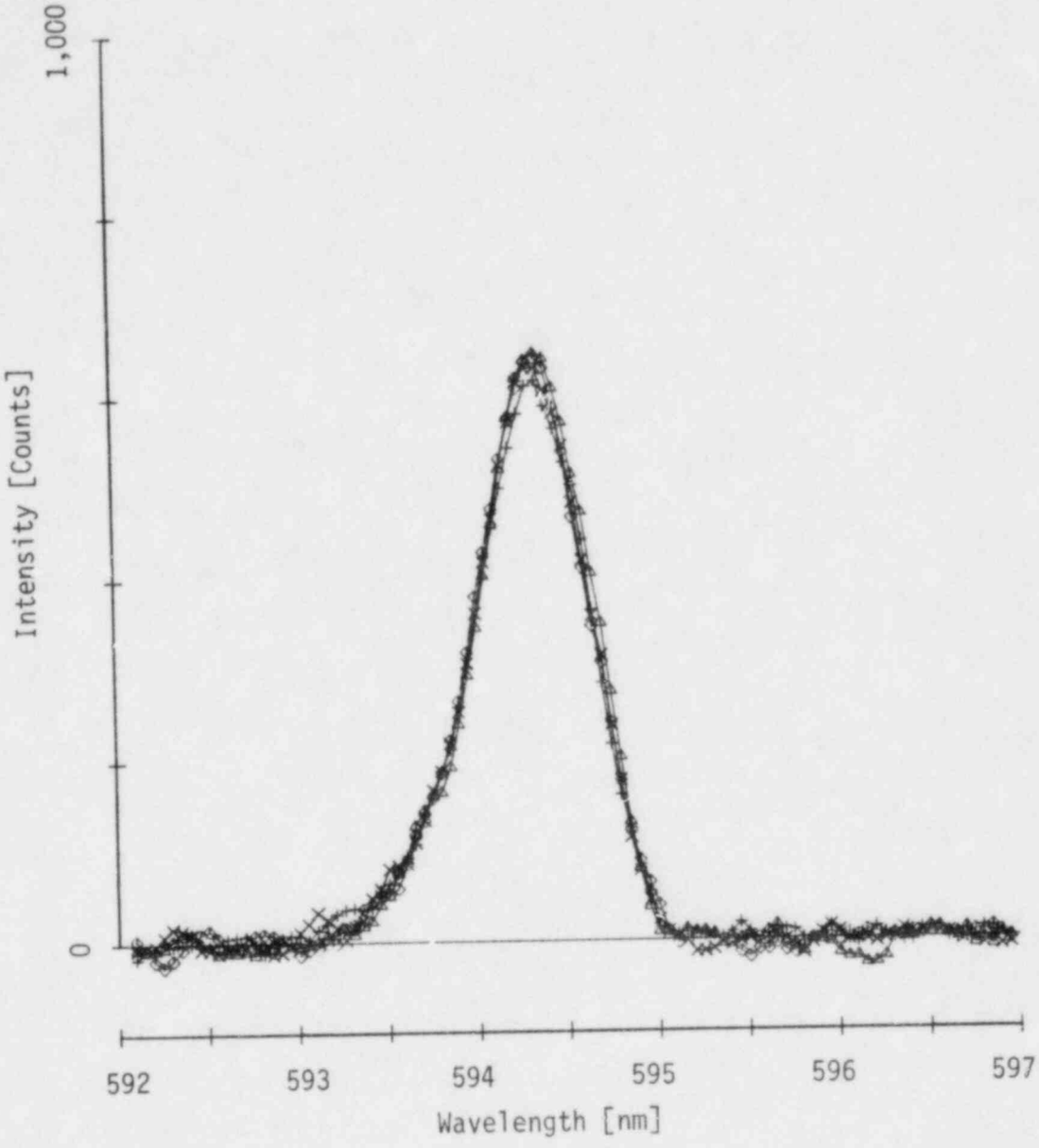

Figure 5.32 Four normalized Raman spectra, steam in non-equilibrium dispersed flow, atmospheric pressure, 53 K vapor superheat

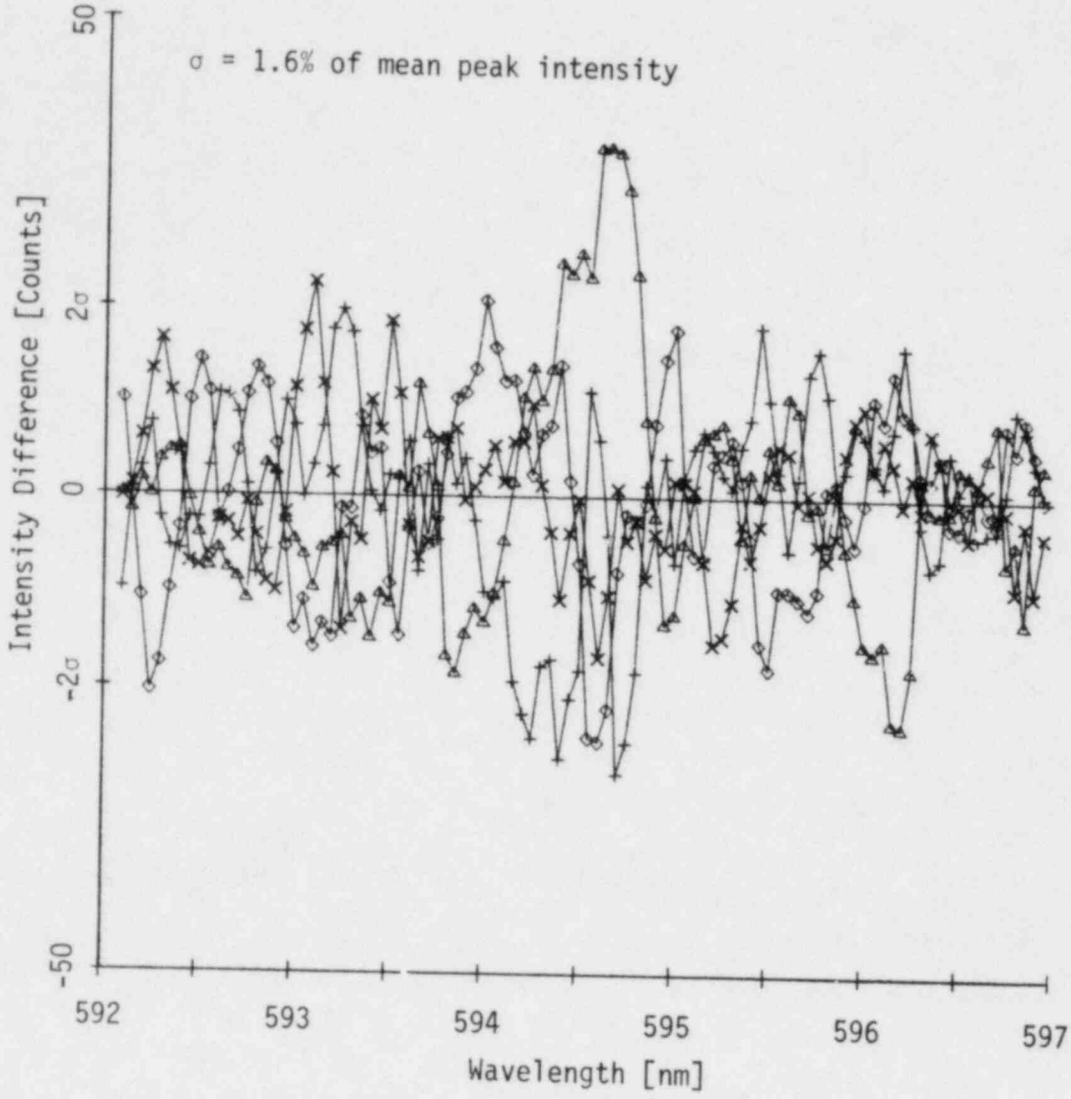

Figure 5.33 Four difference spectra, steam in nonequilibrium dispersed flow, atmospheric pressure, 53 K vapor superheat

vapor superheats ($T-T_{SAT}$, $T_{SAT} = 373$ K) of 20, 50, and 80 K. The vapor to liquid mass flow ratio was 2.0 ±.5 and the equilibrium quality ranged from 62 to 71 percent.

Two spectra were obtained at each temperature to demonstrate reproducibility. The normalized band shapes for pairs of spectra, observed at the same temperature, show fairly good agreement (see Figures 5.34 to 5.37). The RMS deviation between spectra for the same temperature ranges from 1.0 to 1.3 percent of the mean peak intensity for the pair, as shown in Figures 5.35 and 5.37.

The normalized band shapes for the 20 and 80 K superheat runs are shown in Figure 5.38. Data for 50 K superheat has been omitted for clarity. Careful examination of the band shapes reveals the presence of temperature effects seen in previous single-phase steam spectra. At the lower temperature, the band shape is narrower. At the higher temperature, the spectrum is broader and the normalized peak intensity is lower. These variations are highlighted by the difference spectra of Figure 5.39 which clearly shows that the effect of temperature is larger than the uncertainty in the band shapes.

The integrated intensity ratio (R_1, equation (5.12)) which gave the best temperature sensitivity for single-phase steam was used to estimate the temperature sensitivity of Raman band shapes for the two-phase flow. Values for this ratio are listed in Table 5.5 and plotted in Figure 5.40. The uncertainty of temperature measurements based on this ratio was estimated, as for the single-

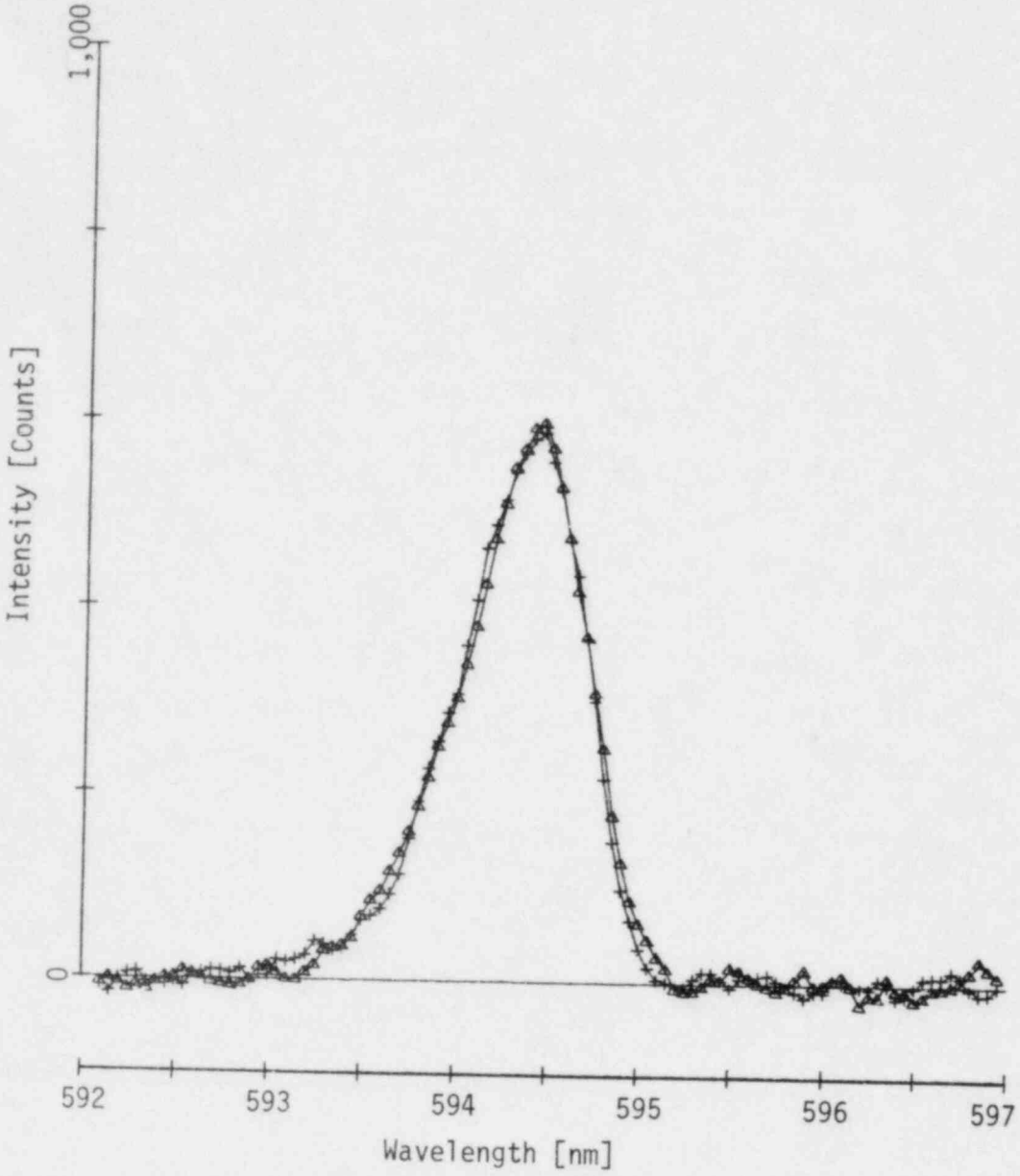

Figure 5.34 Two normalized Raman spectra, steam in non-equilibrium dispersed flow, atmospheric pressure, 80 K vapor superheat ($T-T_{SAT}$, T_{SAT} = 373 K)

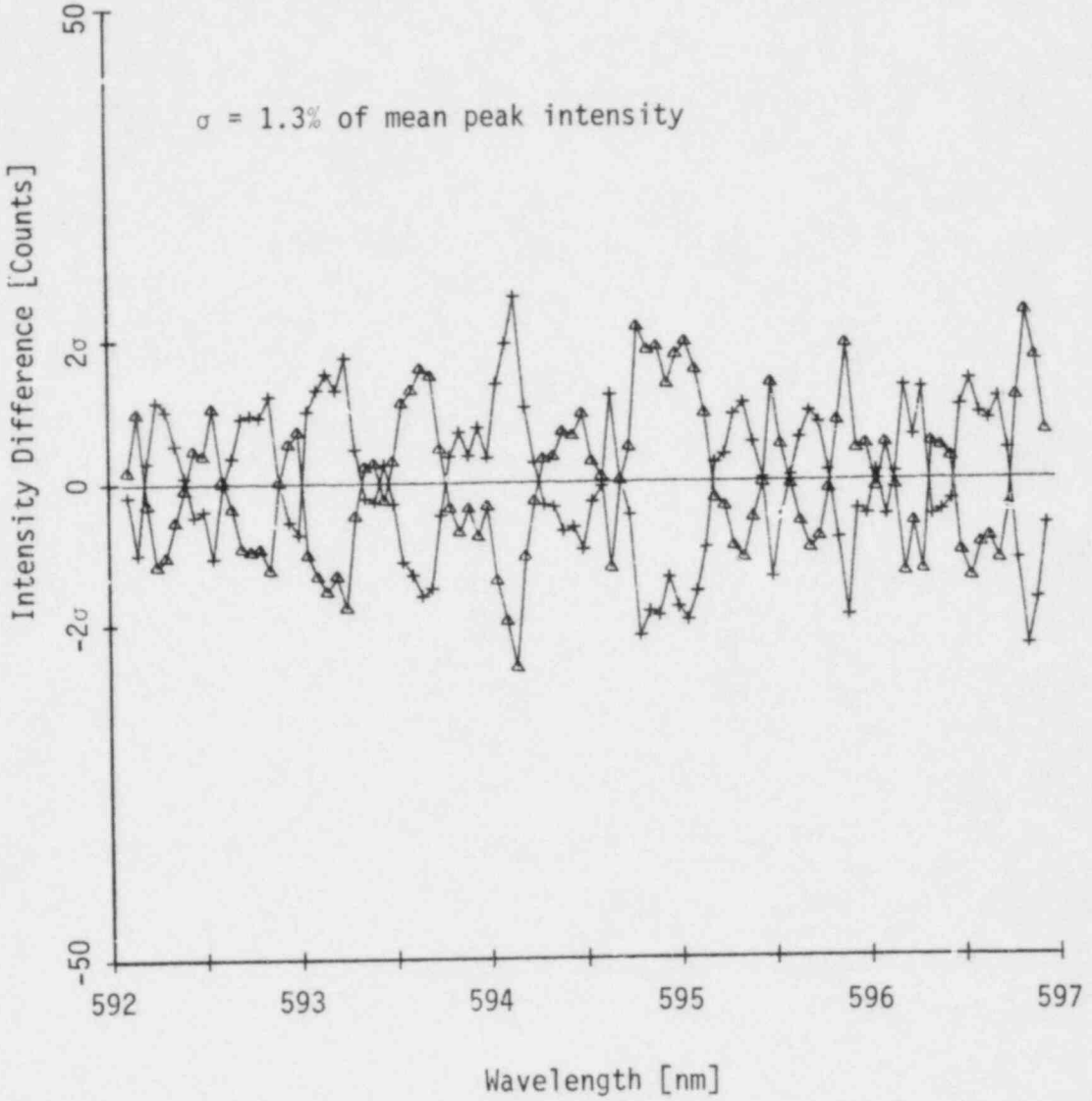

Figure 5.35 Two difference spectra, steam in nonequilibrium dispersed flow, atmospheric pressure, 80 K vapor superheat

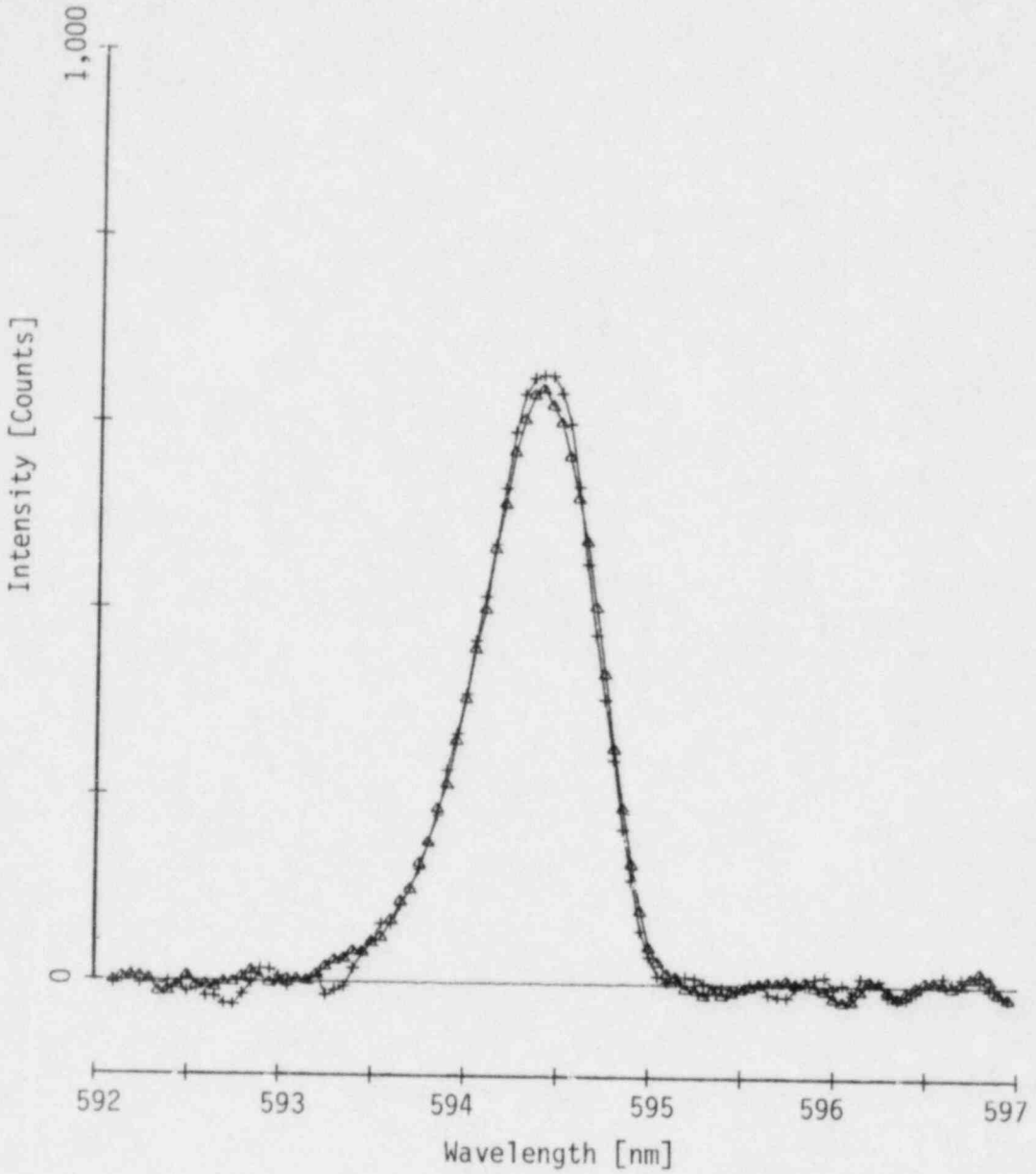

Figure 5.36 Two normalized Raman spectra, steam in non-equilibrium dispersed flow, atmospheric pressure, 20 K vapor superheat

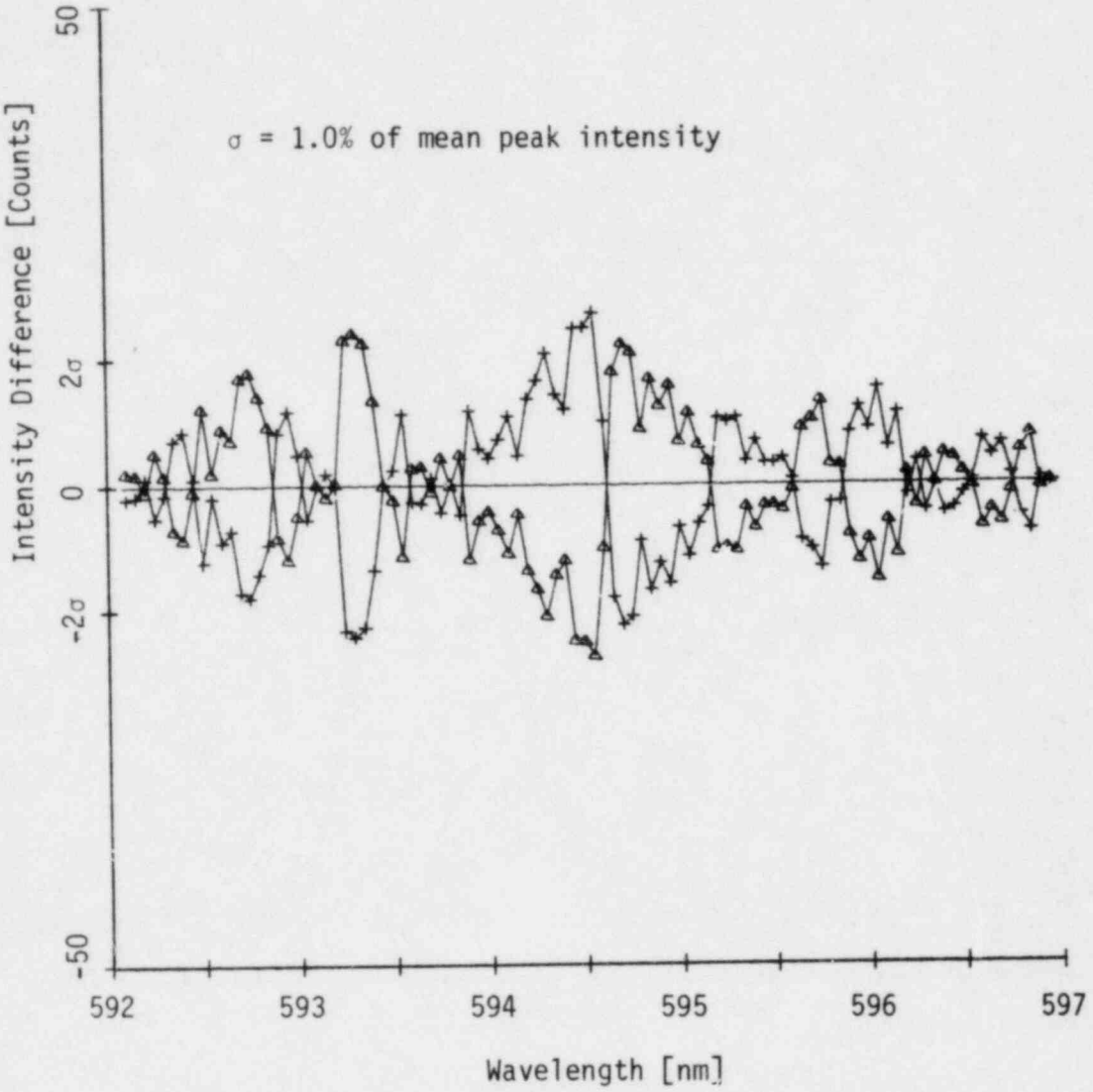

Figure 5.37 Two difference spectra, steam in nonequilibrium dispersed flow, atmospheric pressure, 20 K vapor superheat

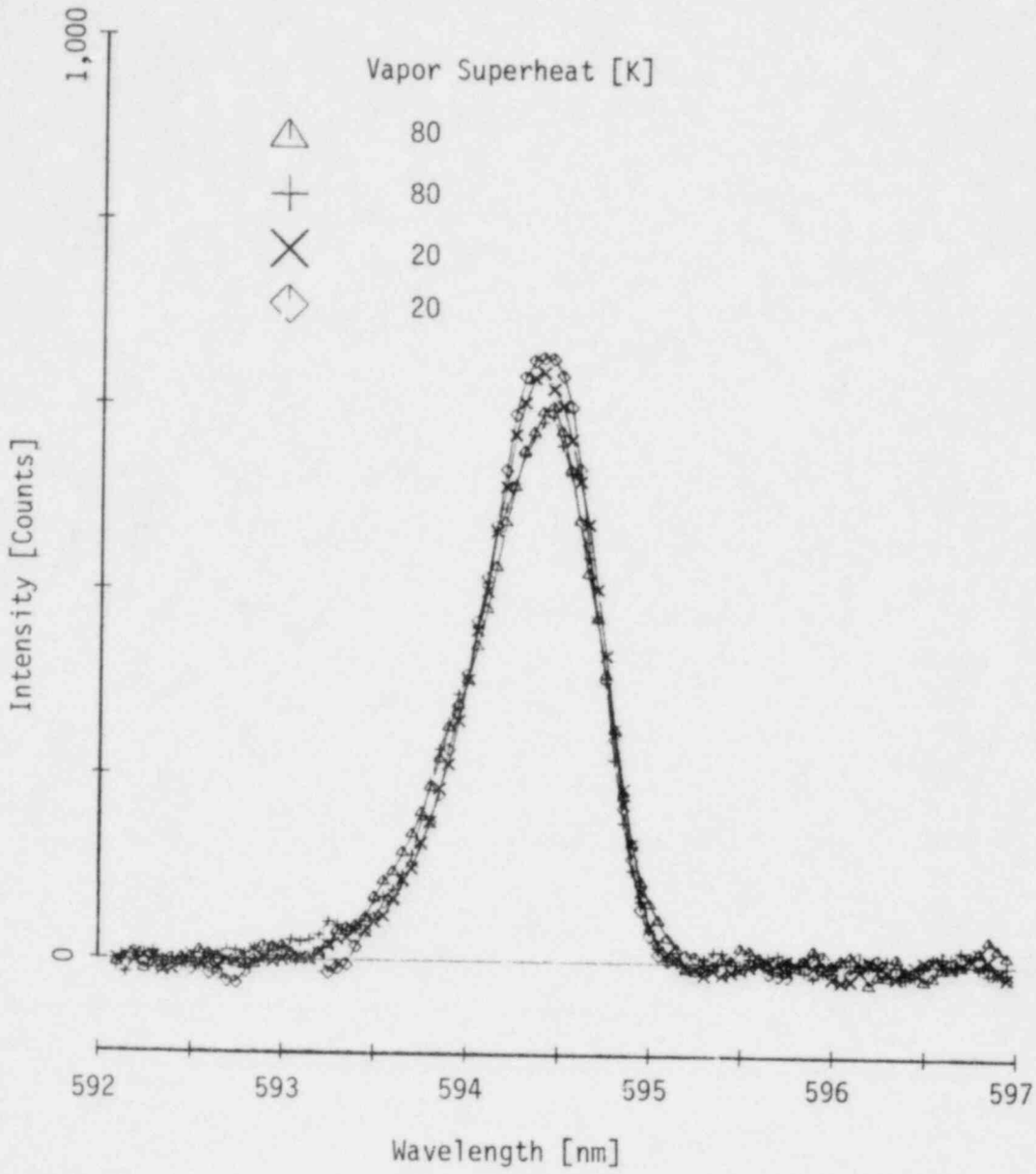

Figure 5.38 Four normalized Raman spectra, steam in non-equilibrium dispersed flow, atmospheric pressure, 20, 80 K superheat

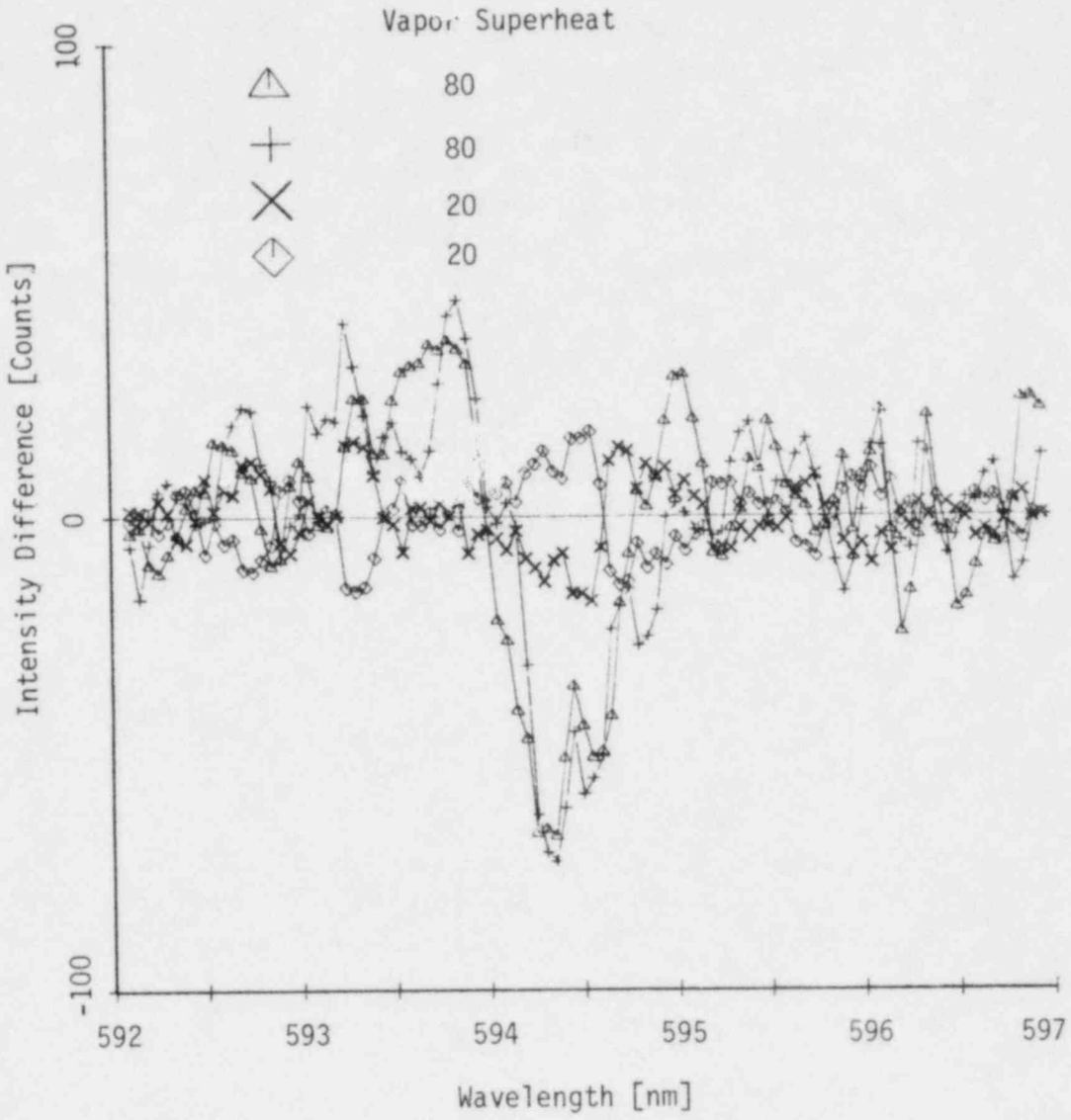

Figure 5.39 Difference between normalized Raman spectra for 20, 80 K nonequilibrium vapor superheat, and mean of two runs at 20 K nonequilibrium vapor superheat

Table 5.5 Integrated intensity ratios for nonequilibrium dispersed two-phase flow and correlation with vapor superheat

Spectrum No.	Vapor Superheat [K] ($T-T_{SAT}$, T_{SAT}=373 K)	R_1
102	80	.736
103	80	.796
104	50	.724
105	50	.713
106	20	.674
107	20	.652

$$R_1 = \left[\int_{592\ nm}^{594.2} I(\lambda)d\lambda/(594.2-592)\right] / \left[\int_{594.2\ nm}^{597} I(\lambda)d\lambda/(597-594.2)\right]$$

Correlation of R_1 with vapor superheat, T,

$R_1 = m \cdot T+b = .00172\ T + .630$

C = .913, correlation coefficient

σ_R = .019, RMS deviation from regression line

$\Delta T = 2\sigma_R/m$ = 22.1 K uncertainty in the vapor superheat correlation

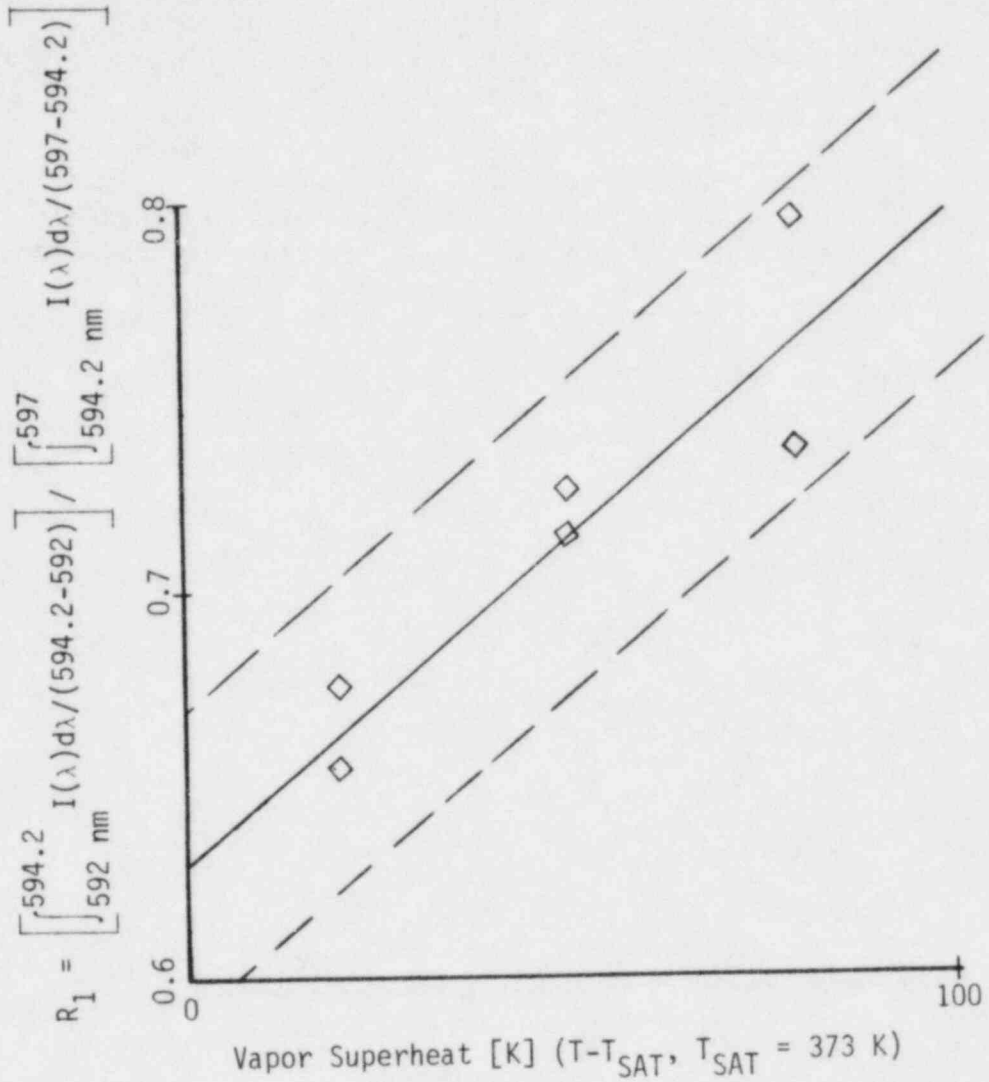

Figure 5.40 Integrated intensity ratios for non-equilibrium dispersed flow as a function of temperature

phase data, using equation (5.11). The estimated uncertainty of Raman scattering temperature measurements in nonequilibrium dispersed flow is ±22 K.

These experiments showed that Raman band contours for steam can be measured in nonequilibrium dispersed two-phase flow. The temperature effects which were seen in earlier single-phase measurements were observed in the presence of liquid droplets. Intensity ratios, calculated from these Raman band contours, were used to estimate the uncertainty of Raman scattering temperature measurements for superheated water vapor in nonequilibrium dispersed two-phase flow.

6. CONCLUSIONS AND RECOMMENDATIONS FOR FURTHER STUDY

A Raman spectroscopy system has been developed which is capable of measuring temperature effects on the Raman vibrational band shape for superheated steam in single and nonequilibrium dispersed two-phase flows. The estimated uncertainty of temperature measurements based on Raman scattering is ±15 K for single-phase samples and ±22 K for dispersed two-phase samples. There are some equipment considerations which limit practical applications of the current system. The following conclusions and recommendations have been drawn from this investigation.

1. Detection and spontaneous Raman scattering from low pressure gases requires careful selection and operation of optical instruments. Considerations of particular importance are,

   i. intensity and frequency of the laser source,
   ii. resolution and stray light rejection of the spectral discrimination instrument,
   iii. collection and transmission efficiency of optical components,
   iv. sensitivity and background noise of the photodetector.

2. The sensitivity of temperature measurements based on Raman scattering is limited by the variation of Raman bands with temperature and the ability to measure these variations accurately. Raman band shapes were measured for superheated single-phase steam at atmospheric pressure and vapor superheats ($T-T_{SAT}$, $T_{SAT} = 373$ K) ranging

from 20 to 190 K. Variations in the band shapes were observed with sufficient accuracy for temperature measurements, with an estimated uncertainty of ±15 K. This level of uncertainty is comparable to that reported by others using Raman scattering for temperature measurements in nitrogen [6.1, 6.2].

3. Mie and Raman scattering, caused by liquid droplets in two-phase samples, complicates observation of Raman spectra for the gas phase. Water droplets cause intense Mie scattering of the incident laser beam, creating a background which is 6 to 9 orders of magnitude more intense than the Raman scattering. Fortunately, this background is spectrally removed from the Raman vibrational bands for nitrogen and water vapor, and can be rejected using a commercially available monochromator.

Raman scattering was observed from atmospheric nitrogen in an air/water mist at an estimated void fraction of 70 to 90 percent. The presence of the liquid droplets reduced the detected Raman intensity by about 30 percent and increased the background by about 12 percent. This approximately doubled the uncertainty of the N_2 Raman band shapes observed in two-phase samples, as compared to single-phase samples. The 3400 cm^{-1} Raman band for the water droplets creates a potential for spectral interference with the 3650 cm^{-1} Raman band for water vapor in nonequilibrium dispersed flow. Experiments using an air/water mist sample showed that for the high void fractions considered here (70 to 90 percent), Raman scattering from the liquid droplets is meas-

urable but does not interfere significantly with the Raman vibrational band for water vapor.

4. Raman vibrational contours were observed for nonequilibrium superheated steam in dispersed two-phase flow at the following conditions,

atmospheric pressure,
20 to 80 K nonequilibrium vapor superheat ($T-T_{SAT}$, $T_{SAT} = 373$ K),
vapor to liquid mass flow ratio, 2.0 ±.5,
equilibrium quality, 62 to 71 percent
estimated void fraction, 70 to 90 percent

The effects of temperature on the Raman band shapes were observed. The estimated uncertainty of temperature measurements based on these band shapes is ±22 K. This is approximately 30 percent worse than the estimated uncertainty of Raman scattering temperature measurements for single-phase steam.

5. Mechanical reproducibility problems associated with alignment of optical components and backlash in the premonochromator create systematic errors which limit the compatability of band shapes or intensity ratios measured from one day to the next. Each day, when the system is realigned or optimized, a new set of calibration runs must be conducted in which Raman band shapes are observed at known reference temperatures. The reference spectra can then be used to develop an intensity ratio correlation for that particular day's experiments. The calibration data take most of a day to run, leaving little time for other experiments. This limits the practical application of the current system.

Specific steps which could be taken to eliminate these problems are listed below.

i. Use kinematic mounts for optical components to reduce or eliminate systematic errors due to misalignment.

ii. Use a fixed bandpass notch filter rather than a premonochromator, which is affected by backlash, to reject the incident laser wavelength.

iii. Develop calibration procedures using a standard reference lamp to correct for systematic errors.

6. Raman scattering is an extremely weak optical process. System improvements which increase the detected intensity will increase the accuracy of proposed temperature measurements. Specific recommendations for system improvements are listed below.

i. Use a better light trapping cell [6.3] to increase the incident intensity in the scattering volume.

ii. Place a parabolic reflector behind the scattering volume to approximately double the solid angle of the collection optics.

iii. Use a more powerful laser to increase the incident intensity.

7. The long time period required to obtain a single Raman spectrum using the present system limits its applicability to steady conditions. In real situations, it is difficult to maintain steady multiphase conditions for such a long time. For practical

applications, the speed of the Raman measurement should be increased by a factor of 10 to 100. This could be accomplished by using an optical multichannel detector. These detectors allow simultaneous observation of the complete spectral region of interest rather than dividing it into segments and observing one interval at a time. A 100 channel optical array with half the sensitivity of the current PMT could reduce the data acquisition time by a factor of 50.

8. The measurements described in this investigation were conducted in an unenclosed sample. Practical application of Raman techniques for temperature measurements in multiphase flow will require that enclosed test sections be used. Problems to be encountered with enclosed test sections are,

i. Limited optical access

ii. Attenuation and scattering of the incident laser beam by windows

iii. Attenuation and dispersion of Raman scattered light by windows

Optical ports for a multiphase test section will require careful design to avoid quenching and condensation on windows. The flow system should be designed to minimize contamination of windows by mineral deposits and scale.

There are some advantages to using an enclosed test section. These are listed below.

i. Experiments can be conducted at higher pressures to increase the density of the sample and thus the scattered intensities.

ii. Experimental conditions can be more precisely controlled in an enclosed test section.

In this investigation, which used an unenclosed sample, temperature variations across the measurement volume may have a significant effect on the measured Raman band shapes. In an enclosed sample, turbulent mixing can be controlled by adjusting the flow rate to achieve a more uniform sample temperature.

9. In this investigation, Raman observations of nonequilibrium two-phase flow were correlated with the sample temperature using aspirated thermocouple data. While for single-phase samples, thermocouple measurements are considered to be reliable, there is a large uncertainty in the two-phase nonequilibrium superheat temperatures. Future studies should concentrate on correlating Raman band shapes for two-phase samples to those of single-phase reference samples in which the temperature can be measured accurately using conventional thermocouples.

10. The spectral discrimination system used in this investigation could not resolve the details of the Raman vibrational bands but measured only smoothed contours. Resolution capability of .1 to .15 nm is required to resolve the details of the 3650 cm^{-1} Raman band for water vapor. Better spectral resolution may

yield improved temperature sensitivity by allowing further optimization of the spectral bands used to calculate intensity ratios.

REFERENCES

Chapter 1

1.1 Nijhawan, S., et al., "Measurement of Vapor Superheat in Post-Critical-Heat-Flux-Boiling," Journal of Heat Transfer, Vol. 102, No. 3, Aug. 1980, pp. 465-470.

1.2 Lapp, M., Penney, C. M., "Introduction," Laser Raman Gas Diagnostics, Lapp, M. and Penney, C. M., ed., Plenum, New York, 1974, pp. xi-xiv.

1.3 Lapp, M., "Flame Temperatures From Vibrational Raman Scattering," Laser Raman Gas Diagnostics, Lapp, M. and Penney, C. M., ed., Plenum, New York, 1974, pp. 107-145.

1.4 Salzman, J. A., Masica, W. J. and Coney, T. A., "Determination of Gas Temperatures From Laser Raman Scattering," NASA TN D-6336, May 1961.

1.5 Bribes, J. L., et al., "Raman Band Contours for Water Vapor as a Function of Temperature," App. Phys. Let., Vol. 28, No. 6, Mar. 1976, pp. 336, 337.

Chapter 2

2.1 Raman, C. V., "A New Radiation," Proceedings of the Indian Academy of Sciences, Vol. 37, 1953, p. 333.

2.2 Brandmuller, J. and Kiefer, W., "Physicists View Fifty Years of Raman Spectroscopy," The Spex Speaker, Issue 4, Dec. 1978, pp. 3-9.

2.3 Lapp, M. and Penney, C. M., "Introduction," Laser Raman Gas Diagnostics, Lapp, M. and Penney, C. M., ed., Plenum, New York, 1974, pp. xi-xiv.

2.4 Penney, C. M., "Light Scattering and Flouresence in the Approach to Ressonance," Laser Raman Gas Diagnostics, Lapp, M. and Penney, C. M., ed., Plenum, New York, 1974, pp. 191-217.

2.5 Regnier, P. R. and Taran, J. P. E., "Gas Concentration Measurement by Coherent Anti-Stokes Raman Scattering," Laser Raman Gas Diagnostics, Lapp, M. and Penney, C. M., ed., Plenum, New York, 1974, pp. 87-103.

2.6 Lapp, M. and Penney, C. M., "Analysis of Rayleigh and Raman Scattered Radiation," Methods of Experimental Physics, Vol. 18, Part B, Fluid Dynamics, Emrich, R. J., ed., Academic Press, New York, 1981, p. 14.

2.7 Tippler, P. A., Modern Physics, Worth, New York, 1978, pp. 304, 305.

2.8 Salzman, J. A., Masica, W. J. and Coney, T. A., "Determination of Gas Temperatures From Laser Raman Scattering," NASA TN D-6336, May 1971, pp. 3, 4.

2.9 Pan, Y., Faw, R. E. and Lester, T. W., Laser Raman Remote Temperature Sensing in Liquids, Kansas Engineering Experiment Station Special Report 133, Kansas State University, Manhattan, Kansas, Mar. 1980, pp. 4-6.

2.10 Lapp, M., "Flame Temperatures From Vibrational Raman Scattering," Laser Raman Gas Diagnostics, Lapp, M. and Penney, C. M., ed., Plenum, New York, 1974, p. 109.

2.11 Ibid., pp. 109-116.

2.12 Ibid., pp. 111, 112.

2.13 Lapp, M., Penney, C. M. and Asher, J. A., "Application of Light Scattering Techniques for Measurements of Density, Temperature, and Velocity in Gasdynamics," Aerospace Research Laboratories, No. 73-0045, April 1973, p. 34.

2.14 Ibid., p. 37.

2.15 Lapp, M., "Flame Temperatures From Vibrational Raman Scattering," Laser Raman Gas Diagnostics, Lapp, M. and Penney, C. M., ed., Plenum, New York, 1974, pp. 119-123.

2.16 Ibid., pp. 123-130.

2.17 Salzman, J. A., Masica, W. J. and Coney, T. A., "Determination of Gas Temperatures From Laser Raman Scattering," NASA TN D-6336, May 1971.

2.18 Lapp, M., Penney, C. M. and Asher, J. A., "Application of Light Scattering Techniques for Measurements of Density, Temperature, and Velocity in Gasdynamics," Aerospace Research Laboratories, No. 73-0045, April 1973, pp. 35-47.

2.19 Pan, Y., Faw, R. E. and Lester, T. W., Laser Raman Remote Temperature Sensing in Liquids, Kansas Engineering Experiment Station Special Report 133, Kansas State University, Manhattan, Kansas, Mar. 1980, p. 10.

2.20 Lapp, M., "Flame Temperatures From Vibrational Raman Scattering," Laser Raman Gas Diagnostics, Lapp, M. and Penney, C. M., ed., Plenum, New York, 1974, p. 113.

2.21 Ibid., pp. 134, 135.

2.22 Salzman, J. A., Masica, W. J. and Coney, T. A., "Determination of Gas Temperatures From Laser Raman Scattering," NASA TN D-6336, May 1971.

2.23 Pan, Y., Faw, R. E. and Lester, T. W., Laser Raman Remote Temperature Sensing in Liquids, Kansas Engineering Experiment Station Special Report 133, Kansas State University, Manhattan, Kansas, Mar. 1980.

2.24 Lapp, M., "Raman Scattering Probe for Water Vapor in Flames," AIAA Paper No. 74-1143, Oct. 1974.

2.25 Lapp, M., "Raman Scattering From Water Vapor in Flames," AIAA Journal, Vol. 15, No. 12, Dec. 1977, pp. 1665-1666.

2.26 Penney, C. M. and Lapp, M., "Raman Scattering Cross Sections for Water Vapor," J. Opt. Soc. Am., Vol. 66, No. 5, May 1976, pp. 422-425.

2.27 Bribes, J. L., et al., "Raman Band Contours for Water Vapor as a Function of Temperature," Appl. Phys. Let., Vol. 28, No. 6, Mar. 1976, pp. 336-337.

2.28 Bribes, J. L., et al., "Detailed Study of the Q-Branch Profile of the ν_1 of Water Molecule from 293 to 1500 K," Proc. Fifth Int. Conf. Raman Spectroscopy, Schmid, E. D., ed., University Freiburg, Sept. 1976, pp. 414-415.

2.29 Pan, Y., Faw, R. E. and Lester, T. W., Laser Raman Remote Temperature Sensing in Liquids, Kansas Engineering Experiment Station Special Report 133, Kansas State University, Manhattan, Kansas, Mar. 1980, p. 147.

2.30 Bribes, J. L., et al., "Raman Band Contours for Water Vapor as a Function of Temperature," Appl. Phys. Let., Vol. 28, No. 6, Mar. 1976, p. 337.

2.31 Lapp, M. and Penney, C. M., "Analysis of Rayleigh and Raman Scattered Radiation," Methods of Experimental Physics, Vol. 18, Part B, Fluid Dynamics, Emrich, R. J., ed., Academic Press, New York, 1981, p. 16.

2.32 Penney, C. M. and Lapp, M., "Raman Scattering Cross Sections for Water Vapor," J. Opt. Soc. Am., Vol. 66, No. 5, May 1976, pp. 424, 425.

2.33 Grumpret, R. D. and Sliepevich, C. M., "Table of Light Scattering Functions for Spherical Particles," Engineering Research Inst., University of Michigan, 1951.

Chapter 3

3.1 Spectra Physics Instruction Manual 164-09/265, Spectra Physics, Inc., 366 South Randolphville Road, Piscataway, NY 08854.

3.2 ISA DL-203 Instruction Manual, Instruments SA, Inc., 173 Essex Ave., Metuchen, NJ 08840.

3.3 Instruction Manual for TN-1705 and TN-1706 Pulse Height Analyzers, Tracor Northern, Inc., 2551 West Beltine Highway, Middleton, WI 53562, p. 6.

3.4 Ibid., p. 12.

3.5 Morton, G. A., Smith, H. M. and Krall, H. R., "The Performance of High Gain First Dynode Photomultipliers," 15th IEEE Nuclear Science Symposium, Publication No. ST-3881, Montreal, Canada, 1968.

3.6 RCA 8850 Photodetector Specifications, RCA, Electro Optics and Devices, Solid State Division, New Holland Ave., Lancaster, Pa. 17604.

3.7 Ibid.

3.8 Nijhawan, S., et al., "Measurement of Vapor Superheat in Post-Critical-Heat-Flux-Boiling," Journal of Heat Transfer, Vol. 102, No. 3, Aug. 1980, pp. 465-470.

Chapter 4

4.1 Hill, R. A. and Hartley, D. L., "Raman Scattering with High Grain Multiple-Pass Cells," Laser Raman Gas Diagnostics, Lapp, N. and Penney, C. M., ed., Plenum, NY, 1974, pp. 315-329.

4.2 RCA 8850 Photodetector Specifications, RCA, Electro Optics and Devices, Solid State Division, New Holland Ave., Lancaster, Pa. 17604.

4.3 Morton, G. A., Smith, H. M. and Krall, H. R., "The Performance of High Gain First Dynode Photomultipliers," 15th IEEE Nuclear Science Symposium, Publication No. ST-3881, Montreal, Canada, 1968.

4.4 Pan, Y., Faw, R. E. and Lester, T. W., Laser Raman Remote Temperature Sensing in Liquids, Kansas Engineering Experiment Station Special Report 133, Kansas State University, Manhattan, Kansas, Mar. 1980.

4.5 Lapp, M., "Flame Temperature Measurements From Vibrational Raman Scattering," Laser Raman Gas Diagnostics, Lapp, M. and Penney, C. M., ed., Plenum, NY, 1974, pp. 107-145.

4.6 Bribes, J. L., et al., "Raman Band Contours for Water Vapor as a Function of Temperature," Appl. Phys. Let., Vol. 28, Mar. 1976, pp. 336, 337.

Chapter 5

5.1 Walrafen, G. E., "Raman Spectral Studies of Water Structure," J. of Chemical Physics, Vol. 40, No. 1, June 1964, pp. 3249-3256.

5.2 Pan, Y., Faw, R. E. and Lester, T. W., Laser Raman Remote Temperature Sensing in Liquids, Kansas Engineering Experiment Station Special Report 133, Kansas State University, Manhattan, Kansas, Mar. 1980.

5.3 Lapp, M., "Flame Temperature From Vibrational Raman Scattering," Laser Raman Gas Diagnostics, Lapp, M. and Penney, C. M., ed., Plenum, New York, 1974, p. 118.

5.4 Lenoard, D., "Measurement of Aircraft Turbine Exhaust Emissions," Laser Raman Gas Diagnostics, Lapp, M. and Penney, C. M., ed., Plenum, New York, 1974, p. 45.

5.5 Lapp, M., "Flame Temperatures From Vibrational Raman Scattering," Laser Raman Gas Diagnostics, Lapp, M. and Penney, C. M., ed., Plenum, New York, pp. 140, 141.

5.6 Schildkraut, E., "Electronic Signal Processing for Raman Scattering Measurements," Laser Raman Gas Diagnostics, Lapp, M. and Penney, C. M., ed., Plenum, New York, 1974, pp. 259-277.

5.7 Lapp, M., "Flame Temperatures From Vibrational Raman Scattering," Laser Raman Gas Diagnostics, Lapp, M. and Penney, C. M., ed., Plenum, New York, 1974, pp. 133, 134.

5.8 Bribes, J. L., et al., "Raman Band Contours for Water Vapor as a Function of Temperature," Appl. Phys. Let., Vol. 28, Mar. 1976, pp. 336, 337.

5.9 Salzman, J. A., Masica, W. J. and Coney, T. A., "Determination of Gas Temperatures From Laser Raman Scattering," NASA TN D-6336, May 1971, pp. 7, 8.

Chapter 6

6.1 Lapp, M., "Flame Temperatures From Vibrational Raman Scattering," Laser Raman Gas Diagnostics, Lapp, M. and Penney, C. M., ed., Plenum, New York, 1974, pp. 134, 135.

6.2 Salzman, J. A., Masica, W. J. and Coney, T. A., "Determination of Gas Temperatures From Laser Raman Scattering," NASA TN D-6336, May 1971, p. 15.

6.3 Hill, R. A. and Hartley, D. L., "Raman Scattering With High Gain Multiple-Pass Cells," Laser Raman Gas Diagnostics, Lapp, N. and Penney, C. M., ed., Plenum, New York, 1974, pp. 315-329.

APPENDIX

A.1 Calculation of Pulse Height for Single Photon Peak

The calculations described below were used to estimate the channel numbers in which the single photon peak should fall for the system gain used to acquire the pulse height distribution shown in Figure 4.9.

The photomultiplier tube generates a charge pulse, Q, which is proportional to the light energy, E, of the detected photon

$$Q = SE \tag{A.1}$$

where S is the sensitivity of the PMT.

The MCA charge sensitive preamplifier produces a voltage signal, V, which is proportional to the input charge

$$V = gQ \tag{A.2}$$

where g is the MCA charge amplifier gain.

The MCA stores the voltage pulse in the channel corresponding to the voltage, V. The channel number, N, is determined by the conversion gain, c.

$$N = cV \tag{A.3}$$

The energy of the incident photon is given by Plancks Law.

$$E = hc/\lambda \tag{A.4}$$

The peak output for the LED is at 560 n/m.

$$E = \frac{.622 \times 10^{-33}[J \cdot S]3 \times 10^{8}[m/s]}{560 \times 10^{-9}\ [m]} \qquad (A.5)$$

$$E = 3.33 \times 10^{-19}\ [J] \qquad (A.6)$$

Values for the PMT sensitivity, S, were obtained from the RCA 8850 PMT specifications.

	Sensitivity [A/W]
typical	1.48×10^{6}
minimum	1.48×10^{5}
maximum	6.84×10^{6}

The MCA preamplifier gain, g, is adjustable from .165 to 3.3 volts per picocoulomb, and the minimum value was used for the pulse height distribution of Figure 4.9. The conversion gain, g, of the MCA A to D converter is 64 channels per volt. Inserting these values into equations (A.1) through (A.3) indicates that the single photon peak should fall between channels 1 and 24.

A.2 Sample Data Listings

The following pages contain sample data from the computer programs RAMDOC and RAMCOM, which were used to document and compare Raman spectra.

RAMDOC was used for documentation of raw data. The output begins with a heading that gives some of the details of the

experiment (p. A-4). The intensity or number of counts in each wavelength interval is listed as a function of channel number, wavelength, and wave number shift (pp. A-5, A-6).

RAMCOM was used to make comparisons of Raman spectra. The listing begins with some spectral parameters similar to those listed by RAMDOC (p. A-7). The average background offset (noise), the integrated Raman signal and the spectrum normalization or scale factor are listed for each run (p. A-7). Intensity ratios, calculated for λ_D = 594.0 to 594.4 nm, in 0.1 nm increments, are also listed for each run. The main body of the listing includes the raw data (pp. A-8, A-9), the three point averaged, smoothed data (pp. A-10, A-11), the normalized data, incldуing the mean normalized spectrum, (pp. A-12, A-13) and the difference between each normalized spectrum and the mean spectrum (pp. A-14, A-15).

SPECTRUM NO. 81. DATE 3 9 82

STEAM AT 153.0 DEG. C

WAVELENGTH RANGE 5920.0 TO 5970.0 ANGSTROMS

WAVENUMBER SHIFT -3601.3 TO -3741.4 1/CM

NO. OF CHANNELS 100 TIME PER CHANNEL 45.0 SEC

CH NO	WAV LEN	WAV NUM	COUNTS
1.	5920.5	-3601.	1682.
2.	5921.0	-3603.	1685.
3.	5921.5	-3604.	1701.
4.	5922.0	-3606.	1735.
5.	5922.5	-3607.	1731.
6.	5923.0	-3608.	1643.
7.	5923.5	-3610.	1718.
8.	5924.0	-3611.	1748.
9.	5924.5	-3613.	1731.
10.	5925.0	-3614.	1693.
11.	5925.5	-3616.	1647.
12.	5926.0	-3617.	1696.
13.	5926.5	-3618.	1672.
14.	5927.0	-3620.	1689.
15.	5927.5	-3621.	1752.
16.	5928.0	-3623.	1796.
17.	5928.5	-3624.	1762.
18.	5929.0	-3626.	1675.
19.	5929.5	-3627.	1742.
20.	5930.0	-3628.	1760.
21.	5930.5	-3630.	1671.
22.	5931.0	-3631.	1719.
23.	5931.5	-3633.	1784.
24.	5932.0	-3634.	1815.
25.	5932.5	-3636.	1819.
26.	5933.0	-3637.	1796.
27.	5933.5	-3638.	1896.
28.	5934.0	-3640.	1827.
29.	5934.5	-3641.	1799.
30.	5935.0	-3643.	1884.
31.	5935.5	-3644.	1844.
32.	5936.0	-3645.	1983.
33.	5936.5	-3647.	2047.
34.	5937.0	-3648.	2181.
35.	5937.5	-3650.	2322.
36.	5938.0	-3651.	2362.
37.	5938.5	-3653.	2445.
38.	5939.0	-3654.	2546.
39.	5939.5	-3655.	2704.
40.	5940.0	-3657.	2810.
41.	5940.5	-3658.	3171.
42.	5941.0	-3660.	3315.
43.	5941.5	-3661.	3699.
44.	5942.0	-3662.	3904.
45.	5942.5	-3664.	4181.
46.	5943.0	-3665.	4489.
47.	5943.5	-3667.	4731.
48.	5944.0	-3668.	4840.
49.	5944.5	-3670.	4748.
50.	5945.0	-3671.	4680.

CH NO	WAV LEN	WAV NUM	COUNTS
51.	5945.5	-3672.	4263.
52.	5946.0	-3674.	4075.
53.	5946.5	-3675.	3661.
54.	5947.0	-3677.	3495.
55.	5947.5	-3678.	2993.
56.	5948.0	-3679.	2856.
57.	5948.5	-3681.	2666.
58.	5949.0	-3682.	2343.
59.	5949.5	-3684.	2096.
60.	5950.0	-3685.	1964.
61.	5950.5	-3686.	1917.
62.	5951.0	-3688.	1759.
63.	5951.5	-3689.	1825.
64.	5952.0	-3691.	1782.
65.	5952.5	-3692.	1822.
66.	5953.0	-3694.	1812.
67.	5953.5	-3695.	1776.
68.	5954.0	-3696.	1671.
69.	5954.5	-3698.	1770.
70.	5955.0	-3699.	1660.
71.	5955.5	-3701.	1779.
72.	5956.0	-3702.	1762.
73.	5956.5	-3703.	1714.
74.	5957.0	-3705.	1696.
75.	5957.5	-3706.	1727.
76.	5958.0	-3708.	1788.
77.	5958.5	-3709.	1679.
78.	5959.0	-3710.	1686.
79.	5959.5	-3712.	1726.
80.	5960.0	-3713.	1799.
81.	5960.5	-3715.	1755.
82.	5961.0	-3716.	1692.
83.	5961.5	-3718.	1706.
84.	5962.0	-3719.	1711.
85.	5962.5	-3720.	1779.
86.	5963.0	-3722.	1742.
87.	5963.5	-3723.	1770.
88.	5964.0	-3725.	1722.
89.	5964.5	-3726.	1828.
90.	5965.0	-3727.	1660.
91.	5965.5	-3729.	1729.
92.	5966.0	-3730.	1725.
93.	5966.5	-3732.	1824.
94.	5967.0	-3733.	1721.
95.	5967.5	-3734.	1769.
96.	5968.0	-3736.	1673.
97.	5968.5	-3737.	1698.
98.	5969.0	-3739.	1669.
99.	5969.5	-3740.	1749.
100.	5970.0	-3741.	1681.

SPEC. NO.	DATE	MEDIUM	TEMP. (C)	TIME/CH. (SEC)
81.	3 9 82	STEAM	153.	45.
82.	2 9 82	STEAM	153.	45.
89.	3 9 82	STEAM	353.	45.
90.	3 9 82	STEAM	353.	45.

SP. NO.	NOISE	SIGNAL	SCALE FACTOR
81.	1714.9	45968.	.2175
82.	1608.8	45222.	.2211
89.	2002.9	28249.	.3540
90.	1930.8	28451.	.3515

SP. NO.	INTENSITY RATIOS				
81.	.227	.353	.576	.961	1.652
82.	.227	.353	.568	.948	1.593
89.	.482	.704	1.075	1.712	2.854
90.	.502	.720	1.068	1.660	2.742

INPUT DATA

CH. NO.	81.	82.	89.	90.
1.	1582.	1543.	2012.	1922.
2.	1685.	1626.	1999.	1950.
3.	1701.	1636.	2002.	1885.
4.	1735.	1545.	1988.	2004.
5.	1731.	1650.	1945.	1978.
6.	1643.	1610.	2068.	1862.
7.	1718.	1580.	2016.	1961.
8.	1743.	1497.	1964.	1991.
9.	1731.	1600.	2078.	1899.
10.	1633.	1609.	2030.	1983.
11.	1647.	1664.	2114.	1826.
12.	1696.	1635.	2003.	1946.
13.	1672.	1683.	1909.	1932.
14.	1689.	1647.	2045.	1970.
15.	1752.	1630.	2021.	1913.
16.	1796.	1709.	2061.	1930.
17.	1762.	1601.	2080.	1884.
18.	1675.	1561.	2081.	1951.
19.	1742.	1595.	1957.	2056.
20.	1760.	1610.	2045.	2031.
21.	1671.	1707.	2105.	2031.
22.	1718.	1637.	2059.	2035.
23.	1784.	1677.	2107.	2087.
24.	1815.	1677.	2154.	2052.
25.	1919.	1646.	2159.	2020.
26.	1796.	1630.	2166.	2124.
27.	1896.	1747.	2266.	2195.
28.	1827.	1739.	2279.	2089.
29.	1799.	1818.	2271.	2206.
30.	1884.	1751.	2263.	2253.
31.	1844.	1786.	2253.	2236.
32.	1983.	1895.	2384.	2344.
33.	2047.	1946.	2424.	2455.
34.	2181.	1890.	2491.	2457.
35.	2322.	2096.	2486.	2485.
36.	2362.	2147.	2680.	2571.
37.	2445.	2299.	2806.	2659.
38.	2546.	2480.	2835.	2785.
39.	2704.	2534.	2793.	2851.
40.	2810.	2768.	2996.	2857.
41.	3171.	2989.	2949.	2990.
42.	3315.	3195.	3122.	3094.
43.	3689.	3446.	3435.	3187.
44.	3904.	3729.	3414.	3253.
45.	4181.	4074.	3544.	3413.
46.	4499.	4386.	3564.	3398.
47.	4731.	4524.	3706.	3509.
48.	4840.	4646.	3519.	3525.
49.	4748.	4461.	3524.	3499.
50.	4690.	4399.	3489.	3299.

INPUT DATA

CH. NO.	81.	82.	89.	90.
51.	4263.	4359.	3201.	3153.
52.	4075.	3858.	3028.	2949.
53.	3661.	3568.	2890.	2732.
54.	3486.	3246.	2780.	2556.
55.	2993.	3009.	2714.	2601.
56.	2856.	2690.	2549.	2438.
57.	2666.	2431.	2296.	2231.
58.	2343.	2293.	2193.	2149.
59.	2096.	2050.	2157.	2174.
60.	1964.	1905.	2165.	2090.
61.	1917.	1795.	2078.	2036.
62.	1759.	1683.	2079.	1981.
63.	1825.	1713.	1985.	1918.
64.	1732.	1664.	2054.	1958.
65.	1822.	1745.	2049.	1951.
66.	1812.	1667.	2057.	1985.
67.	1776.	1620.	1994.	1923.
68.	1671.	1725.	2025.	1935.
69.	1770.	1650.	2009.	1949.
70.	1660.	1659.	1940.	1922.
71.	1778.	1696.	1976.	1846.
72.	1762.	1630.	1965.	1937.
73.	1714.	1654.	2080.	1976.
74.	1695.	1655.	2054.	1965.
75.	1727.	1642.	1972.	1951.
76.	1733.	1639.	1935.	1940.
77.	1679.	1621.	1932.	1852.
78.	1686.	1692.	2039.	1910.
79.	1725.	1679.	1980.	1958.
80.	1799.	1589.	2009.	1986.
81.	1755.	1595.	1953.	1888.
82.	1692.	1591.	1854.	1959.
83.	1706.	1619.	1992.	2008.
84.	1711.	1636.	1967.	1956.
85.	1773.	1601.	1969.	1997.
86.	1742.	1602.	2037.	1894.
87.	1770.	1607.	2042.	1974.
88.	1722.	1607.	2053.	1940.
89.	1823.	1662.	1941.	1858.
90.	1660.	1581.	1924.	1941.
91.	1729.	1683.	1998.	1926.
92.	1725.	1612.	1949.	1911.
93.	1524.	1611.	1973.	1971.
94.	1721.	1685.	1992.	2006.
95.	1769.	1578.	1989.	1931.
96.	1573.	1654.	2049.	1924.
97.	1698.	1603.	1932.	1953.
98.	1669.	1589.	2023.	1950.
99.	1743.	1569.	2038.	1955.
100.	1681.	1672.	2061.	1944.

SMOOTHED DATA

CH. NO.	81.	82.	89.	90.
2.	1689.3	1591.7	2004.3	1919.0
3.	1707.0	1592.3	1996.3	1946.3
4.	1722.3	1600.3	1978.3	1955.7
5.	1703.0	1601.7	2000.3	1948.0
6.	1697.3	1613.3	2009.7	1933.7
7.	1703.0	1562.3	2016.0	1901.3
8.	1732.3	1559.0	2019.3	1913.7
9.	1724.0	1568.7	2024.0	1921.0
10.	1690.3	1624.3	2074.0	1902.7
11.	1673.7	1636.0	2049.0	1918.3
12.	1671.7	1660.7	2009.7	1901.3
13.	1685.7	1655.0	1985.7	1949.3
14.	1704.3	1653.3	1991.7	1938.3
15.	1745.7	1662.0	2042.3	1937.7
16.	1771.0	1646.7	2054.0	1909.0
17.	1744.3	1623.7	2074.0	1925.0
18.	1726.3	1585.7	2039.3	1967.0
19.	1725.7	1588.7	2027.7	2016.0
20.	1724.3	1637.3	2035.7	2039.3
21.	1715.3	1651.3	2069.7	2032.3
22.	1724.3	1673.7	2090.3	2051.0
23.	1772.3	1663.7	2106.7	2061.3
24.	1806.0	1666.7	2140.0	2056.3
25.	1810.0	1651.0	2159.7	2058.7
26.	1837.0	1674.3	2197.0	2113.0
27.	1839.7	1705.3	2237.0	2136.0
28.	1840.7	1768.0	2272.0	2153.3
29.	1836.7	1769.3	2271.0	2182.7
30.	1842.3	1785.0	2262.3	2231.7
31.	1903.7	1810.7	2300.0	2277.7
32.	1958.0	1875.7	2353.7	2345.0
33.	2070.3	1910.3	2433.0	2418.7
34.	2183.3	1977.3	2467.0	2465.7
35.	2288.3	2044.3	2552.3	2504.3
36.	2376.3	2180.7	2657.3	2575.0
37.	2451.0	2309.7	2773.7	2675.0
38.	2565.0	2437.7	2811.3	2771.7
39.	2686.7	2594.0	2874.7	2834.3
40.	2895.0	2763.7	2912.7	2902.7
41.	3093.7	2990.7	3022.3	2990.3
42.	3391.7	3206.7	3168.7	3090.3
43.	3630.0	3453.3	3323.7	3178.0
44.	3924.7	3749.7	3464.3	3284.3
45.	4191.3	4063.0	3507.3	3354.7
46.	4467.0	4328.0	3604.7	3440.0
47.	4686.7	4518.7	3596.3	3477.3
48.	4773.0	4543.7	3583.0	3511.0
49.	4756.0	4502.0	3510.7	3440.7
50.	4563.7	4406.3	3404.7	3320.0

SMOOTHED DATA

CH. NO.	81.	82.	89.	90.
51.	4339.3	4205.3	3239.3	3136.7
52.	3999.7	3928.3	3039.7	2948.0
53.	3741.3	3557.3	2899.3	2745.7
54.	3379.7	3274.0	2794.7	2629.7
55.	3111.3	2981.3	2681.0	2531.7
56.	2833.3	2709.7	2519.7	2423.3
57.	2621.7	2471.3	2347.7	2272.7
58.	2368.3	2259.0	2217.0	2134.7
59.	2134.3	2082.7	2173.3	2137.7
60.	1992.3	1916.7	2133.3	2100.0
61.	1880.0	1794.3	2107.3	2035.7
62.	1833.7	1730.3	2047.3	1979.3
63.	1788.7	1686.7	2039.3	1952.3
64.	1809.7	1707.3	2029.3	1945.7
65.	1805.3	1692.0	2053.3	1958.0
66.	1803.3	1677.3	2033.3	1956.3
67.	1753.0	1670.7	2025.3	1947.7
68.	1739.0	1665.0	2009.3	1935.7
69.	1706.3	1678.0	1991.3	1935.3
70.	1736.0	1668.3	1975.0	1905.7
71.	1733.3	1661.7	1960.3	1901.7
72.	1751.3	1660.0	2007.0	1919.7
73.	1724.0	1646.3	2033.0	1959.3
74.	1712.3	1650.3	2035.3	1954.0
75.	1737.0	1645.3	1997.0	1952.0
76.	1731.3	1634.0	1946.3	1914.3
77.	1717.7	1650.7	1968.7	1900.7
78.	1697.0	1664.0	1983.7	1910.0
79.	1737.0	1653.3	2009.3	1954.7
80.	1760.0	1621.0	1980.7	1947.3
81.	1743.7	1591.7	1938.7	1944.3
82.	1717.7	1601.7	1933.0	1951.7
83.	1703.0	1615.3	1937.7	1974.3
84.	1732.0	1618.7	1976.0	1987.0
85.	1744.0	1613.0	1991.0	1949.0
86.	1763.7	1603.3	2016.0	1955.0
87.	1744.7	1605.3	2044.0	1936.0
88.	1773.3	1625.3	2012.0	1924.0
89.	1736.7	1616.7	1972.7	1913.0
90.	1739.0	1642.0	1954.3	1908.3
91.	1704.7	1625.3	1957.0	1926.0
92.	1753.3	1635.3	1973.3	1936.0
93.	1756.7	1636.0	1971.3	1962.7
94.	1771.3	1624.7	1984.7	1959.3
95.	1721.0	1639.0	2010.0	1953.7
96.	1713.3	1611.7	1990.0	1906.0
97.	1680.0	1615.3	2003.3	1915.7
98.	1705.3	1587.0	1999.7	1926.0
99.	1693.7	1610.0	2042.7	1953.0

SMOOTHED, NORMALIZED SPECTRA

CH. NO.	81.	82.	89.	90.	
2.	-5.6	-3.8	.5	-4.2	-4.7
3.	-1.7	-3.6	-2.3	5.5	-2.7
4.	1.6	-1.9	-8.7	8.7	-.1
5.	-2.6	-1.6	-.9	6.0	-2.1
6.	-3.8	1.0	2.4	1.0	-1.4
7.	-2.6	-10.3	4.6	-10.4	-6.4
8.	3.8	-11.0	5.8	-6.0	-3.6
9.	2.0	-8.9	7.5	-3.5	-3.4
10.	-5.3	3.4	25.2	-9.9	-1.0
11.	-7.9	6.0	16.3	-4.4	-.9
12.	-9.4	11.5	2.0	-10.4	1.0
13.	-6.4	10.2	-6.1	6.5	1.9
14.	-2.3	9.3	-4.0	2.6	3.3
15.	6.7	11.8	14.0	2.4	9.2
16.	12.0	8.4	18.1	-7.7	10.2
17.	6.4	3.3	25.2	-2.0	4.8
18.	2.5	-5.1	12.9	12.7	-1.3
19.	2.3	-4.5	8.8	29.9	-1.1
20.	2.1	6.3	11.6	38.1	4.2
21.	.3	9.4	23.6	35.7	4.9
22.	2.1	14.3	31.0	42.2	8.2
23.	12.5	12.1	36.7	45.9	12.3
24.	13.8	12.8	48.5	44.1	16.3
25.	20.7	9.3	55.5	48.5	15.0
26.	26.6	14.5	68.7	64.0	20.5
27.	27.1	21.3	82.9	72.1	24.2
28.	27.4	35.2	95.3	81.7	31.3
29.	26.5	35.5	94.9	88.5	31.0
30.	27.7	39.0	91.8	105.7	33.3
31.	41.1	44.6	105.2	121.9	42.9
32.	52.9	59.0	124.2	145.6	56.0
33.	77.3	66.7	152.3	171.5	72.0
34.	101.9	81.5	164.3	188.0	91.7
35.	124.8	96.3	194.5	201.6	110.5
36.	143.9	126.5	231.7	226.4	135.2
37.	160.1	154.8	272.8	251.6	157.4
38.	184.9	183.3	286.2	295.5	184.1
39.	211.4	217.3	309.6	317.6	214.6
40.	253.7	255.4	322.1	341.6	256.1
41.	301.0	303.4	360.9	368.9	302.2
42.	364.8	353.3	412.7	407.5	359.1
43.	417.9	407.9	467.5	439.4	412.9
44.	480.7	473.4	517.3	475.7	477.1
45.	538.7	542.7	532.6	500.5	540.7
46.	598.7	601.3	567.0	530.5	600.0
47.	646.5	643.5	564.1	543.6	645.0
48.	665.3	649.0	559.3	555.4	657.1
49.	661.6	639.8	533.7	530.7	650.7
50.	619.7	618.6	496.2	488.3	619.2

SMOOTHED, NORMALIZED SPECTRA

CH. NO.	81.	82.	89.	90.	
51.	570.9	574.2	437.7	423.8	572.6
52.	497.0	512.9	367.0	357.5	505.0
53.	440.6	430.9	317.3	286.4	435.8
54.	362.2	368.2	280.3	245.6	365.2
55.	303.8	303.5	240.0	211.2	303.6
56.	244.4	243.4	182.9	173.1	243.9
57.	197.3	190.7	122.0	120.2	194.0
58.	142.2	143.6	75.3	89.2	142.9
59.	91.2	104.8	60.3	72.7	98.0
60.	60.4	68.1	46.2	59.5	64.2
61.	35.9	41.0	37.0	36.9	38.5
62.	25.8	26.9	15.7	16.7	26.4
63.	16.1	17.2	12.9	7.6	16.6
64.	20.6	21.8	9.4	5.2	21.2
65.	19.7	15.4	17.9	13.1	19.0
66.	13.2	15.2	10.8	9.0	17.2
67.	8.3	13.7	7.9	5.9	11.0
68.	5.2	12.4	2.3	1.7	8.8
69.	-3.2	15.3	-4.1	1.6	6.1
70.	4.6	13.2	-9.9	-8.8	8.9
71.	4.0	11.7	-15.1	-10.2	7.9
72.	7.9	11.3	1.5	-3.9	9.6
73.	2.0	8.3	10.7	10.0	5.1
74.	-.6	9.2	11.5	11.7	4.3
75.	4.8	8.1	-5.6	7.4	6.4
76.	3.6	5.6	-20.0	-5.8	4.6
77.	.6	9.3	-12.1	-10.6	4.9
78.	-3.9	12.2	-6.8	-7.3	4.2
79.	4.8	9.8	2.3	8.4	7.3
80.	9.8	2.7	-7.9	5.8	6.3
81.	7.3	-3.8	-22.7	4.8	1.8
82.	.6	-1.6	-24.7	7.3	-.5
83.	-2.6	1.4	-23.1	15.3	-.6
84.	3.7	2.2	-9.5	19.7	3.0
85.	6.3	.9	-4.2	6.4	3.6
86.	10.6	-1.2	4.6	9.5	4.7
87.	5.5	-.8	14.6	1.8	2.9
88.	12.7	3.7	3.2	-2.4	8.2
89.	4.7	1.7	-10.7	-6.3	3.2
90.	5.2	7.3	-17.2	-7.9	6.3
91.	-2.2	3.7	-16.2	-1.7	.7
92.	9.7	5.9	-10.5	1.8	7.8
93.	9.1	6.0	-11.2	11.2	7.6
94.	12.3	3.5	-6.4	13.5	7.9
95.	1.3	6.7	2.5	8.0	4.0
96.	-.3	.6	-4.6	-8.7	.1
97.	-7.6	1.4	.2	-5.3	-3.1
98.	-2.1	-4.8	-1.1	-1.7	-3.4
99.	-3.3	.3	14.1	7.9	-1.5

DIFFERENCE BETWEEN NORMALIZED SPECTRA

CH. NO.	81.	82.	89.	90.
2.	-.9	.9	5.2	.5
3.	1.0	-1.0	.4	8.1
4.	1.7	-1.7	-8.6	8.9
5.	-.5	.5	1.2	8.1
6.	-2.4	2.4	3.8	2.4
7.	3.8	-3.8	11.1	-3.9
8.	7.4	-7.4	9.4	-2.4
9.	5.4	-5.4	10.9	-.0
10.	-4.4	4.4	26.1	-8.9
11.	-6.9	6.9	17.3	-3.5
12.	-10.4	10.4	1.0	-11.4
13.	-8.3	8.3	-8.0	4.6
14.	-6.1	6.1	-7.7	-1.1
15.	-2.5	2.5	4.7	-6.8
16.	1.8	-1.8	7.9	-17.9
17.	1.6	-1.6	20.3	-6.9
18.	3.8	-3.8	14.2	14.0
19.	3.4	-3.4	9.8	31.0
20.	-2.1	2.1	7.4	34.0
21.	-4.5	4.5	19.9	30.9
22.	-6.1	6.1	22.8	34.0
23.	.2	-.2	24.4	33.6
24.	3.5	-3.5	32.2	27.8
25.	5.7	-5.7	40.5	33.4
26.	6.0	-6.0	48.2	43.5
27.	2.9	-2.9	58.6	47.9
28.	-3.9	3.9	64.0	50.4
29.	-4.5	4.5	63.9	57.5
30.	-5.6	5.6	53.5	72.4
31.	-1.8	1.8	62.3	79.1
32.	-3.1	3.1	68.2	89.6
33.	5.3	-5.3	80.3	99.5
34.	10.2	-10.2	72.6	96.3
35.	14.2	-14.2	84.0	91.1
36.	8.7	-8.7	96.5	91.2
37.	2.7	-2.7	115.4	104.1
38.	.8	-.8	102.1	111.4
39.	-3.2	3.2	94.0	102.9
40.	.7	-.7	66.0	85.5
41.	-1.2	1.2	58.7	66.7
42.	5.7	-5.7	53.6	48.5
43.	5.0	-5.0	54.6	25.5
44.	3.7	-3.7	40.3	-1.3
45.	-2.0	2.0	-8.2	-40.3
46.	-1.3	1.3	-33.0	-69.6
47.	1.5	-1.5	-90.9	-101.4
48.	8.1	-8.1	-97.8	-101.7
49.	10.9	-10.9	-116.9	-120.0
50.	.6	-.6	-123.0	-130.9

DIFFERENCE BETWEEN NORMALIZED SPECTRA

CH. NO.	81.	82.	89.	90.
51.	-1.6	1.6	-134.9	-148.7
52.	-7.9	7.9	-138.0	-147.5
53.	4.9	-4.9	-118.4	-149.3
54.	-3.0	3.0	-84.9	-119.6
55.	.1	-.1	-63.6	-92.5
56.	.5	-.5	-61.0	-70.8
57.	3.3	-3.3	-71.9	-73.8
58.	-.7	.7	-67.1	-53.6
59.	-6.8	6.8	-37.7	-25.3
60.	-3.9	3.9	-18.0	-4.8
61.	-2.6	2.6	-1.5	-1.6
62.	-.5	.5	-10.6	-9.7
63.	-.6	.6	-3.7	-9.1
64.	-.6	.6	-11.8	-16.0
65.	.6	-.6	-1.2	-5.0
66.	2.0	-2.0	-6.4	-8.2
67.	-2.7	2.7	-3.0	-5.1
68.	-3.6	3.6	-6.6	-7.1
69.	-9.2	9.2	-10.2	-4.5
70.	-4.3	4.3	-18.7	-17.7
71.	-3.8	3.8	-22.9	-18.1
72.	-1.7	1.7	-8.2	-13.5
73.	-3.2	3.2	5.5	4.9
74.	-4.9	4.9	7.2	7.3
75.	-1.6	1.6	-12.1	1.0
76.	-1.0	1.0	-24.6	-10.4
77.	-4.3	4.3	-17.0	-15.5
78.	-8.0	8.0	-11.0	-11.5
79.	-2.5	2.5	-5.0	1.1
80.	3.6	-3.6	-14.1	-.5
81.	5.6	-5.6	-24.5	3.0
82.	1.1	-1.1	-24.3	7.8
83.	-2.0	2.0	-22.5	15.9
84.	.8	-.8	-12.5	16.8
85.	2.7	-2.7	-7.8	2.8
86.	5.9	-5.9	-.1	3.8
87.	3.6	-3.6	11.7	-1.0
88.	4.5	-4.5	-5.0	-10.6
89.	1.5	-1.5	-13.9	-9.5
90.	-1.0	1.0	-23.5	-14.2
91.	-2.9	2.9	-17.0	-2.4
92.	1.9	-1.9	-18.2	-5.9
93.	1.5	-1.5	-18.7	3.6
94.	4.4	-4.4	-14.3	5.6
95.	-2.7	2.7	-1.5	4.0
96.	-.5	.5	-4.7	-8.9
97.	-4.5	4.5	3.2	-2.3
98.	1.4	-1.4	2.3	1.3
99.	-1.8	1.8	15.6	9.3

NRC FORM 335 (7-77)

U.S. NUCLEAR REGULATORY COMMISSION

BIBLIOGRAPHIC DATA SHEET

1. REPORT NUMBER (Assigned by DDC)
NUREG/CR-2905

4. TITLE AND SUBTITLE (Add Volume No., if appropriate)
Raman Scattering Temperature Measurements for Water Vapor in Nonequilibrium Dispersed Two-Phase Flow

2. (Leave blank)

3. RECIPIENT'S ACCESSION NO.

7. AUTHOR(S)
C. M. Anastasia, S. Neti, W. R. Smith, J. C. Chen

5. DATE REPORT COMPLETED
MONTH: June | YEAR: 1982

9. PERFORMING ORGANIZATION NAME AND MAILING ADDRESS (Include Zip Code)
Lehigh University
Institute of Thermo-Fluid Engineering and Science
Bethlehem, PA 18015

DATE REPORT ISSUED
MONTH: September | YEAR: 1982

6. (Leave blank)

8. (Leave blank)

12. SPONSORING ORGANIZATION NAME AND MAILING ADDRESS (Include Zip Code)
U. S. Nuclear Regulatory Commission
Office of Nuclear Regulatory Research
Division of Accident Evaluation
Washington, D.C. 18015

10. PROJECT/TASK/WORK UNIT NO.

11. CONTRACT NO.
B6794

13. TYPE OF REPORT
Technical

PERIOD COVERED (Inclusive dates)
June 1981-June 1982

15. SUPPLEMENTARY NOTES

14. (Leave blank)

16. ABSTRACT (200 words or less)

The objective of this investigation was to determine the feasibility of using Raman scattering to measure vapor temperatures in dispersed two-phase flow as an alternative nonintrusive technique. The Raman system developed for this investigation is described, including alignment of optics and optimization of the photodetector for photon pulse counting. Experimentally obtained Raman spectra are presented for the following single and two-phase samples: liquid water, atmospheric nitrogen, superheated steam, nitrogen and water droplets in a high void fraction air/water mist, and superheated water vapor in nonequilibrium dispersed flow.

17. KEY WORDS AND DOCUMENT ANALYSIS

17a. DESCRIPTORS

Raman scattering
Nonequilibrium vapor temperatures

17b. IDENTIFIERS/OPEN-ENDED TERMS

18. AVAILABILITY STATEMENT
Unlimited

19. SECURITY CLASS (This report)
Unclassified

21. NO. OF PAGES

20. SECURITY CLASS (This page)
Unclassified

22. PRICE
$

NRC FORM 335 (7-77)

☆U.S. GOVERNMENT PRINTING OFFICE: 1982-361-297:2411